Investigations of Non-Covalent Carbon Tetrel Bonds by Computational Chemistry and Solid-State NMR Spectroscopy

Scott Alexander Southern

A thesis submitted to the Faculty of Graduate and Postdoctoral Studies in partial fulfillment of the requirements for the degree of

Master of Science

Ottawa-Carleton Chemistry Institute
Department of Chemistry and Biomolecular Sciences
Faculty of Science

University of Ottawa

Table of Contents

List of Figures

List of Tables

Abstract

Non-covalent bonds are an important class of intermolecular interactions, which result in the ordering of atoms and molecules on the supramolecular scale. One such type of interaction is brought about by the bond formation between a region of positive electrostatic potential (σ-hole) interacts and a Lewis base. Previously, the halogen bond has been extensively studied as an example of a σ-hole interaction, where the halogen atom acts as the bond donor. Similarly, carbon, and the other tetrel elements can participate in σ-hole bonds. This thesis explores the nature of the carbon tetrel bond through the use of computational chemistry and solid state nuclear magnetic resonance (NMR) spectroscopy.

The results of calculations of interaction energies and NMR parameters are reported for a series of model compounds exhibiting tetrel bonding from a methyl carbon to the oxygen and nitrogen atoms in a range of functional groups. The ^{13}C chemical shift (δ_{iso}) and the $^{1c}J(^{13}\text{C},^{17}\text{O}/^{15}\text{N})$ coupling across the tetrel bond are recorded as a function of geometry. The sensitivity of the NMR parameters to the non-covalent interaction is demonstrated via an increase in δ_{iso} and in $|^{1c}J(^{13}\text{C},^{17}\text{O}/^{15}\text{N})|$ as the tetrel bond strengthens. There is no direct correlation between the NMR trends and the interaction energy curves; the energy minimum does not appear to correspond to a maximum or minimum chemical shift or *J*-coupling value.

Gauge-including projector-augmented wave density functional theory (DFT) calculations of δ_{iso} are reported for crystals which exhibit tetrel bonding in the solid state. Experimental δ_{iso} values for sarcosine, betaine and caffeine and their tetrel-bonded salts generally corroborate the computational findings. This work offers new insights into tetrel

bonding and facilitates the incorporation of tetrel bonds as restraints in NMR crystallographic structure refinement.

Acknowledgements

This work would not have been possible without the help and support of many friends, family, colleagues and mentors that I've worked with over the past couple years. First and foremost, I would like to thank Professor David L. Bryce, my supervisor, for his exceptional guidance throughout my time in the Bryce Lab. Thank you for having confidence in me, and providing me with a rich environment in which I could learn and excel. I look forward to continuing working with you in the coming years. I would also like to acknowledge Professors Alain St-Amant and Natalie Goto for reading this thesis and providing to me valuable comments.

To my friends and colleagues at the University of Ottawa – thank you for your support and your thoughtful discussions. Dr. Glenn Facey and Dr. Eric Ye at the University of Ottawa NMR lab, your advice and technical support was invaluable throughout this work. To my fellow Bryce Lab colleagues, I appreciate our collaboration over the years. Dr. Fred A. Perras, you first introduced me to solid-state NMR on one of my first days in the lab. I remember you making me spin up the DOR rotor that day without me knowing anything about DOR at the time. Nothing could get me more interested in this field on the first day than getting hands on work. Dr. Kevin M. N. Burgess, while we didn't work together directly that much, you taught me to value sober second thought when it came to the more philosophical aspects of life. Dr. Jasmine Viger-Gravel, you taught me the importance of being precise and meticulous in my research, a trait you've already perfected. To Pat Szell and Sherif Nour, and more recent fellow graduate students Yijue Xu, Angel Wong, and Peter Werhun, life in the office and in the lab wouldn't be as interesting without you. Finally, a special thank you needs to be made to Dr. Libor Kobera, who has gone above and beyond in ensuring I am well trained in the finer aspects of NMR spectroscopy. I would finally also like to take the opportunity to thank the various undergraduate students who I've also worked with. Jeremy Chin, Michael West and Dylan Errulat, your hard work has produced quality results.

Of course, all my time couldn't be spent in the lab alone. I would like to thank my friends and colleagues in my extended Canadian Armed Forces family for providing me with an environment in which I could have fun and focus my mind on other things for a while. Thanks to all of my mentors and supervisors: Maj. Jonathan McAuley, Capt. Dan Parker, the team at OpsAir, and others whom I've worked for directly, for providing me with valuable mentorship in challenging environments over the years. I believe that today I am a better leader and your training and support has benefitted me greatly in my civilian life. Thank you to my colleagues working in support of the Royal Canadian Air Cadets Program for all the good times; in particular Lt. Alex Schmid, for keeping sane and motivated over the years. It's nice to be able to let off steam and vent once in a while! Unfortunately, there are too many more to mention by name, but you all work so hard in providing an important and valuable experience for Canadian youth and I'm grateful for your lasting friendships.

Finally, I would like to thank all of my family and relatives for their love and support. Mom and Dad, over the years you've challenged me to go as far as I can in my education, and you've ensured that I could realize my goals without too much trouble. Evan, you'll have to deal with that a little longer, but thanks for reminding me not to take anything for granted. Thank you, Grandpa, in particular for always believing in me, and making me feel like a "smart cookie". Jane and Doug, thanks for being family to me when mine was so far away.

And finally, Alison, you’ve stood by me for everything, and I couldn’t imagine being with anyone else as I move on to the next chapter of my life. You are the love of my life.

“I have been looking for

someone to come up with NMR investigations on this interaction,

though, I thought it would be difficult. NMR evidence for hydrogen

bonding came nearly a century later. Tetrel carbon bonding

is barely a few years old.”

Elangannan Arunan

Statement of Originality

I certify that the work presented in this thesis is my own. With permission from the publisher, the scientific contribution of this work is based on my own published work in a peer reviewed journal. Sections 1.4 and 1.5, as well as Chapters 2, 3 and 4 are in part, or wholly based on the work published in:

Southern, S. A. and Bryce, D. L. NMR Investigations of Noncovalent Carbon Tetrel Bonds. Computational Assessment and Initial Experimental Observation. *The Journal of Physical Chemistry A,* **2015**, *119*, 11891-11899. DOI: 10.1021/acs.jpca.5b10848.

Chapter 1 - Introduction

1.1 The Basic Properties of Matter

It has been a long time since the idea of the particle first emerged among humans. The imaginations of the ancient Greek philosophers led them to believe that matter was not simply made of what could be seen, but rather individual units. Plato first suggested that matter was essentially divided into polyhedral subunits called elements: earth, air, water and fire. From that point, the great philosophers argued whether matter was continuous, or made from discrete units, trying for many years to resolve the issue before them.

The quest for the answer was later resolved by John Dalton, who first proposed the idea of atomic theory.[1,2] Since then, science has evolved to the point now, where matter has been almost fully characterized right down to the subatomic level, so far as even observing the elusive Higg's boson.[3,4]

In this tiny world, particles behave much differently than one would expect. Humans are used to seeing that when a baseball is thrown by the outfielder, it forms an arc before it arrives at the baseman; this motion is a result of classical mechanics. However, we must use quantum mechanics to describe the intricate details of the nature of the subatomic particles; the constituents of the atom.

Atoms are particles which are composed of electrons, neutrons and protons. When atoms are combined together, they form matter, which can form materials that we are more familiar with and that we can interact with. The atom can be described as a nucleus containing the neutrons and protons, surrounded by the orbiting electrons (**Figure 1**).

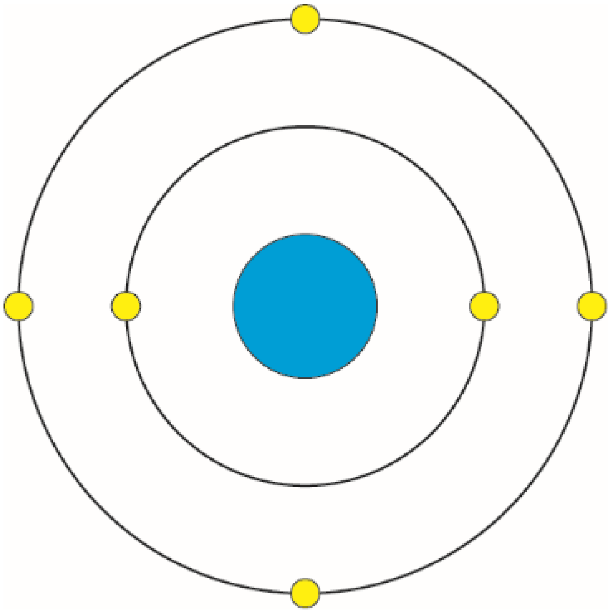

Figure 1. A basic representation of a ^{12}C atom using the Rutherford-Bohr model. The nucleus (blue) is surrounded by the orbit of electrons occupying two energy levels. Two electrons (yellow) reside in the n=1 shell, and four in the n=2 shell. Note that further electronic orbitals may exist beyond those that are occupied in the case of an excited electronic state.

The atom is defined by its atomic number, which represents the number of protons residing within the nucleus. The atomic weight is the average of all the weights of each isotope, weighted according to their abundance in nature. An isotope of a particular element is one which has a different number of neutrons than the other.[5] For example, while ^{12}C contains six neutrons and six protons, ^{13}C contains seven neutrons, and six protons. A given atom that is isolated will always carry the same number of electrons, regardless of the isotope.

The electron configuration of a particular atom describes the arrangements of its electrons in terms of discrete atomic orbitals. It assumes that only two electrons may occupy a given atomic orbital, as defined by the Pauli Exclusion Principle.[6,7] Closest to the nucleus is the $1s$-orbital. Further away are the p-, *d-,* and *f*-orbitals, each with x, y, and z Cartesian components. Consider a ^{12}C atom, which has six electrons. Its formal configuration is $1s^22s^22p^2$ because it has two electrons in its core orbital, and a total of four electrons in the valence s- and p-orbitals. It is worth noting that in quantum mechanics, the square of the atomic orbitals represent the probability of observing electron density at any point in space surrounding a nucleus, so they exist in various shapes and symmetries. [7] The larger the atom, the more electrons it has, and therefore the more orbitals that are filled. Hund's rule[8,9] states that the electronic orbitals are filled with one electron, before filling it with a second. So when there are three p-orbitals of the same energy, each must be filled by one electron before they can be filled again by a second electron. To illustrate this, **Figure 2** shows the electronic configuration of fluorine, where the $2p$-orbitals are each filled by one electron, then by a second electron of opposing spin. The $2p_Z$-orbital remains filled with only one electron.

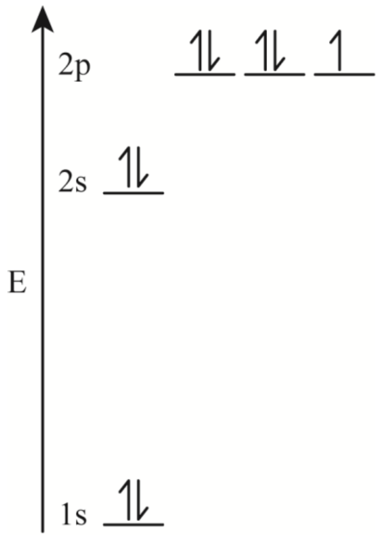

Figure 2. The electronic configuration diagram for a single fluorine atom ($1s^2 2s^2 2p^5$). The filling of the molecular orbitals, with increasing energy, follows Hund's rule.

In describing the electronic orbitals as a set of allowed states which the electrons can possess, they can be quantized by the quantum number, *n*. By doing this, the idea of quantum mechanics is introduced to the description of the atom. Quantum mechanics is the more accurate description and it will be used throughout this thesis.

Protons have a net positive charge, and electrons hold negative charge. However, this is a simplistic view of the particle, and in fact, their character becomes more complex. In fact, the description of subatomic particles may include such characteristics as spin, angular momentum, and magnetic moment.

Nuclear spin is an important property of the nucleus. Just as the Earth rotates around its axis, spin can be thought of, in a classical sense, as the rotation of a nucleus around its own axis.[10] Consequently, particles possess spin angular momentum. Consider a gyroscope. When it is spun, it tends to remain in place until a force is acted upon it due to the conservation of angular momentum. While it may seem quite familiar, this classical description of the elementary particle is, of course, false, and indeed nuclei do not actually rotate around axes in the way a planet does. Instead, chemists resort to quantum mechanics in order to properly describe the angular momentum due to the fact that subatomic particles display properties of both particles and waves (the *wave-particle duality*). Spin is an intrinsic property[10], and it may be described as α or β; being "up" or "down," respectively. They are represented in the electronic configuration diagrams by upward and downward arrows, respectively (**Figure 2**).

1.2 Noncovalent interactions

Noncovalent interactions are the result of the interactions between electrons resulting from their charge distributions over a particular atom or molecule. These interactions can, consequently, exist between two different molecules or within a molecule but between nearby groups. Some examples of noncovalent interactions include van der Waals (vdW) interactions, π-interactions and electrostatic interactions.

Electrostatic interactions, such as the dipole-dipole interaction is an example of an attractive vdW interaction arising due to the electronic dipoles formed from the asymmetric distribution of electrons over the surface of an atom or a molecule, where some regions tend to be more electronegative than others.[5] In some cases, that region may also possess a formal charge. For example, two molecules of acetone may interact between the carbonyl oxygen of one molecule and the carbonyl carbon of the other. Hydrogen bonds exhibit partially noncovalent character (**Figure 3**), whereby the partially positive charge on the hydrogen atoms can interact with a partially negative charge.[11,12] π-interactions may, for example, occur between the negative charge distribution on aromatic faces resulting from the π-orbitals, and any partially positive or formally positive counter charge, such as an ion or another aromatic ring. These interactions are quite weak, on the order of less than 10 kcal/mol, yet significant especially in protein folding or molecular signalling, because amino acids histidine, tryptophan, phenylalanine, and tyrosine all contain aromatic rings with π-systems.[13,14]

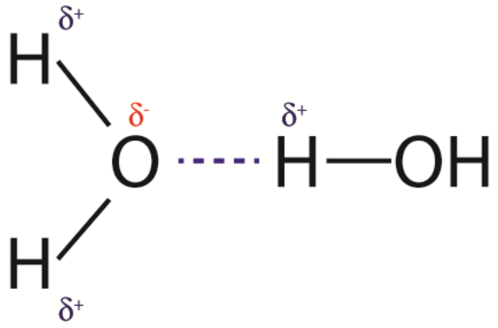

Figure 3. The hydrogen bond. The electrostatic interactions between the partially positive (δ^+) and partially negative (δ^-) charge contribute to an attractive interaction between the oxygen and hydrogen atoms in water molecules.

Noncovalent bonding mediated by σ-holes has been studied extensively in the context of halogen bonding[15,23,24], pnicogen bonding [16,17], chalcogen bonding. [18,19,20,21] Bonding involving the noble gases, coined "aerogen bonding", has also been explored in the recent years. [22] Halogen bonding[23,24] is an example of a noncovalent interaction, where an area of partially positive charge, called a σ-hole[25,26], acts as an electrophile for a negatively charged or electron rich molecule.

Each of the preceding are examples of σ–hole interactions which is a subclass of noncovalent interactions.[27,28] In every case, the bond donors interact with a Lewis base like entity, such as electronegative atoms or lone pairs of electrons (**Figure 5**). As with covalent bonds, the strength of the σ–hole bond can be expressed in terms of energy, whereby the resulting energy is known as the bonding energy.

Table 1. Typical interaction strength of noncovalent interactions compared to some examples of covalent bonds. A variety of examples were selected to present an idea of expected interaction energy strengths.

Interaction		Interaction Strength / kcal mol^{-1}
Covalent Bond	C-C	85[29]
	C-H	100[29]
	C=O	175[29]
Hydrogen Bond		1-3[29]
	PH···N	0.8[30]
van der Waals Interactions		0.5-1[29]
Halogen Bond		1-7[31]
	chloro-cyanoacetylene	2.3[32]
Chalcogen Bond	$H_2S \cdots Cl^-$	0.81[33]
	$SCS \cdots Cl^-$	10.59[33]
	$F_4S \cdots NH_3$	14[21]
Pnicogen Bond	FN···N	4[30]
	PN···N	7[30]
	$F_4P \cdots NH_3$	43[17]
	$H_3FP \cdots NH_3$	36[17]

1.2.1 Sigma-Holes

Computational examination of the electrostatic potential (ESP) surfaces of halogen bonding molecules revealed that on one side of the interaction, there was an area in which different charges were present on a single atom.[25,26]

Consider a symmetric atom in a vacuum in the absence of any external effect of charge, magnetism or other influences. In the case of this lone atom, the ESP is generally positive because the effect of the nucleus dominates over the effect of the electrons which are dispersed over the entire atom.[34] The electrostatic potential resulting from the contributions of the electron density, $\rho(r)$, and the charge on the nucleus, Z_A, at any point r on the surface of an atom is given by[34]:

$$V(r) = \sum_A \frac{Z_A}{|R_A - r|} - \int \frac{\rho(r')dr'}{|r' - r|} \qquad \textbf{1}$$

where the distance between the point and the nucleus is R_A. Typically, the $\rho(r) =$ 0.001 electrons/bohr^3 surface is used to represent a molecular surface, corresponding to an electrostatic potential of $V_S(r)$. When the effects of the electrons dominate at a given point, the expression yields a negative value on the potential surface. The ESP provides an effective and convenient way to model the σ-hole in noncovalent bonding.[26]

The σ-hole is an area at which $V(r)$ has a value that is more positive than the surrounding area, thus indicating and area of electronic depletion. When the atom of interest is covalently bound to another atom or functional group with electron withdrawing character, such as a trifluoromethane group, a substituted aromatic ring, an amino group, the tendency is for the electronic distribution to be drawn toward the covalent σ–bond. This gives rise to a σ–hole situated along the extension of the covalent on the opposite side of the atom of interest. The point representing the σ–hole can be depicted as $V_{s,max}$ because it typically portrays a local area of maximum electrostatic depletion.[15]

The electrostatic depletion at $V_{s,max}$ can be explained using natural bond order (NBO) analysis.[35] It has been shown that the halogen bond donor atoms tend to possess a sigma bonding orbital as well as three unshared pairs of electrons, each occupying the p-orbitals. The p_z orbital lying along the axis of the covalent bond is half filled, resulting in an $s^2p_x^2p_y^2p_z^1$ character. The result is therefore a "belt"[35] of negative electrostatic potential around the halogen atom, leaving an area of electronic deficiency on the opposite end of the covalent bond; the σ–hole.[26] The magnitude of this electronic deficiency comes down to the amount of s character is present in the p-orbital; the more purely p the orbital is, the stronger the σ–hole.[26] The σ–hole can be effectively neutralized by a negative group such lone pair of electrons, and this accounts for the high degree of linearity in such an interaction.[36] The situation is somewhat different with respect to the group IV tetrel elements. The tetrel elements do not have lone pairs of electrons, and are as such sp^3 hybridized. Consequently, there is a large amount of s-character in the bonding orbitals. The conclusion is, however, that reduced p-character of the bonding orbital is acceptable, and the σ–hole remains present, albeit weaker.[36]

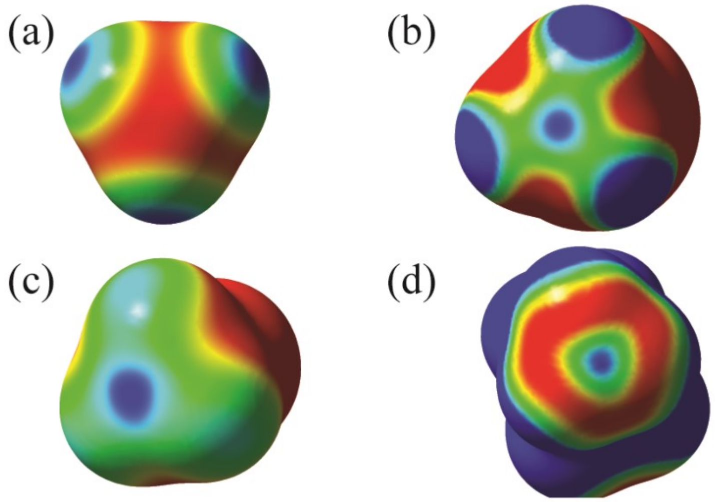

Figure 4. The electrostatic potential at the 0.001 a.u. surface of various structures exhibiting σ-holes. The σ-hole is present on (b) chloromethane; (c) fluoromethane; (d) a methyl group that is covalently bonded to methylammonium. For illustration purposes, a molecule of methane (a) is shown and does not to possess a sigma hole on carbon. Instead, the area where the σ–hole ought to be is more negative due to the electronic depletion over the hydrogen atoms (each of which coincidently possess a single σ–hole[15]). The red colour corresponds to electrostatic potential values ≤ 0.172 a.u. and the blue colour corresponds to electrostatic potential values ≥ 0.179 a.u.

The strength of a σ-hole depends significantly on the electron withdrawing character of its covalently bonded partner atom or molecule.[36] Considering iodine, bound to a methyl group, one is not likely to observe a significant σ–hole. In this case, the methyl carbon is not considered to be very polarizing because the hydrogen atoms do not have any polarization capabilities. In fact, the polarization strength of iodine has a greater effect and it would be more likely that a negative *σ*–hole would be found on the iodine atom, and a positive *σ*–hole on the carbon. [26] Conversely, when fluorine atoms, or other electron-withdrawing substituents such as aromatic rings, are substituted for the hydrogen atoms, a relatively strong σ–hole is introduced as a result of the increased electron withdrawing ability of the other group.[26.19]

The electronic potential of a number of σ–holes generated by various electron withdrawing substituents has been listed by Politzer et al.[27] They show that the strongest σ–holes are achieved when cyanide groups are used, although these σ–holes are achieved only when the entire isoelectric surface is positive in nature. Other substituents, such as fluorine and chlorine, also contribute to the formation of σ–holes.[15] in general, $V_{s,max}$ becomes increasingly positive as the rest of the molecule becomes more electron-withdrawing.[37]

1.2.2 Sigma Hole Bonding

Consider a molecule or fragment RX interacting with a nucleophilic molecule or fragment Y (often an anion, a Lewis base, or π-electrons). The σ-hole is on X along the extension of the covalent bond to R (**Figure 5**). Depending on the identity of element X, such interactions take on their own names in the literature, e.g., halogen bonding, pnicogen bonding, chalcogen bonding, and aerogen bonding, where the name of the interaction refers to the periodic table group to which the bond donor (electron acceptor) belongs (group V: pnicogens; group VI: chalcogens, etc.).[38] These are all different types of σ-hole bonds.

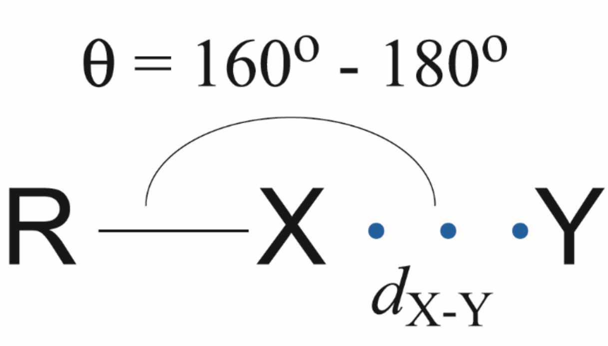

Figure 5. General schematic of a tetrel bond, where R is a covalently bonded atom or functional group, X is the tetrel bond donor (X = C, Si, Ge, Sn, or Pb), and Y is the tetrel bond acceptor.[40] $d_{\text{X-Y}}$ is smaller than the sum of the van der Waals radii of the interacting atoms.

The σ–hole has been studied extensively as it applies to halogen bonding. Considering again the iodine atom covalently bound in I-CF_3, one would expect to observe a relatively significant σ–hole. In terms of its electropositive character, the magnitude of $V_{s,max}$ within the σ–hole increases as the atomic number of the halogen increases, thereby increasing the interaction strength of the halogen bond.[15] For example, the σ–hole bond between a π-electron and an iodine atom would be greater than that resulting from a bromine atom.

In general, the bonding energy is a negative value, representing an attractive interaction. The correlation between the $V_{s,max}$ and the interaction energy is such that when the electronic depletion on the σ–hole is increased, the magnitude of the bond strength increases as well. It can therefore be expected that σ–bond donors with higher atomic numbers will more readily form bonding interactions. That's not to say that weakly polarized atoms such as carbon will not participate in these types of bonds; the bonds will simply be weaker in nature and sometimes difficult to produce by crystallization.

1.3 Group IV “Tetrel” Bonding

The focus of this thesis is on tetrel bonding, named after the bond donor, which falls under group IV in the periodic table.[36,39,40,56] In an R-C···Y carbon tetrel bond (**Figure 5**), the σ-hole resides on carbon. As noted by Politzer[27], often in such group IV cases, all or almost all of the electrostatic potential on the R-C moiety is positive and in such cases the σ-hole is simply identified as a region which is more positive than its surroundings (**Figure 4**), leading to the preferential formation of an interaction from the σ-hole over other types of complexes.

As is generally the case for σ-hole bonds, the strength of the tetrel bond depends largely on the atomic number of X and by the electron withdrawing ability of the R substituents.[41,42,43] The nature of the tetrel bond donor has an impact on the tetrel bond strength, whereas the atomic size of the bond donor increases from C to Sn, the bonding energy increases. This is attributed to an increase in the polarizability of the atom as one goes down the periodic table, thus increases the size of the σ–hole.

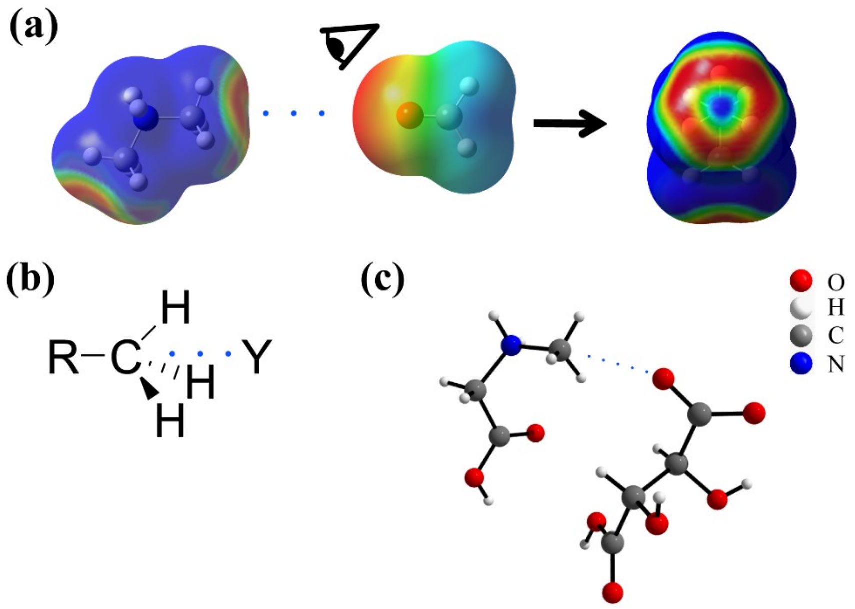

Figure 6. (a) The electrostatic potential at the 0.001 au surface of positively charged dimethylammonium (left) and formaldehyde (centre) computed by CAM-B3LYP/6-311++G(d,p). The red colour on dimethylammonium (right) corresponds to electrostatic potential values ≤ 0.172 au; the blue colour corresponds to electrostatic potential values ≥ 0.179 au. The σ-hole is present on the methyl carbon and is adjacent to the C-N σ-bond, and it has an electrostatic potential value of 0.179 au. (b) A carbon tetrel bond involving a methyl carbon. (c) An example of a carbon tetrel bond occurring in the crystal structure of sarcosinium tartrate.[44]

Experimental evidence for tetrel bonding involving Si and Sn has been in the literature for many years. Silicon tetrel bonding was noted to mediate chemical reactions by its hexacoordinated intermediate.[45] In other cases, hexacoordinated tetrel bonded silicon atoms have been observed to exist in various species.[46,47] Inter- and intramolecular tetrel bonding of silicon and lead atoms have also been demonstrated through crystallographic methods.[48,49,50]

Additional evidence for the existence of tetrel bonding involving carbon as well as silicon has been growing significantly in recent years.[36,39,51,52] Quantum calculations have confirmed the presence of carbon tetrel bonds between electron deficient carbon atoms and electron rich tetrel bond acceptors.[40,42,53,54] The importance of the tetrel bond may be analogous to other forms of noncovalent bonding. Given that carbon atoms are in abundance in nature and in synthetic chemistry, carbon tetrel bonding may play important roles in the organization of molecular units, from natural products to functional materials and pharmaceuticals. Furthermore, it could be envisaged that carbon tetrel bonding could play a role in directing molecular orientation in some dynamic systems, such as protein folding, ligand-acceptor interactions, or other processes of biological importance.[40,55] For instance, it has recently been suggested that the carbon tetrel bond could play a critical role in directing S_N2 reactions (**Figure 7**).[56] A search of the Crystal Structure Database (CSD) demonstrates that there are perhaps thousands of examples where the tetrel bond interactions exist, and could be contributing to the three-dimensional packing arrangements of molecules within their crystal lattices.

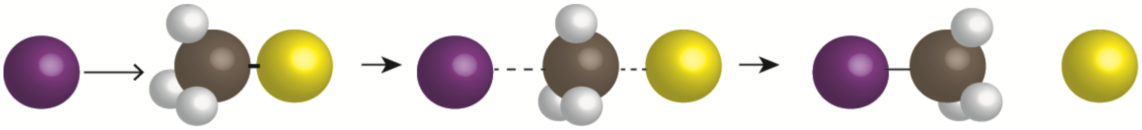

Figure 7. A schematic showing the influence of a tetrel bond on the activation of an S_N2 reaction. Inspired from the work of Grabowski.[56] Purple: fluorine; Grey: carbon; White: hydrogen; and Yellow: chlorine.

Recently, Arunan related the atoms in molecules (AIM) descriptors for a hydrogen bond[57] to the carbon tetrel bond, an implication that similar rules could be applied to tetrel bonding.[15] These criteria are meant to test for the presence of a bond path indicative of a noncovalent interaction (a hydrogen bond in the original paper). Among these criteria were: 1. A bond path linking two interacting atoms must connect the bond critical point which is present between both atoms; 2. There must be mutual penetration of the electron density clouds; 3. On the formation of the complex, the bond donor loses some charge, and there is some destabilization on the donor atom; 4. The atomic volume of the donor atom decreases. In almost all of the examples presented by Arunan, the carbon tetrel bonded complexes follow the proposed behaviour of hydrogen bonds.

IR spectroscopic studies on tetrel bonded complexes have shown that there is a red shift in the C-X stretching frequency due to hyperconjugation of lone pair orbitals of the bond acceptor and the anti-bonding orbital of the bond donor.[15] This causes a weakening of the sigma bond between X and C causing a decrease in the stretching frequency.

Finally, computational work in 2009 provided key evidence predicting σ-hole bonding to the lightest tetrel element, carbon.[36] More recently, Thomas et al. identified 716 compounds which may exhibit C···O tetrel bonding in the compounds in the CSD.[58] They conducted important experiments providing charge density analysis of fenobam and dimethylammonium 4-hydroxybenzoic acid in the solid state, each exhibiting carbon tetrel bonds. The results indicated the presence of a tetrel bond on the latter structure.

However, the former preferentially formed hydrogen bonds between the methyl hydrogen and the associated chlorine atom.

1.4 Nuclear Magnetic Resonance Spectroscopy

1.4.1 The Zeeman Interaction

It is useful to begin the discussion of nuclear magnetic resonance (NMR) by first discussing the basics of quantum mechanics. Nuclei possess a nuclear spin quantum number, I, which can take the values of integers and half integers of 0, ½, 1, etc., increasing in intervals of one half. Nuclei possessing spin with integer values of I are known as *bosons* while nuclei with half-integer spin values are called *fermions*.[10]

Related to spin is the property called angular momentum, L, given by eqn. **2** as:[10]

$$L = \hbar\sqrt{I(I+1)} \qquad \mathbf{2}$$

The nuclear spin angular momentum is a vector with a component along the *z*-axis. The *z*-component interacts directly with the applied magnetic field, B_0 (reported in units of Tesla (T)), which also lies along the *z*-axis. It is for this reason that the angular momentum operator representing its *z*-component can therefore be defined by $\hat{I}_z$.

The angular momentum gives rise to an intrinsic property called magnetic moment, μ, representing the interaction between the nucleus and the magnetic field.[10] μ is dependent on both the nuclear spin angular momentum and the gyromagnetic ratio, γ (rad s^{-1} T^{-1}). The total energy from this interaction is given by:[59]

$$E = -\mu B_0 \qquad \textbf{3}$$

The spin quantum number, I, has corresponding eigenvalues of m_l, equal to $-I$ to $+I$ in intervals of 1. Thus, for any value of I, there are precisely $(2I + 1)$ eigenvalues. The $\hat{I}_z$ operator has $(2I + 1)$ eigenfunctions. In general, this can be represented by:

$$\hat{I}_z \psi_m = m_l \hbar \psi_m \qquad \textbf{4}$$

It is now useful to define the Hamiltonian for a spin in a magnetic field. The Hamiltonian operator is dependent on the gyromagnetic ratio, B_0, and the angular momentum operator. Eqn. **5** describes the Hamiltonian:

$$\hat{H} = -\gamma B_0 \hat{I}_z \qquad \textbf{5}$$

Thus, when the Schrödinger equation for a single spin in the magnetic field is given by:

$$\hat{H} \psi_m = E_m \psi_m \qquad \textbf{6}$$

where the energy, E_m (in units of Joules) representing the eigenstates of the nuclear spin in the presence of the magnetic field is given by eqn. **7**:

$$E = -m_l \hbar \gamma B_0 \qquad \textbf{7}$$

Each energy state can be labelled as an α state or a β state, representing the lower energy and higher energy levels, respectively. These eigenstates are related to the magnetic moment such that lowest possible energy is brought about by perfect alignment with the magnetic field. The transition energy corresponds to the energy which must be subjected to a nuclear spin in order to induce a transition from the α state to the corresponding β state, matching to a specific electromagnetic frequency. This is referred to as the NMR transition, and the transition can only occur when the difference between both values of m_l is equal to exactly one. The frequency of the photon that will induce an NMR transition, or the *Zeeman Effect* (**Figure 8**), is given in eqn. **8**, where ν_0 is the *Larmor frequency*, and is isotopically specific due to its dependence on the gyromagnetic ratio.

$$\nu_0 = \frac{\gamma B_0}{2\pi} \qquad \mathbf{8}$$

In a simple system, one would expect a line on the NMR spectrum at the exact frequency of ν_0. However, this is not typically the case because nuclear spins are usually affected by their chemical environments. The energy eigenvalue becomes significantly more complex as the nature of the nearby electrons, as well as the coupling to other nuclei is taken into account.

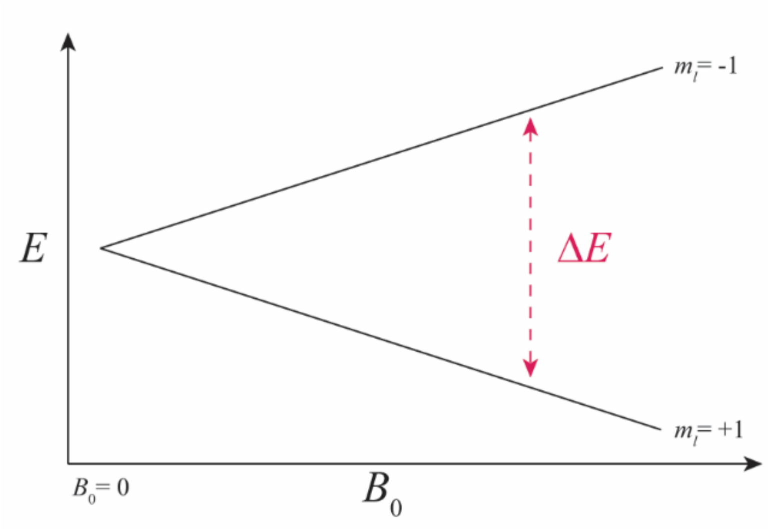

Figure 8. The *Zeeman Effect* for a spin $\frac{1}{2}$ nuclide. The splitting of the spin states is observed as a function of the strength of the magnetic field.

In the absence of a magnetic field, the direction of the spins is isotropic.[10] When a sample is placed in B_0, the interaction of the spin nuclear magnetic moments with the magnetic field will cause their bulk alignment with B_0. This is a process that is time dependent and is known as T_1 spin-lattice relaxation. The net equilibrium magnetization can be represented by the vector, $\overrightarrow{M}$. In the end, the spin polarization does not align with the magnetic field *per se*, but instead, the magnetic moments cause the spins to rotate *around* B_0 in the shape of a "precession cone"[10] with oscillations equal to ν_0. The *z*-component of the magnetization is important for NMR.

At the thermal equilibrium, the distribution of spins in the high energy state versus the low energy state is governed by the Boltzmann distribution:

$$\frac{n_{\alpha 2}}{n_{\beta 1}} = e^{-\frac{\Delta E}{kT}} \qquad \mathbf{9}$$

The NMR experiment is therefore the practice of manipulating the magnetization vector through space. A sample is placed in a coil which is situated in the xy-plane perpendicular to B_0. By applying a radiofrequency (RF) pulse along the x- or y- axis, the magnetization may be tilted away from the z-axis. In doing so, the magnetization precesses around the z-axis at the Larmor frequency, resulting in a component of the vector oscillating in the xy plane. The vector oscillations can be detected as it induces a current in the coil. These oscillations are detected by the spectrometer. The magnetization vector continues to precess around the z-axis, but the cone eventually returns to the thermal equilibrium along the z-axis, causing a gradual decrease of the xy component of the magnetization over time. The detected current in the coil resulting from the oscillations in the xy-plane is known as the free induction decay (FID). The FID is transformed from the time domain to the frequency domain through Fourier transform to an NMR spectrum.

As it was mentioned before, nuclear spins are affected by their chemical environments. For example, the effects of the electrons shielding the interaction between the nucleus and B_0 would have a direct effect on the resulting NMR transition. Other effects, such as spin-spin coupling, or the quadrupolar interaction of some nuclides can have a major impact on the NMR spectrum. These NMR interactions are essentially perturbations to the *Zeeman* interaction. Thus, the NMR spectrum is complicated by the fact that these interactions exist.

The Hamiltonian for a spin in a magnetic field is therefore not only dependent on the Zeeman Hamiltonian alone (eqn. **5**). In fact, it is additionally dependent on the magnetic shielding interaction, the direct and indirect dipolar coupling interactions, and the quadrupolar interaction in the case of nuclides with spin greater than $\frac{1}{2}$. It is therefore essential to examine some of these interactions in detail. For the purposes of this thesis, only the magnetic shielding interaction as well as the indirect spin-spin *J*-coupling interactions will be discussed in detail.

1.4.2 Magnetic Shielding

Magnetic shielding is brought about by the magnetic fields generated by the electrons. These fields may be additive or subtractive to B_0, and consequently change the way the nuclear magnetic moment interacts with the magnetic field. The magnetic field seen by the nucleus as a result of the effects of magnetic shielding is given by:

$$B_\sigma = (1 - \sigma)B_0 \qquad \mathbf{10}$$

where σ is the shielding constant.

Using the secular approximation, the magnetic shielding operator is shown in eqn. **11** to be dependent on the gyromagnetic ratio and the shielding constant.

$$\hat{H}_\sigma = -\gamma\hbar\bar{\sigma}B_0\hat{I}_Z \qquad \mathbf{11}$$

The magnetic shielding interaction is anisotropic by nature, meaning it is orientationally dependent. In expression **12**, the magnetic shielding tensor is diagonalized such that the interaction is represented by its principal axis system (PAS).

$$\begin{bmatrix} \sigma_{xx} & \sigma_{xy} & \sigma_{xz} \\ \sigma_{yx} & \sigma_{yy} & \sigma_{yz} \\ \sigma_{zx} & \sigma_{zy} & \sigma_{zz} \end{bmatrix} \Rightarrow \begin{bmatrix} \sigma_{11} & 0 & 0 \\ 0 & \sigma_{22} & 0 \\ 0 & 0 & \sigma_{33} \end{bmatrix} \quad , \quad \sigma_{11} \leq \sigma_{22} \leq \sigma_{33} \qquad \mathbf{12}$$

The isotropic shielding constant, σ_{iso}, is given as the average of the three shielding tensor components (eqn. **13**). Further parameters which may be used are the span, Ω, and the skew, κ, measuring the breadth of the signal and the asymmetry, respectively (eqn. **14** and **15**).[60] The span is related to the distribution of the signals corresponding to the orientations the molecule takes in the sample, which is averaged out in a solution, and the skew is the asymmetry of the distribution of the signals.

$$\sigma_{iso} = \frac{\sigma_{11} + \sigma_{22} + \sigma_{33}}{3} \qquad \mathbf{13}$$

$$\Omega = \sigma_{33} - \sigma_{11} \qquad \mathbf{14}$$

$$\kappa = \frac{3(\sigma_{iso} - \sigma_{22})}{\Omega} \qquad \mathbf{15}$$

The shielding constant is observed directly in the NMR spectrum in the form of a chemical shift. The chemical shift is the value of σ with respect to a reference. For example, the secondary reference for a ^{13}C spectrum could be glycine, and the chemical shift of the carbonyl carbon is 176.4 ppm with respect to tetramethylsilane ($\delta_{iso}^{\mathrm{TMS}} = 0$ ppm).[61] In units of Hz, the chemical shift is defined by eqn. **16**:

$$\delta = \frac{\sigma_{ref} - \sigma}{1 - \sigma_{ref}} \tag{16}$$

The preceding formula can also give the chemical shift in units of parts per million by simply multiplying by 10^6.

1.4.3 Spin-spin coupling

In general, coupling results from the interaction between two different spins. Indirect spin-orbit coupling (*J*-coupling) occurs when the interaction between two nuclear spins is mediated by the electrons involved in their bonding.

J-coupling is typically only a very small perturbation to the Zeeman interaction. Therefore, it is likely that the other NMR interactions overshadow the presence of this interaction because it tends to be on the order of a few Hz for first-row elements. Nevertheless, *J*-coupling is a very important tool for probing the connectivity of atoms in a molecule.[62] In units of Hz, the *J*-coupling operator between nucleus 1 and 2 is:

$$\hat{H} = 2\pi \hat{I}_1 J \hat{I}_2 \tag{17}$$

In the preceding Hamiltonian, J is the orientation-dependent *J*-coupling tensor. The isotropic *J*-coupling (J_{iso}) is the average of the principal components of the tensor. The anisotropic contribution to *J*-coupling (ΔJ) is averaged out in the molecular tumbling of an isotropic solution. However, in the solid state, it remains present, albeit often small. The sign of J_{iso} is dependent on the gyromagnetic ratios of each of the spins for the case of single bonds.

Ramsey's theory[63] states that there are precisely five mechanisms that contribute to the total *J*-coupling. Fermi contact (FC) is typically the dominant contribution to *J*-coupling. It is important to recall that s-orbitals have electron density at the nucleus. The FC contribution arises due to the interaction of the electronic spins and the nuclear spins when the electronic density is at the nucleus. Therefore, the FC contribution is typically a good indicator of chemical bonding. The paramagnetic spin orbit (PSO) and the diamagnetic spin orbital (DSO) mechanisms emerge due to the coupling of angular momenta of the electrons around two nuclear spins. The spin dipole (SD) term is simply due to the coupling between the nuclear and the electronic spins. Finally, there exists a $(\mathrm{FC} \times \mathrm{SD})$ cross term which is usually a major contribution ΔJ. It is important to note that the FC mechanism does not contribute to ΔJ.[64]

1.4.4 Other NMR interactions

Other contributions to the total nuclear spin Hamiltonian which arise due to the interaction with a magnetic field are dipolar coupling and quadrupolar coupling. Direct dipolar coupling is a case of nuclear spin coupling, but in this case it is a result of the interaction of the two magnetic dipoles resulting from the magnetic moments of each of the nuclei. It is a through space interaction, as opposed to *J*-coupling, which is a through-bond interaction mediated by interceding electrons. Accordingly, dipolar coupling can be used to measure the distance between nuclei or give global snapshots of macromolecules. [65,66]

The quadrupolar interaction affects nuclei that have spin greater than $\frac{1}{2}$.[10] The quadrupolar interaction arises because these nuclei have a non-spherical distribution of charge within the nucleus. This distribution is expressed as the quadrupole moment, Q, which couples with the electric field gradient (EFG) caused by the nuclei and electrons within the molecule. This interaction is often very strong, so the quadrupolar interaction usually dominates the NMR spectra of quadrupolar nuclides.

Using all of the preceding NMR interactions, it possible to obtain a substantial amount of information about the electronic structure of a molecule. This is the power of solid-state NMR spectroscopy; it is a tool that has the potential to reveal a lot of information that can lead to conclusions about the nature of molecular systems. In this work, solid state NMR is used to reveal the nature of noncovalent chemical bonding between atoms.

1.5 Objectives

It is clear that noncovalent bonds play important roles in every aspect of life and chemistry. It is therefore extremely important to fully understand how they work so as to develop more efficient strategies for dealing with the molecular chemistry and properties of materials.

Previously, there has been only limited analysis of σ-hole bonds involving the Group IV “tetrel” elements. Tetrel bonds with carbon acting as the bond donor are considered to be of great importance since carbon atoms are greatly abundant in nature and in chemistry. Therefore, further research into the area of tetrel bonding is extremely important.

Nuclear magnetic resonance (NMR) spectroscopy is an important tool for furthering the understanding of noncovalent interactions. Work on halogen bonds, using both experimental and computational methods, has demonstrated the sensitivities of chemical shifts, quadrupolar couplings, and *J*-couplings to the halogen bond geometry in crystalline materials.[67,68,69,70,71] In methyl tetrel bonds, it has been shown that the methyl hydrogens surrounding the tetrel bond experience a decrease in their chemical shifts.[72]

The major goal of this thesis is to determine whether the presence or the absence of a tetrel bond can be detected using solid-state NMR. In the present study, investigations into carbon tetrel bonding are expanded using NMR quantum chemical calculations and solid-state NMR spectroscopy with the goal of observing how the presence of carbon tetrel bonds, and their geometries, may affect the NMR response. The NMR parameters observed are chemical shifts, providing an indication of the magnetic shielding on the tetrel atom, and the computed *J*-coupling, giving insights to the connectivity of the tetrel bond.

Chapter 2 - Instrumentation and Methodology

2.1 Sample Preparation

2.1.1 Introduction to Theoretical Aspects of Powder X-Ray Diffraction

The work of this thesis was complemented by an analytical technique known as powder X-ray diffraction (PXRD). Specifically, the identities of the synthesized crystals were confirmed by PXRD as it allows for crystal structural determination using powdered samples. In comparison to single crystal X-ray diffraction, PXRD can be more efficient as it avoids the need for growing single crystals, which can be a long, sometimes laborious, and often costly endeavour.

It has certainly been possible, while not very trivial, to solve *ab initio* a crystal structure using PXRD.[73,74,75] In this work, rather than solving the crystal structure, PXRD results are compared to known data to verify the correct product has been produced.

In PXRD, the sample is bombarded with X-rays from angles set by the user. The range of angles depends entirely on the sample since the signals generated from the X-ray diffraction on the diffractogram are obtained as a function of the angle. In many cases, no diffraction pattern past the angle of 65 degrees may be obtained, while with other samples, the range may be larger or smaller. The peaks in the diffractogram depend ultimately on the crystal structure of the compound.

First, the sample is spread onto a sample plate made of either glass or some metal. It is then placed in the X-ray diffractometer, which consists of a cathode ray tube that generates X-rays. The resulting X-rays are passed through a monochromator in order to filter out unwanted wavelengths of electromagnetic radiation. The X-rays then make contact with the surface of the material, and are either scattered by the atoms in the sample, or passed to the next layer of atoms to either scatter or pass through again. Constructive interference occurs when the X-ray beams from two different layers are in phase. This is detected and shown as a peak on the diffractogram. This process follows *Bragg's Law*:

$$n\lambda = 2d \sin\theta \tag{18}$$

where λ is the wavelength, d is the spacing between the layers, and θ is the incident angle of the X-ray beam. The detector accepts the X-rays at an angle of 2θ from the cathode ray tube as both rotate around the sample, and the diffraction pattern is hence reported as a function of 2θ on the diffractogram. This is known as the *Bragg-Brentano* method.

2.2 Quantum Computational Chemistry

2.2.1 The Hartree-Fock Method and the Self Consistent Field

Quantum computational methods allow chemists to study complex systems existing with more than one electron in order to understand its fundamental properties. *Ab initio* methods have enabled the calculation of the electronic information of complicated systems, which gives researchers better insights into the intricate details of their study. In many fields, quantum computational methods allow for the *de novo* discovery of the properties of various materials which cannot be studied alternatively. However, in this work, quantum chemical computing is used as a means to complement the findings of experimental studies in order to achieve a greater confidence to the solution of a given problem.

In order to successfully employ quantum chemistry, it is important to properly understand the basics of how it works. It is often the case that a person will use a tool at their disposal but it is not always that the user knows how that tool works. In order to fully appreciate the power of quantum computational chemistry, the fundamentals aspects must be understood.

The electronic structure of a system can be described by the solution to the time independent Schrödinger equation. The solution to the Schrödinger equation can be entirely independent of any experimental information, making it a first principles method. Solving the electronic structure is, however, a very difficult task. Except for the case of a single, and sometimes even a dual electron system, it is not computationally feasible to obtain the exact solution. Ab initio methods usually always employ some sort of technique to solving the Schrödinger equation through various simplifications and approximations, and therefore allow for very close estimations of the true solution, but not necessarily the solution itself.

The time independent Schrödinger equation for a ground state system is:

$$\hat{H}\Psi_0 = E_0\Psi_0 \qquad \textbf{19}$$

where the wavefunction describing the spatial distribution of the electronic orbitals is the eigenfunction for the Hamiltonian operator. The ground state energy is returned as the eigenvalue of the wavefunction.

The Hamiltonian operator incorporates a number of terms representing both the kinetic and potential energy of the system.[76] In the simplest of cases, these terms include the kinetic energy of the electrons, the kinetic energy of the nuclei, the attractive electrostatic interaction between the electrons and nuclei, the repulsive electrostatic interaction between electrons and electrons, and the repulsive electrostatic interaction between nuclei. For M nuclei and N electrons, the Hamiltonian operator is thus given by (in atomic units)[76]:

$$\widehat{H} = -\sum_{i=1}^{N}\frac{\nabla_i^2}{2} - \sum_{i=1}^{M}\frac{\nabla_A^2}{2M_a} + \sum_{i=1}^{N}\sum_{A=1}^{M}\frac{Z_A}{r_{iA}} + \sum_{i=1}^{N}\sum_{j>i}^{N}\frac{1}{r_{ij}} + \sum_{A=1}^{M}\sum_{B>A}^{M}\frac{Z_A Z_B}{r_{AB}} \qquad \mathbf{20}$$

where Z is the charge on a given nucleus, and r is the distance between two given particles.

It is possible to see that in the preceding expression, when a greater quantity of nuclei and electrons that are present in the system, the problem becomes extremely complicated. It is for this reason that the Schrödinger equation for relatively large systems cannot be solved.

In order to overcome this critical challenge, the Born-Oppenheimer approximation is applied.[77] Some assumptions inherent in the Born-Oppenheimer approximation are: 1. there is a high ratio of electrons present compared to the number of nuclei; and 2. That an electron is several orders of magnitude less massive than a nucleus. In general, this approximation means that electrons have the ability to change their position instantaneously with respect to the relatively slow motion of the nuclei. This assumption effectively separates the electronic motion from the nuclear motion and considerably simplifies the Schrödinger equation by only incorporating the electronic terms.

While the electronic Hamiltonian appears to be simpler (and, indeed, it is), the wavefunction still cannot be solved for molecules or atoms with more than two electrons. However, it does form the basis for employing various principles and computational methods for solving the electronic structure as an approximation to the true solution for the ground state of a system.

A key principle that must be considered while attempting to solve the Schrödinger equation is called the variation principle.[76] The variation principle states that the energy corresponding to any trial wave function, Ψ_1, will be greater than or equal to the true ground state energy of the system. By using the variation principle, it is possible to start with a known trial wave function, and iteratively minimize the energy such that the resulting trial wave function resembles the true wave function as much as possible. The energy expression can then be parameterized by a value of λ, where the trial energy is calculated for each value of λ. The lowest energy obtained is assumed to be closest to the true energy, satisfying the convergence requirement.

Hartree-Fock (HF) theory was introduced as a means of solving the Schrödinger equation using simplified wavefunctions to estimate the true energy eigenvalue of any system with N number of electrons. HF theory is a computationally feasible system because rather than each electron feeling the Coulombic repulsion of every other electron individually, it essentially considers only the average repulsion felt by a single electron over the total field of all of the other electrons in the molecule.

It is possible to separate the Hamiltonian in terms of a product of all of the individual electrons. In order to do this while satisfying the necessary antisymmetric property of the wave function, a Slater determinant is used. Spin orbitals are introduced when the spin of each atom is considered. The spin orbital depends on both spatial coordinates as well as the spin quantum number, m_s. The spin orbitals are all represented by the four coordinate vector $\mathbf{x}$. As previously mentioned, a spin can have two states, α or β. The spin orbital is represented by $\chi_i(\mathbf{x}_i)$, for each electron, i. The antisymmetry of the wavefunction can be satisfied if the wavefunction is expressed in terms of a Slater determinant[78], where the spin orbitals and the electronic coordinates are represented in the columns and rows, respectively. The Slater determinant provides a wavefunction that is antisymmetric, meaning the electrons cannot occupy the same state. Eqn. **21** shows the Slater determinant representing the Hartree-Fock wavefunction.

$$\Psi(\mathbf{x}_1, \mathbf{x}_2, \dots, \mathbf{x}_N) = \frac{1}{\sqrt{N!}} \begin{bmatrix} \chi_1(\mathbf{x}_1) & \chi_2(\mathbf{x}_1) & \cdots & \chi_N(\mathbf{x}_1) \\ \chi_1(\mathbf{x}_2) & \chi_2(\mathbf{x}_2) & \cdots & \chi_N(\mathbf{x}_2) \\ \vdots & \vdots & \ddots & \vdots \\ \chi_1(\mathbf{x}_N) & \chi_2(\mathbf{x}_N) & \cdots & \chi_N(\mathbf{x}_N) \end{bmatrix} \qquad \mathbf{21}$$

The HF energy can now be solved in terms of the molecular orbitals in the Slater determinant. The wavefunction represented by the Slater determinant which has the lowest possible energy, according to the variation principle, is the wavefunction that most closely resembles the true wavefunction. In order to obtain the lowest energy Slater orbital, the variation principle must also be applied to minimize the spin orbitals. However, in order to solve this energy expression, something must be known about the spin orbitals beforehand, which is not the case. As such, an initial guess is made, and the spin orbital energies are then iteratively minimized through basis sets.

Basis sets are sets of functions which are used to build the HF wave function. The HF wave function is expressed as a Slater determinant formed from each individual molecular orbital. Roothaan expressed the spin orbital in terms of a basis set.[79]

A contracted Gaussian function is essentially designed to reproduce a Slater functional while minimizing computational costs. [76] Thus, a Slater *S*-type orbital, using the aforementioned parameters to mimic real Slater functionals, with M Gaussian functions, is referred to an STO-MG basis set. An increased size of the contracted Gaussian results in a better fit with a Slater functional. However, the increase comes at a severe computational cost, and represents mainly the core orbitals which are generally not of relevance.

Consider the basis set, 6-311++G(d,p). This basis set is composed of 6 Gaussian functions in each of the core orbitals, 3 tight functions, 1 intermediate function and 1 diffuse function. The latter three functions are used to replicate the decay of the Slater-type basis sets. In this particular case, additional diffuse functions are added to each heavy atom (+), and diffuse functions are added to hydrogen (++). Finally, there is a set of d-type polarization functions added to the heavy atoms (before the comma) and p-type polarization functions added to the hydrogens (after the comma). The 6-311++G(d,p) basis set includes polarization functions, diffuse functions and it is triple-zeta, so it is used in this work to provide calculations for cluster model analysis. Other basis sets are possible, such as Dunning's more modern correlation consistent basis sets[80], but these come at a higher computational expense. These basis sets are named by their *zeta*-level, cc-pVXZ, where X is D (double-*zeta*), T (triple-*zeta*), etc. The term "aug" may be added to add diffuse functions in a similar way to the ++ notation.

Each spin orbital has an eigenvalue obtained using the Fock operator, $\hat{\mathbf{f}}(\mathbf{x}_i)$. The operator acts on the spin orbital wavefunction forming the Hartree-Fock equation,

$$\hat{\mathbf{f}}(\mathbf{x}_i)\chi_i(\mathbf{x}_i) = \varepsilon_i\chi_i(\mathbf{x}_i) \qquad \mathbf{22}$$

where the Fock operator is given by

$$\hat{f}(\mathbf{x}_i) = -\frac{\nabla_i^2}{2} - \sum_{A=1}^{M} \frac{Z_A}{r_{iA}} + \sum_{b=1}^{N} [J_b(\mathbf{x}_i) - K_b(\mathbf{x}_i)] \qquad \mathbf{23}$$

The sum of all of the spin orbital energies will therefore give an expression representing the sum of all of the single electron kinetic energies, as well as the sum of all the double electron Coulomb and exchange energies, from the J_b and K_b terms, respectively.

Thus, the HF energy for the system can be expressed as

$$E_{HF} = -\frac{\nabla_i^2}{2} - \sum_{A=1}^{M} \frac{Z_A}{r_{iA}} + \frac{1}{2}\sum_{i=1}^{N}\sum_{j=1}^{N} [J_b(\mathbf{x}_i) - K_b(\mathbf{x}_i)] \qquad \mathbf{24}$$

2.2.2 Møller-Plesset Perturbation Theory

Due to the single-Slater restriction of HF theory, the Hamiltonian does not give the full description of the wavefunction representing the system in question. Møller-Plesset (MP) perturbation theory[81,82,83,84,85] is a post-HF method which introduces a significant amount of improvement over HF by incorporating electron-correlation to the solution of the wavefunction. It is a form of perturbation theory, meaning that it adds the correction to the reference wavefunction by expressing the perturbation as the difference between the desired true Hamiltonian and the reference Hamiltonian, which is the sum of the Fock operators obtained by HF theory. The general case, the desired Hamiltonian is represented as the original unperturbed HF Hamiltonian, H_0, affected by a perturbation, V:

$$H = H_0 + \lambda V \tag{25}$$

where λ is an ordering parameter.

The value of the perturbation is given by[76]:

$$V = \sum_{i=1}^{N}\sum_{j>i}^{N}\frac{1}{r_{ij}} - \sum_{i=1}^{N}\left\{\sum_{b=1}^{N}[J_b(\mathrm{x_i}) - K_b(\mathrm{x}_i)]\right\} \tag{26}$$

MP methods are usually named after the order by which the calculation is performed, with MP2 and MP3 being calculations of second and third order correction to the energy. Even higher order corrections can often be obtained, but are not commonly used due to the costly nature of these calculations. MP1, representing first order perturbation theory, simply regenerates the HF wavefunction, and consequently is not used.

MP2, the second-order correction to the wavefunction, is commonly used MP method due to its relatively high degree of accuracy in representing the true Hamiltonian, at a relatively low cost. The cost is reduced because this method uses the information obtained during an HF calculation in the new calculation. Increasing the perturbation order to the infinite degree, using an infinite basis set, will theoretically yield a perfect wavefunction describing the molecular system in question.

2.2.3 Density Functional Theory

Density functional theory (DFT) is able to provide the ground state properties of most systems and is one of the best methods for computing these properties. Instead of calculating the energy using the orbital wavefunctions in the Schrödinger equation, DFT depends on the electronic density of a system to determine its total energy. This approach was first proposed by Hohenberg and Kohn[86] later to be developed into the DFT method. [87] It has since become one of the most popular, if not the leading method, for solving complex computational problems involving large chemical systems.

As stated, DFT uses the electron density to solve the energy of the system, and not the wavefunction. This was developed to avoid solving the orbital wavefunctions for every electron, as is the case in HF theory. Since the electron density simply depends on three dimensional coordinates, unlike HF theory, where each orbital has three spacial coordinates as well as a spin coordinate, the computational challenge become much less cumbersome.

It was shown that the density functional could be used to solve the electronic energy of a system. [86,87] The density function $\rho(\vec{r})$ is put into an energy functional, so as to obtain an energy.

$$E_{DFT} = E[\rho(\vec{r})] \qquad \mathbf{27}$$

In DFT, the density functional is not known, but various functionals are developed and tested to give the best possible answers for various scenarios. The general form of the functional is given as[76]:

$$E[\rho] = T_s[\rho] + E_{Ne}[\rho] + J[\rho] + E_{XC}[\rho] \qquad \mathbf{28}$$

In the preceding expression, the energy functional depends on the terms incorporating the kinetic energy, $T_s[\rho]$, the electron-nucleus attraction potential, E_{Ne}, the Coulombic interaction between electrons, J, and the exchange-correlation, E_{XC}. All of these functionals are simply added together to obtain the total DFT energy.

In order to ensure the antisymmetry principle is obeyed, spin is introduced. [87] This is found in the T_s functional, where the electrons are assumed to be non-interacting. The electronic density is obtained through this approach, but introduces some approximation to DFT due to its reliance on HF theory.

The functional representing nuclear attraction is simply the interaction between the nucleus and the electron density over all space. The Coulombic repulsion term is similar in that it is the repulsion between two given electron charge distributions over a given area.

Finally, the exchange correlation term, E_{XC}, accounts for the correction to the energy due to the exchange energy (which is already treated in HF but not directly in DFT) as well as the fact that there is indeed electron correlation that is not incorporated into the kinetic energy term. The exchange-correlation functional is not known; it can, however, can be guessed.

There are many different types of DFT, each one differing in its approach to the exchange-correlation correction. The simplest is known as the Local Density Approximation (LDA).[76] In this approach, the charge felt by the electron density is assumed to be constant over the space at which each point in the electronic density is probed, an unrealistic prospect.

An improvement over LDA, known as the Generalized Gradient Approximation[88] (GGA) is used in this work. In this case, the exchange-correlation functional is dependent on both the electron density and the derivative thereof, which gives the change of the electron density over space. This class of functionals gives a better picture of the electron density over space as it better reproduces the true state of the system.

The best attempt at approximating the exchange-correlation functions is through the hybrid DFT approach. In short, hybrid DFT utilizes a bit of everything, so to speak. In fact, this class of functionals incorporates both exchange from HF theory as well as correlation from DFT, and other sources depending on the functional. One of the most popular functionals is B3LYP.[89,90] In this functional, the HF exact exchange is used, as well as the LDA exchange and correlation. The GGA term is simply the LYP correlation functional. The generalized expression is given as:

$$E_{XC}^{B3} = (1-a)E_X^{LSDA} + aE_X^{HF} + b\Delta E_X^{B88} + (1-c)E_C^{LSDA} + c\Delta E_C^{GGA} \qquad \textbf{29}$$

where a, b, and c are variable parameters.

DFT has difficulty modelling certain interactions. In general, DFT has difficulty modelling long range interactions. [91] For example, radical-molecule interactions are prone to error due to limited exchange modelling the charge transfer. [92] Similar issues arise with other noncovalent interactions because DFT cannot properly model electron density over longer distances, and so the exchange potential is represented by $-\frac{0.2}{r}$, where the ideal case would be seeing the exchange potential treated as $-\frac{1}{r}$. [91,91] However, some hybrid DFT functionals attempt to overcome these problems. These include BHandHLYP[93], which uses a mixture of both DFT and HF exchange energies and CAM-B3LYP[94] (CAM = Couloumb attenuating method), which introduces long range corrections in order to better treat noncovalent interactions. PBE is a functional which has both exchange and correlation correction incorporated. When this functional is corrected for long range, it is referred to as ωPBE, or LC-ωPBE[95,96,97] (ω = 0.40 a.u.), depending on the corrections used. The M05[98] and M06[99] family of functionals are meta-GGA approaches to the exchange and correlation correction. The preceding functionals have all been used in this thesis to evaluate the interaction energies, as well as the NMR parameters of various simple compounds.

2.2.4 Computation of NMR Parameters using DFT

DFT is a useful computational method for calculating the magnetic properties of atoms and molecules when they are under the influence of a magnetic field. In computing properties such as magnetic shielding and spin-spin coupling, the chemist has the ability to predict the outcome of NMR experiments. Additionally, DFT computational results may provide complementary information to support the experimental findings of an NMR study.

When a molecule is subjected to an external magnetic field, the electrons are perturbed in such a way that their properties are altered by the field. In DFT, the magnetic properties of the electrons can be derived from the first and then second derivatives of the total energy of the system with respect to two different perturbations, under the assumption of a static magnetic field. In other words, all of the information needed to obtain magnetic properties are within the wavefunction of the system.[100]

Nuclear shielding constants as well as indirect spin-spin coupling constants are obtained from the derivative of the electronic energy of the system with respect to the magnetic induction, and the nuclear magnetic moments to obtain the various contributions to the *J*-coupling. [101] The second derivative is performed to determine further the magnetic properties of the system. This is essentially derived from the electronic Hamiltonian for the system, whereby the Hamiltonian is altered slightly for the dependence on the external magnetic field.

DFT is, of course, an approximation method to solve the total energy of the system. In doing so, it uses basis sets in order to represent molecular orbitals. When an infinite size basis set is used, a perfect solution can be obtained. However, this is not possible, and introduces the so-called "gauge origin problem" to the calculation of NMR parameters. It is a problem that exists as a result of improper description of the magnetic field.[102] This is solved through the implementation of the gauge-invariant atomic orbitals (GIAO) method[103], being the default option in the *Gaussian* software.

2.2.5 Gauge Including Projector Augmented Wave DFT Calculations

Gauge Including Projector Augments Waves (GIPAW) DFT calculations [104] are conducted on known crystal structures to obtain NMR parameters. GIPAW DFT is important because it is able to account for the long-range effects of the crystal lattice on the NMR properties, giving rise to more accurate results than in methods using single molecules. GIPAW DFT is implemented in the CASTEP-NMR software code.[105]

Periodic boundary conditions are used to compute the total energy of a bulk crystalline system. Since a crystalline material is made up of repeating unit cells, GIPAW DFT is extremely useful for calculating NMR parameters of crystal structures in the solid state. The main advantage of GIPAW DFT is that it is able to produce fairly accurate results at a reasonable computational cost, whereas other traditional methods of DFT would not be able to achieve similar results without astonishing computational cost.

In the GIPAW method, there are several factors that must be considered. First, a plane wave basis set must be specified. Plane wave basis sets are used because of their improved treatment of periodic systems. In addition, in order to minimize the number of nodes in the core wavefunction due to the higher kinetic energy of the electrons, pseudopotentials provide an alternative that replicates the core such that the computation can proceed better.[106] Finally, a cut-off energy is set in order to define the level of convergence for the calculation.

2.2.6 Counterpoise Correction

Counterpoise (CP) correction[107] is used in computational chemistry in order to reduce basis set superposition error (BSSE). When calculating bimolecular interactions, it is important to consider the effect of BSSE because in the calculation of the complex, there will be an artificial lowering of the overall energy because of the sharing of basis functions between the nearby monomers.[108] CP-correction provides a good way to correct for this error, showing good results for noncovalent interactions at higher level calculations, such as MP2.[109]

In the CP-correction program, the energy is calculated a number of times in Gaussian:

1. Dimer
2. Monomer 1 with dimer centred basis set (DCBS 1),
3. Monomer 2 with dimer centred basis set (DCBS 2)

4. Monomer 1 with monomer centred basis set (MCBS 1)

5. Monomer 2 with monomer centred basis set (MCBS 2)

The CP-corrected energy is thus given by a simple formulation of all of the calculated energies[110] (eqn. **30**).

$$E^{CP} = E_{dimer} - E^{1}_{DCBS} - E^{2}_{DCBS} \tag{30}$$

The resulting energy value obtained from a calculation is the interaction energy (as a function of intermolecular distances or angles). This is, however, different from binding energy. In order to find the binding energy, the monomers are geometry optimized, then the dimer is again geometry optimized at a fixed distance (2.825 A). The resulting energy is the binding energy. The interaction energy is then the energy obtained when the geometries are then frozen and the interaction distance is changed.

The NMR values are obtained from the output files from the dimer calculation. There has been a study looking into the impact of BSSE on magnetic shielding constants. However, for ^{13}C and ^{15}N, these corrections are normally on the order of 0.2 ppm for magnetic shielding and 0.01 Hz for *J*-coupling (own data). As such, for the purpose of revealing NMR trends, the CP-correction is not used to obtain corrected NMR parameters; only interaction energies.

2.3 Experimental Methodology of SSNMR

2.3.1 Experimental Setup

The NMR spectrometer (**Figure 9**) consists of several components which, when acting together, allow the user to collect an NMR spectrum of a compound of interest, whether it be in the liquid state or in the solid state. The major components of interest are the magnet, the transmitter, the probe and the receiver.

The magnet provides the experiment with a strong, essentially homogenous magnetic field in order to induce the *Zeeman* interaction, the fundamental process which gives rise to the NMR transition. The energy corresponding to the NMR transition is dependent on the strength of B_0, so in the absence of a magnetic field, it would be difficult to observe an NMR spectrum.

Figure 9. A 9.4 T NMR spectrometer magnet for the solid state. The superconducting coil is found within the large cylindrical container, which also houses the cooling liquid.

2.3.2 Magic Angle Spinning

Magic angle spinning is a technique used in SSNMR which has the ability to reduce or eliminate the anisotropies of certain NMR interactions such as dipolar coupling and chemical shift anisotropy, which are orientationally dependent.[111,112,113] MAS mimics the isotopic tumbling of molecules in solutions through motional averaging. In solids, MAS can reduce the anisotropies of chemical shift anisotropy, heteronuclear dipolar coupling anisotropy and the *J*-coupling interaction anisotropy.[111] Finally, the quadrupolar effect is only partially averaged. In most cases, MAS has the average effect of sharpening the NMR signals to yield liquid-like spectra. Its importance is very clear when it comes to the analysis of complex spectra with many peaks at different chemical shifts. It is thus useful in chemical shift assignment, or when changes in chemical shifts must be probed. However, due to the reduction of the anisotropies, MAS has the effect of reducing the ease of observing some anisotropic NMR parameters. Therefore, often times the NMR spectroscopist will also perform static NMR experiments, where the sample remains motionless in the coil.

The need for MAS comes from the dependence of the angle of the PAS of certain NMR interactions, such as magnetic shielding, with respect to B_0 (eqn. **31**). This dependence is contained within a term in each of the respective Hamiltonian operators.

$$3\cos^2\theta - 1 \qquad \textbf{31}$$

θ is the angle between the magnetic field and the z-axis of the interaction tensor. Consequently, when $\theta = 54.74^{\circ}$, or the *Magic Angle*, the term is forced to zero. Thus, when a sample is rotated around the magic angle axis, the averaging of the anisotropies occurs.

In order for the procedure to work, the spinning rate must be fast compared to the anisotropy of the interaction, because there is a dependence of the $\cos\theta$ term on the angular velocity of the spinning rotor.[114,115] As such, the faster the spinning speed, the more isotropic the spectrum becomes. [59] A set of spinning side bands will be present, separated from the isotropic peak by intervals of the spinning speed, in Hz. At the time of writing this thesis, some of the fastest spinning rates of 111 kHz and 110 kHz that have been made commercially available have been achieved by Bruker and JEOL, on their 0.7 mm[116] and 0.75 mm[117] CP/MAS probes, respectively.

2.3.3 Sensitivity Enhancement

2.3.3.1 Cross-Polarization

Cross-polarization (CP) is a technique used to improve the signals of spin-$\frac{1}{2}$ nuclei which often have low natural abundance (n.a.) or are sparse within the sample (such as in the case of ^{13}C, n.a.= 1.1%) This technique is made possible due to the possibility for some nuclei to transfer their polarization to other nuclei. In cases where the n.a. of the NMR active nucleus is very low (< 1%), a CP experiment can drastically increase the signal-to-noise ratio, and decrease the experimental time required in order to obtain decent results.

A CP experiment takes advantage of the fact hydrogen atoms possess an inherently larger magnitude of polarization compared to other atoms of interest, such as ^{13}C, ^{15}N, and ^{31}P, among others. This abundance in polarization is due to the protons' gyromagnetic ratio, γ, which is much larger than most other NMR active nuclei. The CP experiment will work when the pulse applied to both the proton frequency channel and the frequency channel of the nucleus of interest satisfies the Hartmann-Hahn matching condition[118], meaning, the nuclear precession frequencies become matched, thereby allowing a transfer of spin polarization.

The Hartmann-Hahn matching condition can be demonstrated by first recalling that ΔE depends on the gyromagnetic ratio and the magnetic field. If two nuclear spins, ^{1}H and R, are coupled, and the application of an RF field induces local magnetic fields, then

$$hv_{^1\mathrm{H}} = \gamma_{^1\mathrm{H}}\beta_1(^1\mathrm{H}) \tag{32}$$

$$hv_R = \gamma_R\beta_1(R) \tag{33}$$

where B_1 is the oscillating field generated by the respective nuclei. The Hartmann-Hahn condition is fulfilled when:

$$\gamma_{^1\mathrm{H}}B_1(^1\mathrm{H}) = \gamma_B B_1(R) \tag{34}$$

so these two terms are matched by a common rf pulse.

A typical single pulse program using CP is shown in **Figure 10**. Following the 90° pulse, a contact pulse is applied during which there is a transfer of polarization from the spin A to spin B. Proton decoupling is applied during acquisition to ensure that maximum sensitivity is gained on the nucleus of interest without interference from proton coupling.

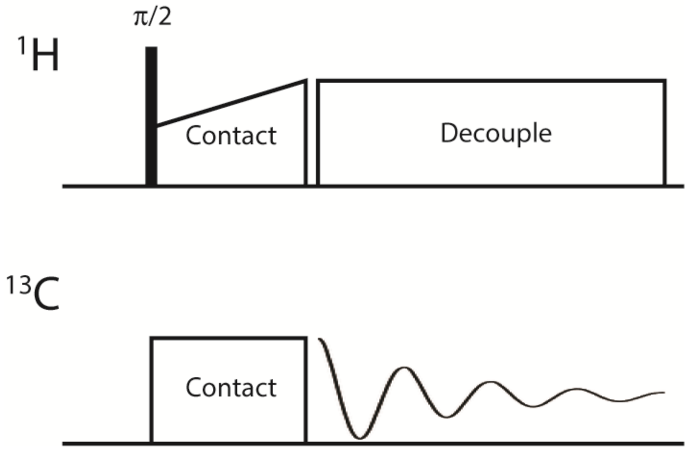

Figure 10: Typical single pulse cross polarization pulse program. A $\frac{\pi}{2}$ pulse is applied to the proton channel, followed by a ^{1}H → ^{13}C contact time. This is followed by the acquisition period coinciding with decoupling from the protons.

2.3.3.2 Data Acquisition Periods

A physical parameter that can be changed is the number of transients, or scans, that are obtained in the experiment. The signal to noise ratio is very much dependent on this number. As the number of transients increases, so does the signal-to-noise ratio. Consequently, depending on the natural abundance of the nuclide being observed, it is typical for an experiment to acquire hundreds, if not thousands of samplings to obtain a good end signal. The signal intensity can be described as increasing as the square root of the number of scans (eqn. **35**).

$$\frac{S}{N} = \sqrt{n_{\text{scans}}} \qquad \mathbf{35}$$

Therefore, four times the number of scans is required to double the signal intensity with respect to the background noise. However, the preceding expression shows that the signal to noise ratio becomes limited as a function of time. As such, it is necessary to balance the experimental time with the desired signal intensity.

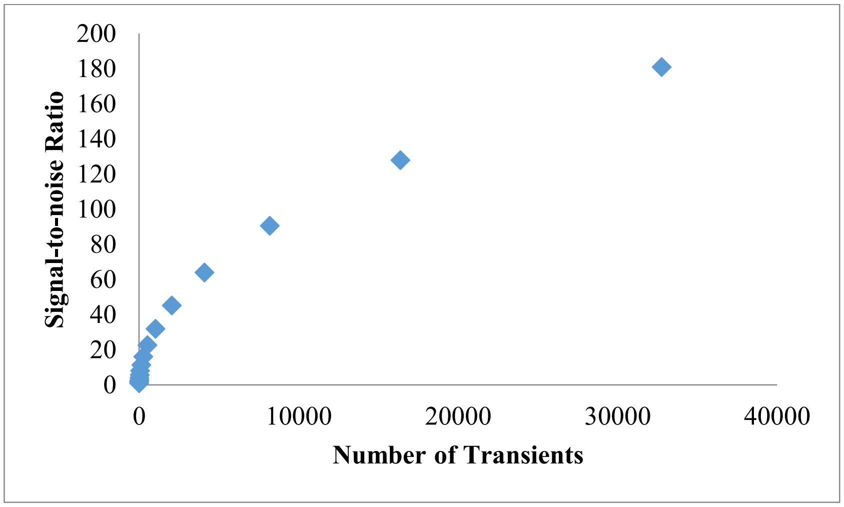

Figure 11. The increase of the signal-to-noise ratio as a function of the number of time dependent scans. Initially, the signal intensity grows rapidly, but as time continues to increase, the interval at which the signal gain is achieved becomes impractically long.

2.4 Experimental Methods

2.4.1 Sample Preparation

Crystal structures exhibiting carbon tetrel bonds were selected from the CSD. Conquest version 1.17 was used in conjunction with CSD version 5.36 with the November 2014 update, and the structures were visualized in Mercury version 3.5.1. The compounds were chosen based on the criteria described in Chapter 3.

Salts containing tetrel bonds were investigated: sarcosinium tartrate, sarcosine maleate and of N,N,N’,N’-tetramethylethylenediammonium succinate succinic acid.

Sarcosine was obtained from Sigma-Aldrich and used without further purification, and the salts were collected according to the published procedures.[44, 119,120]

2.4.2 Powder X-ray Diffraction – Experimental Methods

The sample purity was confirmed by powder X-ray diffraction, using a Rigaku Ultima IV X-ray diffractometer, with the Bragg-Brentano method with a monochromator with CuKα_1 radiation (λ = 1.54060 Å). Diffractograms were collected at room temperature (298 ± 1 K) and with 2θ values ranging from 2° to 5°, to 80° in increments of 0.02°. Diffractograms were analyzed using the Rigaku PDXL 2 software and compared to existing diffractograms in the PDF-2 2.1302 database and simulations generated using the Mercury version 3.5.1 software provided from the Cambridge Crystallographic Data Centre (CCDC) (CCDC entry numbers are 660888 and 159986, 142944 and 237950 for sarcosine, sarcosinium tartrate, N,N,N',N'-tetramethylethylenediammonium dichloride and of N,N,N',N'-tetramethylethylenediammonium succinate succinic acid, respectively).

2.4.3 Cluster Model Analysis

Computations on a library of model compounds were done several times, for comparison, using B3LYP, MP2, BH&HLYP, CAM-B3LYP, LC-ωPBE, and LC-ωPBE-D3 (D3 refers to the addition of Grimme's dispersion[121]) methods with the Gaussian 09 software[122] on the Wooki cluster at the University of Ottawa. While the MP2 method cannot calculate the NMR parameters, it is chosen as a method for comparing the energy calculated by various DFT methods because it is able to properly treat noncovalent interactions.

In addition, a series of other functionals were also used to establish a cost benchmark to identify the best functionals for calculating tetrel bonding energies (**Table 2**). The model compounds were constructed and visualized via GaussView 4.1 software for Microsoft Windows.[123] All calculations were conducted with the 6-311++G(d,p) basis set. The tetrel bond donor and acceptor moieties were each first geometry optimized using both density functional theory (DFT) methods, or MP2. The DFT optimized precursors were combined to form the tetrel-bonded systems that would be examined by various DFT methods, and the MP2 optimized precursors were combined into models that would be analyzed via MP2. In all cases the carbon tetrel bond length was set to 2.825 for geometry optimization. These tetrel bonded models were then again geometry optimized by both DFT and MP2 methods using counterpoise (CP) correction. Once optimized, the DFT and MP2 NMR parameters were calculated. The GIAO method was used for magnetic shielding, specifying iop33(10=1) in order to compute paramagnetic and diamagnetic contributions to the magnetic shielding constants. Examples of Gaussian input files are in Appendix II – Sample of Computation Input Files. EFGShield version 4.2 was used to extract the NMR parameters.[124] Magnetic shielding constants were then converted to chemical shift values with respect to the shielding constant for tetramethylsilane (TMS), 184.1 ppm.[125] Total *J*-coupling values were extracted manually from the Gaussian output files calculated by DFT methods when the "spinspin" keyword was specified. Taking into account basis set superposition error (BSSE), CP-corrected interaction energies were obtained in units of kcal/mol and reported in this work.

2.4.4 Solid-State NMR

^{13}C solid-state NMR was conducted at 9.4 T (ν_L(^{13}C) = 100.613 MHz) under MAS conditions ($\theta = 54.74°$) on an AVANCE III NMR spectrometer. Cross polarization experiments (ν_L(^{1}H) = 400.130 MHz) were performed with a spinning rate of 6 kHz in a Bruker 4 mm HXY probe. Spectra were referenced externally to glycine at 176.4 ppm. In each case, the contact time was 5000 μs and the proton 90-degree pulse was 3.00 μs. Several thousand transients were typically acquired using a relaxation delay of 5 s.

Figure 12. A 4 mm MAS rotor compared to a Canadian Penny for scale. The cap of the rotor is winged so that it may spin using a high pressure air stream. The spinning speed is adjusted using an MAS controller fit onto the spectrometer console.

2.4.5 GIPAW DFT

GIPAW DFT calculations were carried out using the CASTEP-NMR software version 4.4[126,105] on the Wooki cluster at the University of Ottawa. This was done in order to properly treat the effects of the crystal lattice. Crystallographic information files were imported into Materials Studio v. 4.4 (Accelrys) to generate input files. In all cases, the generalized gradient approximation (GGA) with the functional of Perdew, Burke, and Ernzerhof (PBE)[127] using on-the-fly ultrasoft pseudopotentials[128,129] was employed. Geometry optimization for the hydrogen atoms, followed by NMR calculations on the sarcosine salts, were performed with a 550.0 eV cutoff at the "fine" setting for the *k*-point grids. The calculation for sarcosine was conducted using a 610.0 eV cutoff at the "ultra-fine" setting for the *k*-point grids. No geometry optimization was performed for sarcosine. NMR parameters were extracted from the CASTEP NMR output file using EFGShield version 4.2.[124]

Chapter 3 - Results and Discussion

3.1 Computational Investigations of NMR Trends in Tetrel Bonds

In this study, computational investigations were performed on a library of model systems containing carbon tetrel bonds (**Figure 14**). It was previously demonstrated that regions of negative charge energetically favour a weak interaction with the methyl carbon of interest, especially when the methyl carbon is bonded to a strong electron-withdrawing substituent.[54] As discussed by Torres and DiLabio, DFT methods such as B3LYP often cannot accurately describe medium to long range non-covalent interactions without some sort of correction.[91] Yet, the use of DFT is highly desirable because it can provide rapid and accurate *J*-coupling values, an important NMR parameter providing structural information, which can be used to probe the tetrel bond. A number of solutions have been offered to overcome the shortfalls of DFT, including the use of dispersion correction,**[121]** and the packaging of improved exchange-correlation, as in the case of the M06 suite of functionals.[91] In order to describe the tetrel bonding interaction energy, a study was performed to determine a set of density functionals that could best represent the tetrel bond.

Model 6 (**Figure 14**) was chosen as the standard for this test. It was chosen due to its relatively simple structure, and because it possesses a negative charge. The carbon tetrel bond length was fixed at 2.825 Å, and the geometry was optimized by B3LYP/6-311++G(d,p) with CP correction. The CP corrected bonding energy was obtained, using the 6-311++G(d,p) basis set, for each of the functionals that were tested (**Table 2**). In each case, the bonding energy was compared to the QCISD bonding energy, -2.72 kcal/mol.

Table 2. Functionals compared to QCISD in order to set a benchmark for determining the highest performing functional as it applies to carbon tetrel bonding.

Density Functional	Correction	CP corrected energy / a.u.	CP corrected bonding energy / kcal/mol
M06-2X	D3	-285.03	-4.53
M06-2X	-	-285.03	-4.40
M06-HF[130,131]	-	-285.05	-4.61
LC-ωPBE	D3	-284.92	-4.74
LC-ωPBE	-	-284.98	-2.57
CAM-B3LYP	D3	-284.98	-5.21
CAM-B3LYP	-	-285.05	-3.33
BHandHLYP	-	-284.99	-3.04
B3LYP	D3	-285.10	-4.77
B3LYP	-	-285.17	-2.45
HF	-	-283.51	-1.83
CCSD[132,133]	-	-284.42	-2.72
QCISD[134]	-	-284.43	-2.72

A few functionals provide results within a relatively small difference of 0.5 kcal/mol from the bonding energy obtained using QCISD (-2.72 kcal/mol), these being LC-ωPBE, B3LYP, and BHandHLYP. CAM-B3LYP is also close but yielded an energy difference of 0.61 kcal/mol. Given the relative costs (**Figure 13**), the functionals that were chosen to proceed representing a good mix of correlation and dispersion corrections that were chosen for further calculations were B3LYP, BHandHLYP, CAM-B3LYP, LC-ωPBE and LC-ωPBE-D3. We note that all of the M06 functionals took significantly longer and yielded results which were further away in magnitude from the QCISD result.

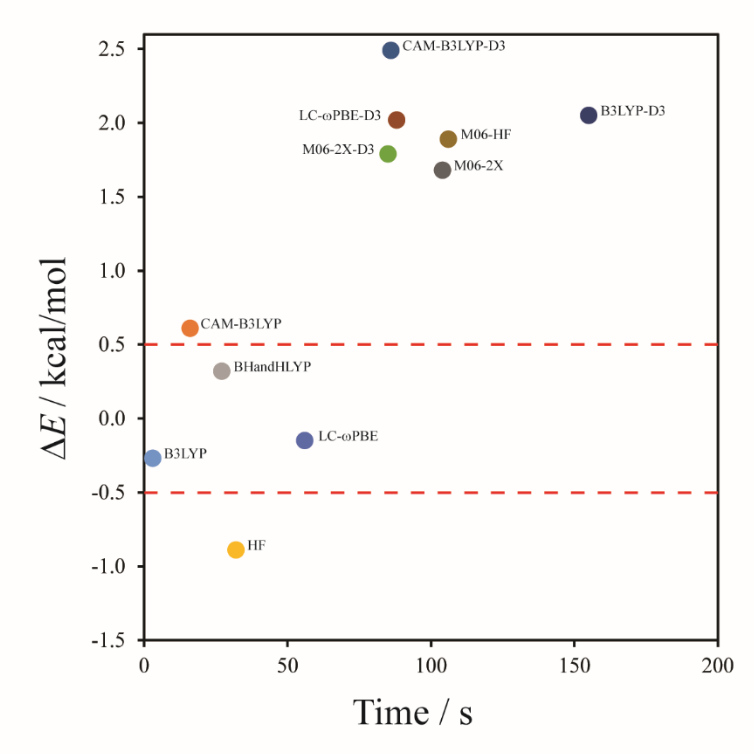

Figure 13. Cost analysis of the various methods used in the test study on model 6. The red hashed line represents the energy difference cut-off for this study at 0.5 kcal/mol, as compared to the energy obtained in the QCISD calculation. All energies are at a tetrel bond distance of 2.825 Å. The time taken for the QCISD calculation was 5,232 s.

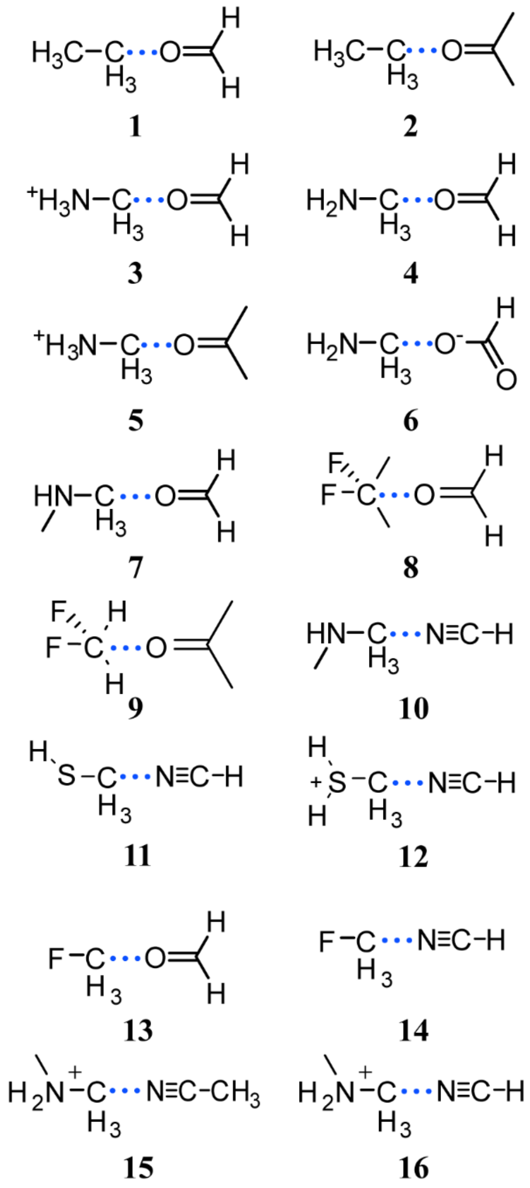

Figure 14. Model compounds containing carbon tetrel bonds between methyl carbons and oxygen-containing functional groups.

To explore trends in the NMR parameters, the LC-*ω*PBE, LC-*ω*PBE-D3, BHandHLYP, B3LYP functionals, as well as the MP2 method, were used to perform calculations of magnetic shielding tensors, on each of the compounds in the library (**Figure 14**), using the 6-311++G(d,p) basis set in Gaussian 09.[122] Model structures were constructed with carbon tetrel bond lengths increasing in 0.10 Å increments from 2.825 Å to 3.325 Å (**Figure 15**), just over the sum of the vdW radii between carbon and oxygen, and carbon and nitrogen, 3.22 Å and 3.25 Å, respectively.

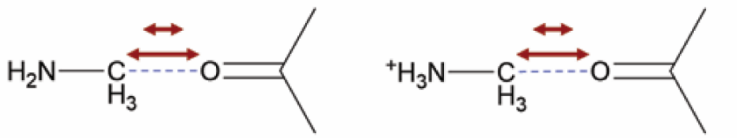

Figure 15. A schematic showing how the tetrel bond lengths of the model compounds are modified for the computations. The bond lengths are changed in 0.10 Å increments from 2.825 Å to 3.325 Å. The atomic coordinates are modified in the GaussView software.

The results for δ_{iso} are presented graphically in **Figure 16**. At the time of this work, in the vast majority of reported crystal structures, carbon tetrel bonds between methylamine and oxygen have interaction lengths greater than 2.8 Å. However, there are a few cases where the distance is shorter. The smallest value in the database is 2.591 Å,[135] and the shortest carbon tetrel bond between methylamine and a carboxylic acid is 2.825 Å.[136]

This analysis was done in order to expand the overall understanding of how the ^{13}C chemical shift of methyl group involved in a R-C···Y tetrel bond (R = C, F, N, N^{+1}, S or S^{+1}; Y = O, O^{-1}, or N) changes as a function of the interaction distance. The response of the chemical shift to the tetrel bond angle was also assessed. The structures were constructed with tetrel bond lengths of 2.925 Å, then varying the R-C···Y angle in increments of 5° between 140° and 180°. This provides an adequate range over which to test chemical shift response to the changing geometry of the tetrel bond and has been used previously as the relevant range over which to search the CSD for existing tetrel bonded compounds.[58]

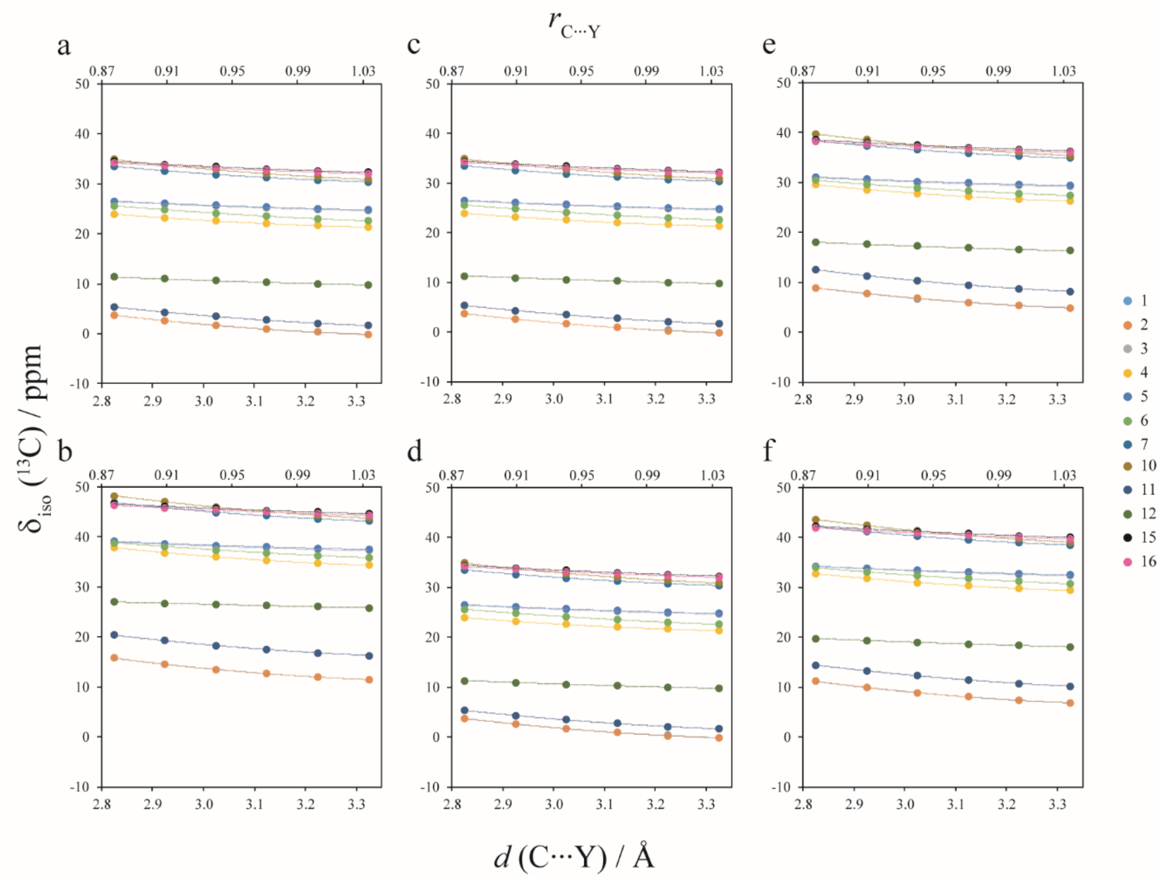

Figure 16. NMR computational investigations of model compounds. Calculated isotropic chemical shifts of model compounds using (a) MP2, (b) B3LYP, (c) LC-ωPBE, (d) LC-ωPBE-D3, (e) BHandHLYP, and (f) CAM-B3LYP are plotted against the reduced distance parameter ($r_{C\cdots Y}$) (top axis) and the interaction distance (d (C···Y)) (bottom axis). Each plot is fit by a quadratic polynomial function with $R^2 > 0.99$ for all methods except CAM-B3LYP (**Table 12-Table 17**). For spacing, data values for structures **8, 9, 13** and **14** are found in **Table 6** to **Table 8** in Appendix I – Supplementary Data.

The model compounds are varied by the nature of their chemical structures and their substituents, while the change in the C···Y tetrel bond distance remained consistent across all of the examples (**Figure 14**). We also propose the use of the normalized distance parameter,

$R_{X\cdots Y}$, to measure the chemical shift response as well as the interaction energy as a function of the interaction length (where the interaction distance is divided over the sum of the vdW radii), as has been done for halogen bonds (eqn. **36**).

$$R_{X\cdots Y} = \frac{d_{X\cdots Y}}{\sum d_{VDW}} \qquad \mathbf{36}$$

Interestingly, in each case, the calculated ^{13}C chemical shift increases quadratically as the carbon tetrel bond length decreases, indicating of a correlation between the tetrel bond strength and the chemical shift. This trend is not unexpected; it is reproduced experimentally in ^{81}Br halogen bonding, where the ^{81}Br chemical shift increases significantly with the shortening of the halogen bond distance, albeit with the possible competing effects of hydrogen bonding.[137] The polynomial function is stable beyond the vdW distance. The computational data therefore suggest that, experimentally, the introduction of a carbon tetrel bond should result in a positive ^{13}C chemical shift on the order of up to 5 ppm. We note that in the case of fluoro-substituted compounds (**8** and **9**), the computed chemical shift difference is on the order of less than 1 ppm, albeit following the same trend. We note that while each functional provides a different magnitude of chemical shift, they all show similar trends.

CP corrected interaction energies are reported in **Figure 17**. These computations show that there is indeed a dependence of the interaction energy on the interaction distance. Sometimes a local minimum is reached over the relevant range of distances, while sometimes these minima reside closer or farther. However, there is no clear correlation with chemical shift trends. Therefore, it can be expected that the presence of a tetrel bond, whether it is a favourable or unfavourable interaction energetically, will provide the same chemical shift trends as a function of distance.

A further analysis of the computed results (**Figure 16**) reveals that for the neutral models (**Figure 14**), the chemical shift trend is largely dominated by changes in the paramagnetic contribution, σ_p, to the magnetic shielding constant, σ (**Table 3**). Conversely, for the charged models, the changes in the diamagnetic contribution, σ_d, are on the same order of magnitude as the changes in the paramagnetic contribution. Also notable is that the overall change in the magnitude of σ between B3LYP and LC-ωPBE is largely a result of the change in the magnitude of the σ_p values, reflecting the latter's ability to better handle longer range corrections. The paramagnetic contribution involves the mixing of virtual orbitals with the ground electronic state (eqn. **37**), while the diamagnetic contribution reflects the structure of the ground electronic state (eqn. **38**). A favourable overlapping of the ground state orbitals (0) with the excited state orbitals (n) results in paramagnetic deshielding. Given that the overall changes to the chemical shift are very small relative to the total range of known ^{13}C chemical shifts, it is unproductive to attempt to further attribute the contributions to specifics of the electronic structure of the tetrel bond.

$$\sigma_p^{\alpha\beta} = -\left(\frac{\mu_0}{4\pi}\right)\left(\frac{e^2}{2m}\right)\sum_{n\neq 0}\left\{\frac{\langle 0|\sum_k r_k^{-3}\hat{l}_{k\alpha}|n\rangle\langle n|\sum_k \hat{l}_{k\beta}|0\rangle + \langle 0|\sum_k \hat{l}_{k\beta}|n\rangle\langle n|\sum_k r_k^{-3}\hat{l}_{k\alpha}|0\rangle}{{}^1\varepsilon_n - \varepsilon_0}\right\} \qquad \textbf{37}$$

$$\sigma_d^{\alpha\beta} = \left(\frac{\mu_0}{4\pi}\right)\left(\frac{e^2}{2m}\right)\left\langle 0\left|\frac{r^2\delta_{\alpha\beta} - r_{h\alpha}r_{h\beta}}{r_k^3}\right|0\right\rangle \qquad \textbf{38}$$

where μ_0 is the mass of an electron, and $\delta_{\alpha\beta}$ is a Kroeneker delta, and the other terms are previously defined.

Computed ^{13}C chemical shift anisotropies (CSA, Haeberlen convention) for the model compounds range from about 15 ppm for symmetric models (i.e., **1** and **2**; (*d* = 3.325 Å)) to a high of almost 116 ppm for **14** (*d* = 2.825 Å) (**Table 4**). In all cases, the CSA increases as the tetrel bond shortens.

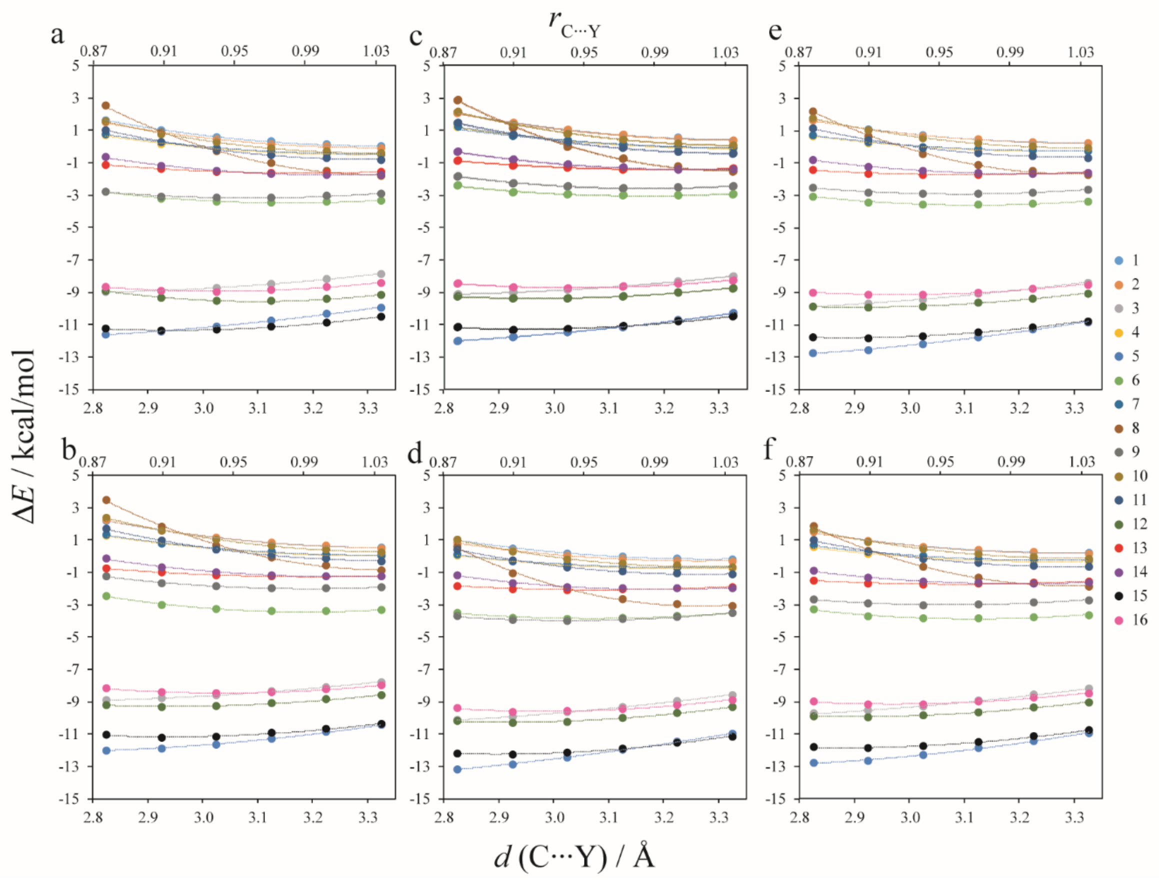

Figure 17. Computed CP corrected interaction energy values vs. interaction distance of the model compounds. Computed interaction energies using (a) MP2, (b) B3LYP, (c) LC-ωPBE, (d) LC-ωPBE-D3, (e) BHandHLYP, and (f) CAM-B3LYP are plotted against the reduced distance parameter ($r_{C\cdots Y}$) (top axis) and the interaction distance (d(C···Y)) (bottom axis). The calculated interaction energies of the model compounds were obtained by 6-311G++(d,p) with each respective functional. Each plot is fit by a quadratic polynomial function with $R^2 > 0.96$ (**Table 12** to **Table 17** in Appendix I – Supplementary Data).

Table 3. Computed values of the diamagnetic and paramagnetic contributions to the magnetic shielding constants (σ_d, σ_p, and σ_t) for the model structures. Values were calculated by B3LYP and LC-ωPBE using the 6-311++G(d,p) basis set.

		B3LYP			LC-ωPBE		
Model Structure	Interaction Distance / Å	σ_d	σ_p	σ_t	σ_d	σ_p	σ_t
1	2.825	247.58	-79.22	168.37	247.81	-67.42	180.39
	3.125	246.80	-75.34	171.47	246.71	-63.52	183.19
	3.325	246.51	-73.85	172.66	246.25	-61.99	184.26
2	2.825	247.74	-79.39	168.34	246.76	-66.41	180.35
	3.125	247.54	-76.10	171.44	246.59	-63.37	183.22
	3.325	247.48	-74.79	172.69	246.57	-62.27	184.30
3	2.825	255.59	-110.45	145.14	257.13	-99.42	157.71
	3.125	256.26	-109.89	146.37	257.69	-98.77	158.92
	3.325	256.64	-109.73	146.92	258.06	-98.59	159.47
4	2.825	250.02	-103.79	146.23	251.24	-91.04	160.20
	3.125	250.35	-101.54	148.81	251.20	-89.14	162.06
	3.325	250.55	-100.73	149.81	251.25	-88.45	162.80
5	2.825	259.65	-114.58	145.07	262.58	-105.05	157.54
	3.125	260.08	-113.92	146.16	263.34	-104.62	158.72
	3.325	260.32	-113.63	146.69	263.80	-104.51	159.29
6	2.825	250.11	-104.92	145.19	251.03	-92.52	158.52
	3.125	250.86	-103.60	147.26	251.76	-91.17	160.58
	3.325	251.25	-103.04	148.21	252.21	-90.68	161.53
7	2.825	249.77	-112.55	137.22	250.88	-100.30	150.58
	3.125	250.06	-110.15	139.91	251.02	-98.23	152.80
	3.325	250.22	-109.27	140.95	251.16	-97.47	153.69
8	2.825	245.88	-198.11	47.78	248.08	-185.82	62.26
	3.125	245.44	-197.46	47.98	247.18	-184.78	62.40
	3.325	245.13	-197.04	48.09	246.68	-184.19	62.49
9	2.825	249.33	-182.74	66.59	249.39	-171.76	77.63
	3.125	249.85	-182.97	66.88	249.83	-171.99	77.84
	3.325	250.18	-183.17	67.01	250.15	-172.17	77.98
10	2.825	249.58	-113.75	135.83	251.28	-102.04	149.24
	3.125	249.59	-110.56	139.04	251.06	-99.05	152.01
	3.325	249.63	-109.25	140.38	251.00	-97.80	153.20
11	2.825	249.97	-86.20	163.77	250.47	-71.70	178.77
	3.125	249.42	-82.79	166.64	249.92	-68.53	181.40
	3.325	249.09	-81.24	167.84	249.52	-67.02	182.50

12	2.825	249.48	-92.30	157.18	251.46	-78.61	172.86
	3.125	248.83	-90.89	157.94	250.67	-76.80	173.88
	3.325	248.50	-90.14	158.36	250.21	-75.81	174.40
13	2.825	248.16	-143.09	105.07	249.13	-133.40	115.72
	3.125	248.93	-142.52	106.41	249.76	-132.84	116.92
	3.325	249.37	-142.40	106.97	250.15	-132.68	117.48
14	2.825	246.82	-141.52	105.30	247.78	-131.98	115.81
	3.125	247.67	-141.32	106.35	248.49	-131.67	116.82
	3.325	248.12	-141.22	106.89	248.87	-131.51	117.37
15	2.825	259.60	-122.14	137.46	261.51	-111.86	149.65
	3.125	260.27	-121.50	138.77	262.05	-110.94	151.12
	3.325	260.46	-121.03	139.44	262.21	-110.41	151.80
16	2.825	255.88	-118.03	137.85	257.54	-107.58	149.97
	3.125	256.29	-117.11	139.18	257.81	-106.40	151.41
	3.325	256.46	-116.64	139.82	257.94	-105.87	152.07

Table 4. Computed chemical shift anisotropy data for model compounds using stated functionals using the 6-311++g(d,p) basis set.

		Model Structure															
Functional	Interaction Distance / Å	**1**	**2**	**3**	**4**	**5**	**6**	**7**	**8**	**9**	**10**	**11**	**12**	**13**	**14**	**15**	**16**
MP2	2.825	20.51	21.96	56.39	52.81	57.86	58.37	66.15	26.53	30.15	71.51	32.76	39.40	106.49	112.12	73.95	73.19
	2.925	19.52	20.89	56.16	52.09	57.59	57.47	65.39	26.66	30.64	69.80	31.05	38.50	106.38	111.23	72.92	72.12
	3.025	18.67	19.96	55.92	51.44	57.31	56.64	64.71	26.76	31.07	68.32	29.59	37.69	106.23	110.42	71.99	71.18
	3.125	17.95	19.16	55.68	50.88	57.03	55.90	64.12	26.85	31.43	67.05	28.35	36.97	106.05	109.68	71.16	70.35
	3.225	17.36	18.49	55.46	50.39	56.76	55.23	63.61	26.91	31.75	65.97	27.30	36.35	105.86	109.04	70.44	69.64
	3.325	16.87	17.93	55.25	49.98	56.51	54.65	63.18	26.97	32.01	65.06	26.42	35.82	105.69	108.47	69.80	69.02
B3LYP	2.825	22.00	23.54	60.60	54.81	61.56	59.72	66.54	27.83	32.16	74.61	40.34	51.75	112.30	118.57	77.55	76.81
	2.925	21.03	22.45	60.48	54.16	61.48	58.89	65.85	27.99	32.48	72.59	38.48	51.12	112.32	117.67	76.60	75.80
	3.025	20.16	21.50	60.32	53.56	61.35	58.16	65.21	28.13	32.75	70.85	36.89	50.52	112.24	116.85	75.73	74.90
	3.125	19.43	20.68	60.14	53.02	61.20	57.52	64.65	28.24	32.97	69.37	35.53	49.98	112.12	116.10	74.96	74.10
	3.225	18.81	19.98	59.96	52.55	61.03	56.96	64.16	28.32	33.16	68.13	34.39	49.49	111.98	115.44	74.27	73.40
	3.325	18.30	19.40	59.79	52.14	60.87	56.46	63.74	28.40	33.32	67.09	33.44	49.06	111.84	114.85	73.66	72.79
LC-*ω*PBE	2.825	18.32	19.89	56.12	50.89	57.72	56.71	61.96	31.25	34.34	67.89	31.81	43.04	109.89	115.91	73.48	72.67
	2.925	17.38	18.83	55.92	50.06	57.46	55.69	61.26	31.48	34.66	66.21	30.16	42.20	109.85	115.01	72.38	71.54
	3.025	16.57	17.92	55.70	49.35	57.18	54.77	60.63	31.66	34.93	64.76	28.76	41.43	109.74	114.18	71.39	70.55
	3.125	15.89	17.14	55.47	48.72	56.90	53.94	60.08	31.79	35.14	63.53	27.58	40.76	109.59	113.43	70.53	69.68
	3.225	15.33	16.49	55.25	48.19	56.63	53.21	59.60	31.89	35.32	62.48	26.58	40.17	109.43	112.77	69.77	68.93
	3.325	14.87	15.95	55.06	47.76	56.37	52.57	59.21	31.97	35.47	61.62	25.75	39.65	109.28	112.20	69.11	68.29
LC-*ω*PBE-D3	2.825	18.32	19.89	56.12	50.89	57.72	56.71	61.96	31.25	34.34	67.89	31.81	43.04	109.89	115.91	73.48	72.67
	2.925	17.38	18.83	55.92	50.06	57.46	55.69	61.26	31.48	34.66	66.21	30.16	42.20	109.85	115.01	72.38	71.54
	3.025	16.57	17.92	55.70	49.35	57.18	54.77	60.63	31.66	34.93	64.76	28.76	41.43	109.74	114.18	71.39	70.55
	3.125	15.89	17.14	55.47	48.72	56.90	53.94	60.08	31.79	35.14	63.53	27.58	40.76	109.59	113.43	70.53	69.68
	3.225	15.33	16.49	55.25	48.19	56.63	53.21	59.60	31.89	35.32	62.48	26.58	40.17	109.43	112.77	69.77	68.93
	3.325	14.87	15.95	55.06	47.76	56.37	52.57	59.21	31.97	35.47	61.62	25.75	39.65	109.28	112.20	69.11	68.29
CAM-B3LYP	2.825	21.15	22.73	59.44	53.84	60.23	58.74	65.75	28.66	32.13	73.63	37.61	47.52	112.33	118.67	77.01	76.22
	2.925	20.13	21.60	59.25	53.13	60.08	57.86	65.02	28.84	32.45	71.62	35.70	46.68	112.30	117.73	75.93	75.10
	3.025	19.24	20.60	59.03	52.48	59.90	57.08	64.34	28.98	32.72	69.88	34.05	45.92	112.18	116.86	74.96	74.09
	3.125	18.48	19.75	58.81	51.90	59.70	56.39	63.74	29.09	32.94	68.41	32.66	45.23	112.02	116.08	74.09	73.21
	3.225	17.84	19.03	58.60	51.39	59.50	55.78	63.22	29.18	33.13	67.16	31.48	44.62	111.85	115.38	73.32	72.45
	3.325	17.31	18.42	58.40	50.96	59.31	55.25	62.79	29.25	33.30	66.12	30.50	44.09	111.69	114.77	72.64	71.78
BHandHLYP	2.825	20.14	21.65	56.79	51.09	57.91	55.98	62.78	25.33	29.25	69.93	37.32	46.54	105.24	111.02	73.12	72.35
	2.925	19.10	20.50	56.51	50.34	57.64	55.06	62.00	25.49	29.55	67.98	35.25	45.67	105.10	110.06	72.05	71.23
	3.025	18.19	19.50	56.23	49.67	57.37	54.25	61.30	25.61	29.82	66.32	33.49	44.88	104.91	109.18	71.09	70.25
	3.125	17.43	18.65	55.97	49.09	57.09	53.54	60.70	25.71	30.04	64.91	32.02	44.18	104.70	108.40	70.24	69.40
	3.225	16.80	17.94	55.72	48.59	56.84	52.91	60.18	25.79	30.23	63.72	30.78	43.57	104.49	107.71	69.49	68.66
	3.325	16.29	17.35	55.50	48.17	56.60	52.36	59.75	25.85	30.39	62.74	29.76	43.04	104.30	107.12	68.85	68.02

A change in the chemical shift as a function of the interaction angle was also observed. The change in angle yielded only small changes, on the order of less than 2 ppm between 140° and 180°. Overall, as the angle gets closer to 180°, the chemical shift decreases. The largest magnitude of change occurs between 140° and 160°, which could be explained by the gradual approach of Y to the methyl hydrogens, introducing a C-H···Y hydrogen bond, and begins to slow down as the angle approaches 180° as the tetrel bond becomes dominant. It is clear then that the tetrel bond distance remains the dominant effect on the carbon chemical shift and consequently, any effect of the angle on the chemical shift is expected to be negligible or overshadowed by other effects.

In additional to chemical shifts and energy, *J*-couplings are valuable parameters for the characterization of noncovalent interactions. Trans-hydrogen bond *J*-coupling has been studied extensively as an important tool for obtaining direct experimental evidence of hydrogen bonding via NMR.[138,139,140,141,142,143,144] Recently, computed *J*-coupling constants have been reported for a series of noncovalent interactions, including pnicogen bonding, chalcogen bonding and halogen bonding.[145,146,43] For instance, in a recent study by Del Bene et al., the interaction distance in a P-P pnicogen bond is estimated by the calculated correlation between the *J*-coupling and the interaction distance.[146] As such, *J*-coupling could provide a valuable probe of tetrel bonds.

In the present study, *J*-coupling was calculated for each of the model compounds (**Figure 14**) using the LC-ωPBE-D3, BHandHLYP, and CAM-B3LYP functionals. Total $^{1c}J(^{13}\mathrm{C},^{17}\mathrm{O}/^{15}\mathrm{N})$ coupling constants across the carbon tetrel bond are plotted in **Figure 18** as a function of the interaction distance in order to gain information as to whether the *J*-coupling can provide evidence for the presence of the carbon tetrel bond. Here, we propose use of the "${}^{1c}J$" nomenclature to denote trans-carbon bond coupling, in analogy with the "${}^{1h}J$, ${}^{2h}J$" etc. labels used in the literature for trans-hydrogen bond couplings. In each case, the roles of the Fermi contact (FC), spin-dipolar (SD), paramagnetic spin-orbital (PSO), and diamagnetic spin-orbital (DSO) mechanisms were assessed to evaluate their contributions to the total *J*-coupling (**Table 6** to **Table 8**, Appendix I – Supplementary Data). In all of the model structures, the FC mechanism contributes 100% ± 5% of the total, suggesting an overlap of orbitals with spin density centered at the nuclei of the carbon and the oxygen or nitrogen atoms. The importance of various coupling mechanisms in different models suggests a delicate interplay between these mechanisms[147] depending on the exact geometrical details and charge state of the model.

It can be observed in all cases that the coupling value (${}^{1c}J({}^{13}C,{}^{17}O)$ or ${}^{1c}J({}^{13}C,{}^{15}N)$) becomes more negative as the interaction distance becomes shorter. Clearly there exists a correlation between interaction distance and the magnitude of ${}^{1c}J$, thereby providing a new parameter for the study of carbon tetrel bonds. In each case, a second-order polynomial fits the data with a correlation coefficient, R^2, of at least 0.99 (**Table 9**-**Table 11**, Appendix I). The data corroborate the findings for pnicogen and halogen bonding as well, where analogous correlations have also been observed computationally. In one case of pnicogen bonding, $J({}^{31}P,{}^{31}P)$ decreases from hundreds of hertz toward zero as the interaction distance is increased. [146] In the case of *J*-coupling across Cl···N halogen bonds, computations show that the $J({}^{35/37}Cl,{}^{15}N)$ value approaches 0 Hz from values of between approximately -60 and -90 Hz, as the interaction distance is increased. [70]

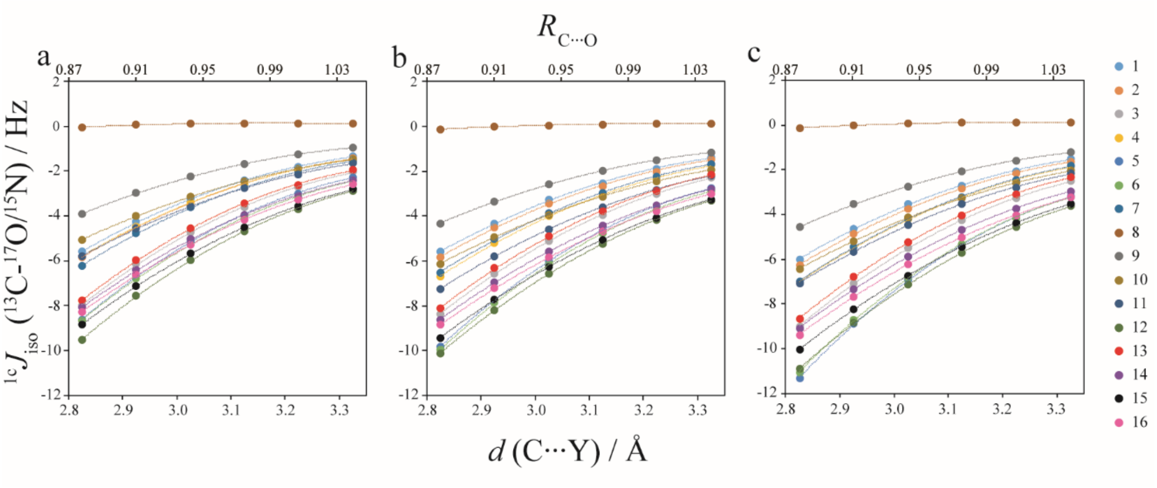

Figure 18. Computed *J*-coupling for model compounds. Graphs represent ^{1c}J-coupling values between ^{13}C and either ^{17}O or ^{15}N using (a) The LC-ωPBE-D3, (b) BHandHLYP, and (c) CAM-B3LYP methods. In each case, the 6-311++G(d,p) basis set is used. Each plot is fit by a quadratic polynomial function with $R^2 > 0.99$ (**Table 9** to **Table 11** in Appendix I – Supplementary Data).

3.2 Experimental NMR Investigations of Noncovalent Tetrel Bonds

The calculations on isolated model systems provide valuable insight into the relationship between NMR parameters and tetrel bonds. Given that the crystal lattice can influence NMR parameters, a further step was taken in order to investigate dependence of carbon chemical shift on the carbon tetrel bond in the case of crystal structures. The CSD was used to search for published crystal structures that contain carbon tetrel bonds. Because there is not yet a universally accepted definition of a tetrel bond, candidate compounds were screened for using two criteria, which are in accordance with the IUPAC standard for halogen bonds: (1) The C···Y interaction distance must be within the sum of their van der Waals radii and (2) R-C···Y angle must be within 160° and 180°.[148] We note that these criteria are slightly stricter than those used in the work of Thomas and co-workers, wherein the angle range used is 140° to 180°.[58] Among a large number of hits were sarcosinium tartrate ($d_{C...O}$ = 3.08 Å) (**Figure 6**), sarcosine maleate ($d_{C...O}$ = 2.96 Å), and N,N,N’,N’-tetramethylethylenediammonium succinate succinic acid ($d_{C...O}$ = 3.07 Å) (**Figure 19**) which were found to be good carbon tetrel-bonding candidates for this study.[44,149] Each salt is compared to its corresponding salt lacking a tetrel bond.

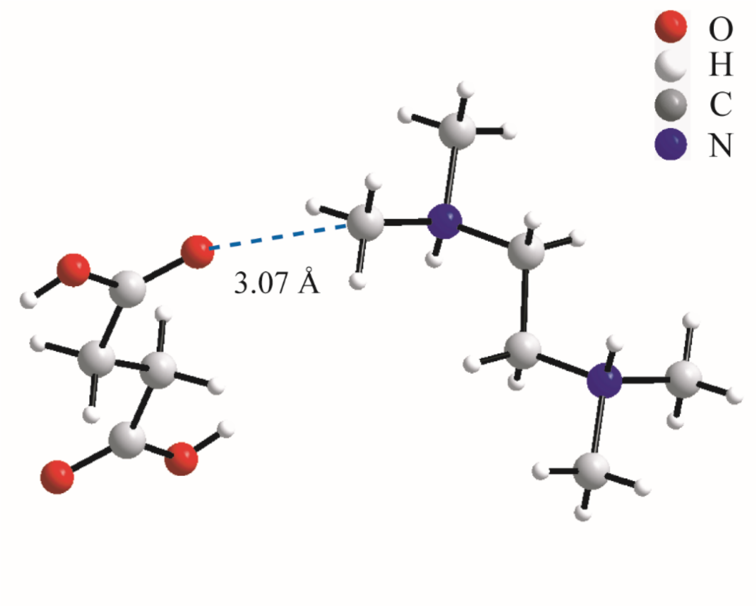

Figure 19. The tetrel bond present in N,N,N’,N’-tetramethylethylenediammonium succinate succinic acid. The interaction distance is 3.07 Å.

Although the tetrel bonds in these compounds are significant on the basis of the C···O distances, there was concern with respect to the possible impact of competing weak C-H···O hydrogen bonds. In the case of sarcosinium tartrate, the distances between O and H are greater than 2.72 Å, the sum of their vdW radii. In sarcosinium maleate, there is a single hydrogen 2.70 Å from the oxygen, according to the published crystal structure. Thus, for these two salts, the strengths of the tetrel bonds, as judged by the reduced distance parameter ($R_{X\cdots Y}$; eqn. **36**) are significant whereas the strength of hydrogen bonds as quantified by the same criteria is far less important. Generally, the methyl protons are splayed with respect to the oxygen. The possible role of trifurcated hydrogen bonds in such systems has been discussed in ref 58. In the case of N,N,N’,N’-tetramethylethylenediammonium succinate succinic acid, there are not competing hydrogen bonds directly with the tetrel bonded oxygen atom, however, the methyl hydrogens still make close contacts with other oxygen atoms in the system. Regardless of the possible weak influence of a weak trifurcated hydrogen bond, the presence of a tetrel bond means that *de facto* this interaction contributes to the observed chemical shift.

The compounds were first made according to the literature sources (See section 2.4.1). PXRD was used to confirm the identities of the substances. The PXRD show good agreement between the obtained compounds and the simulated source. In the case of sarcosine, there is only an extra peak at about 26^{o}, but one peak missing at about 33^{o} on the 2θ axis (**Figure 20**), while sarcosinium tartrate shows almost perfect agreement with the simulated diffraction patters, albeit with stronger signal intensities (**Figure 21**). The N,N,N’,N’-tetramethylethylenediammonium salts are shown to have good agreement with their simulated diffraction patterns (**Figure 22** and **Figure 23**).

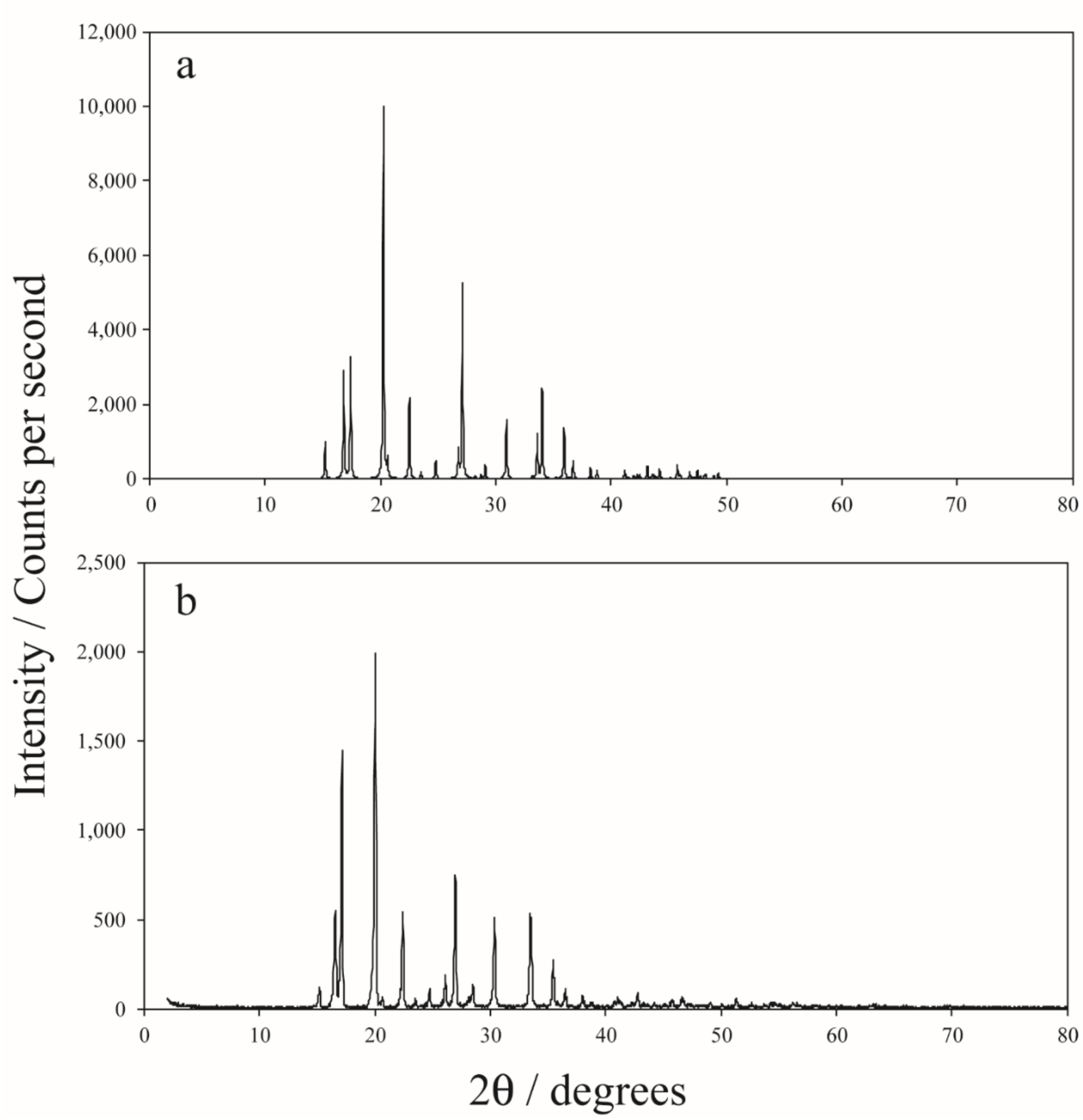

Figure 20. Powder X-Ray diffractogram of sarcosine. The simulated diffractogram (a) was obtained using the Mercury version 3.5.1 software provided by the CCDC. The experimental diffractogram (b) was obtained from a powdered sample using a Rigaku Ultima IV X-ray diffractometer.

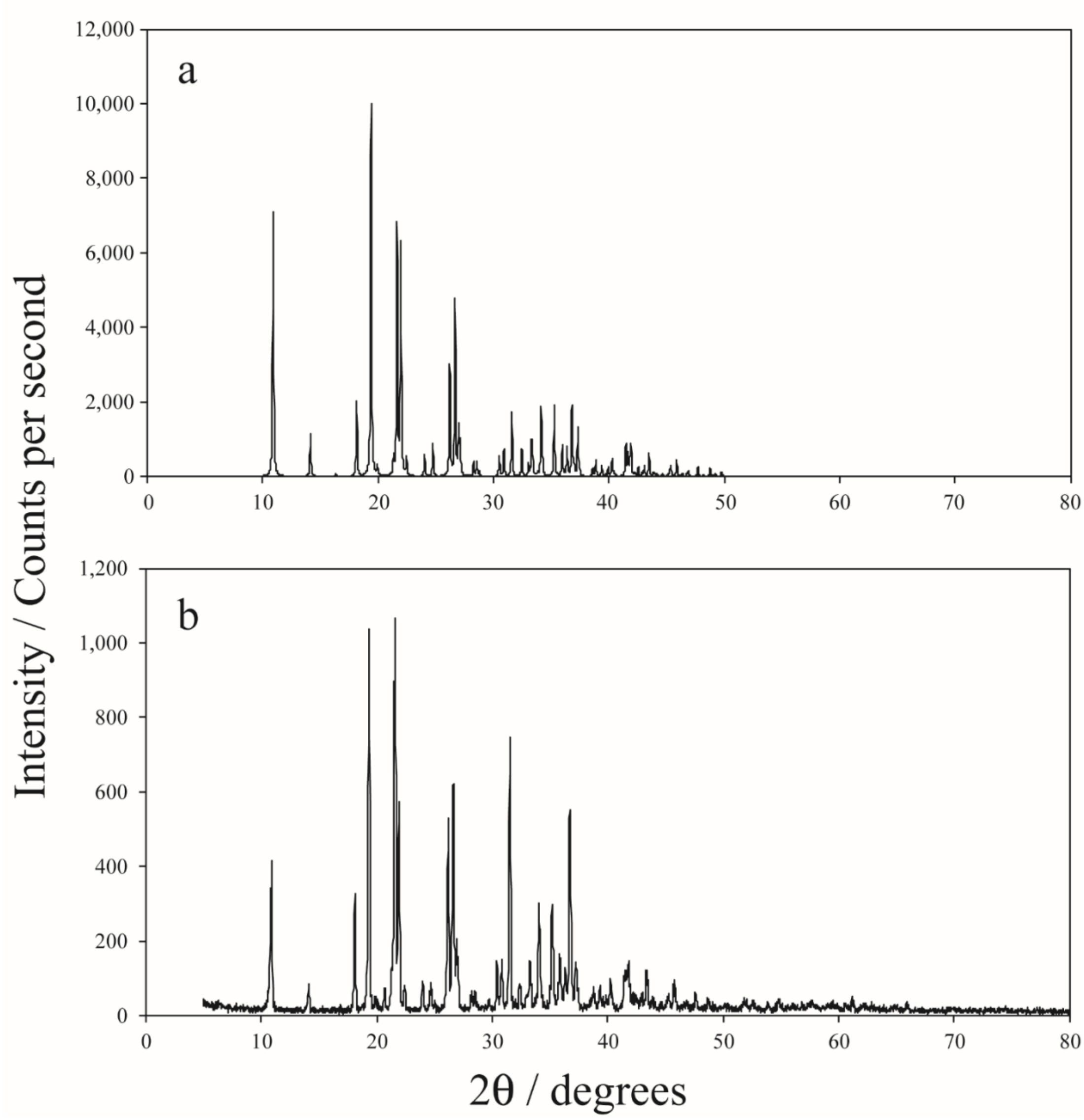

Figure 21. Powder X-Ray diffractogram of sarcosinium tartrate. The simulated diffractogram (a) was obtained using the Mercury version 3.5.1 software provided by the CCDC. The experimental diffractogram (b) was obtained from a powdered sample using a Rigaku Ultima IV X-ray diffractometer.

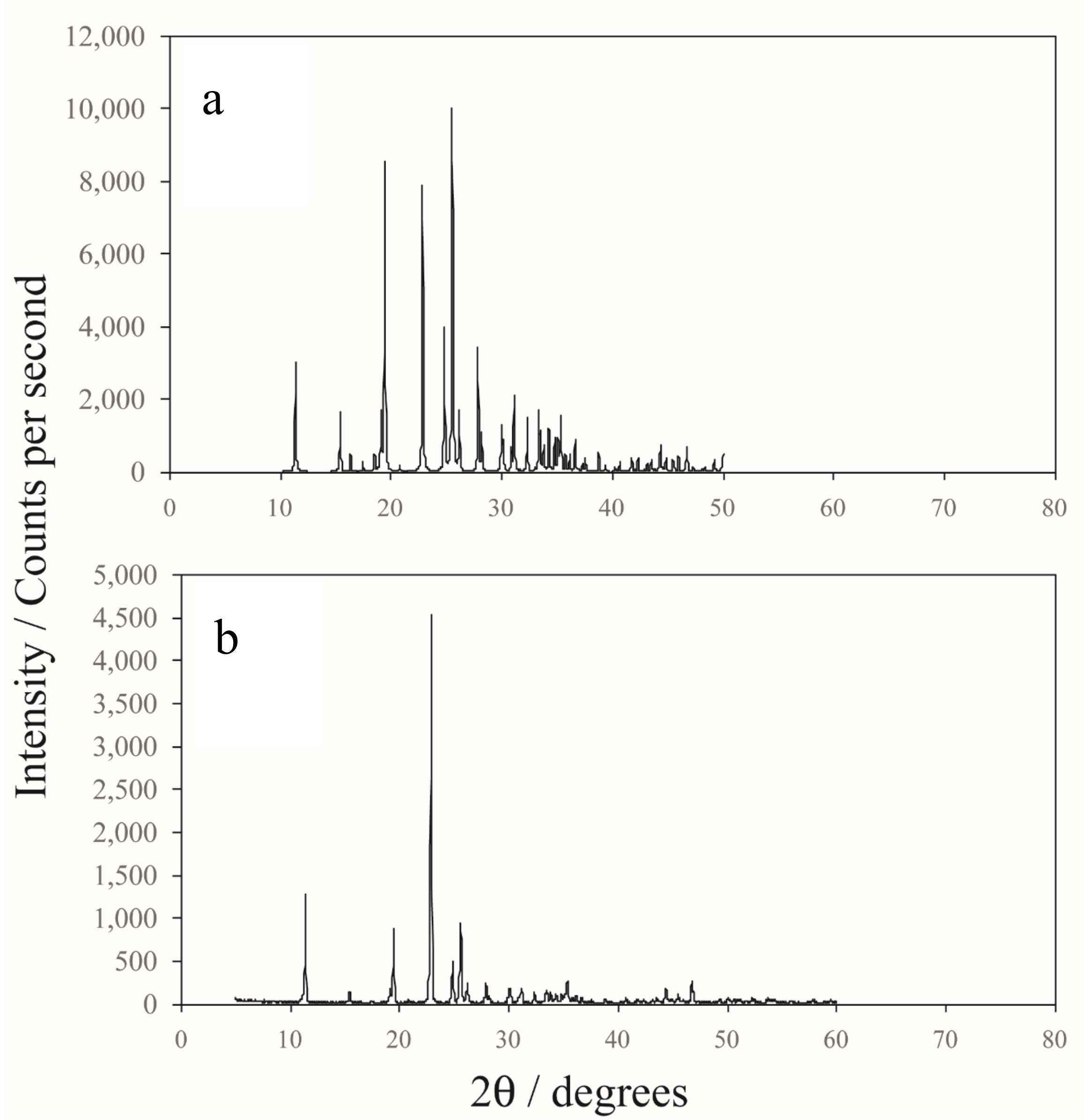

Figure 22. Powder X-Ray diffractogram of N,N,N',N'-tetramethylethylenediammonium dichloride. The simulated diffractogram (a) was obtained using the Mercury version 3.5.1 software provided by the CCDC. The experimental diffractogram (b) was obtained from a powdered sample using a Rigaku Ultima IV X-ray diffractometer.

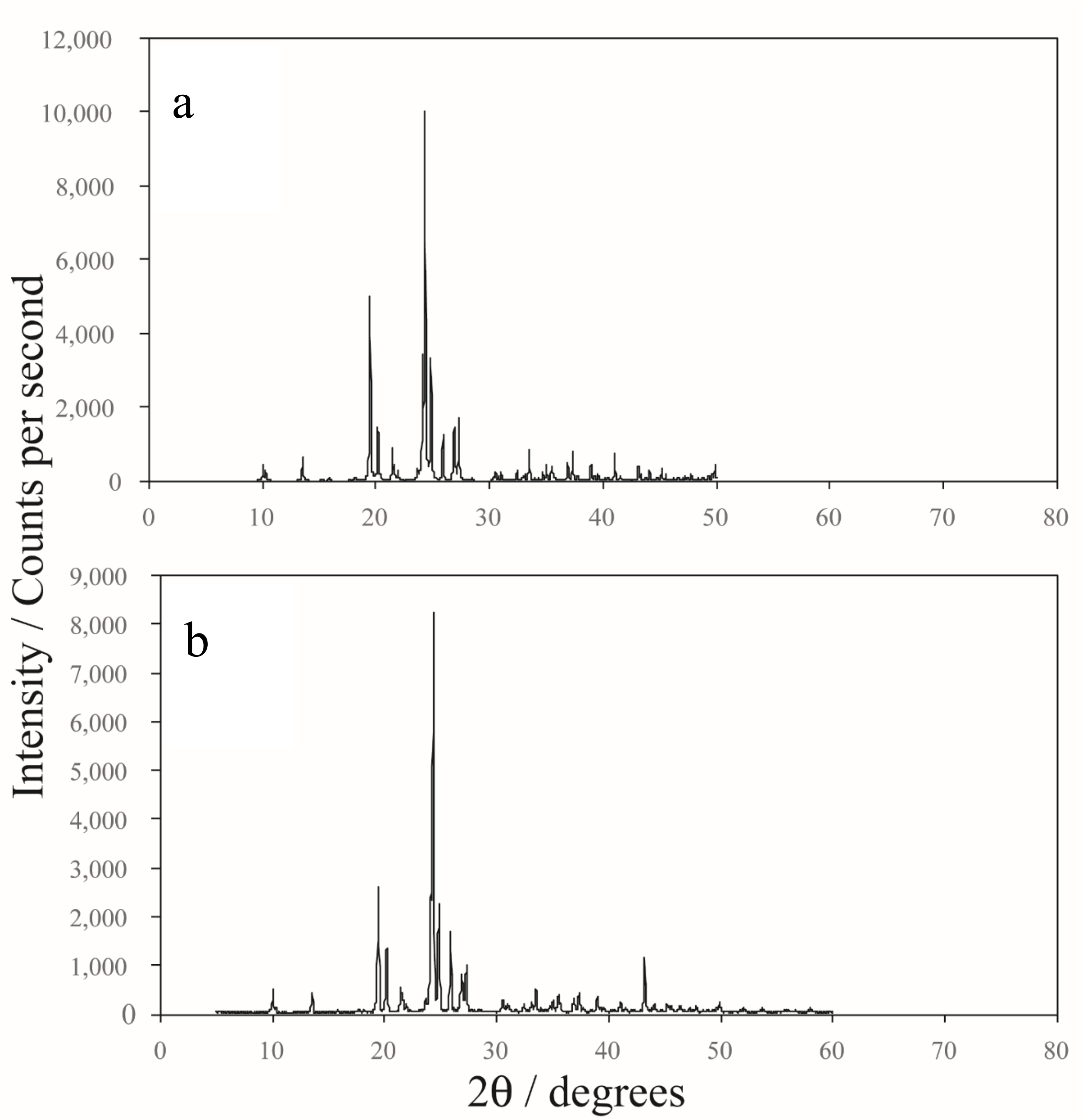

Figure 23. Powder X-Ray diffractogram of N,N,N’,N’-tetramethylethylenediammonium succinate succinic acid. The simulated diffractogram (a) was obtained using the Mercury version 3.5.1 software provided by the CCDC. The experimental diffractogram (b) was obtained from a powdered sample using a Rigaku Ultima IV X-ray diffractometer.

The GIPAW DFT computed and experimental ^{13}C solid state NMR chemical shifts corresponding the sarcosine and N,N,N’,N’-tetramethylethylenediammonium methyl groups

(**Figure 24** to **Figure 27**) involved in the both in the presence of a carbon tetrel bond and in the absence are reported in **Table 5**. In the same table, the C···O noncovalent bond distances, as well as the N-C covalent bond distances are obtained from the CSD.

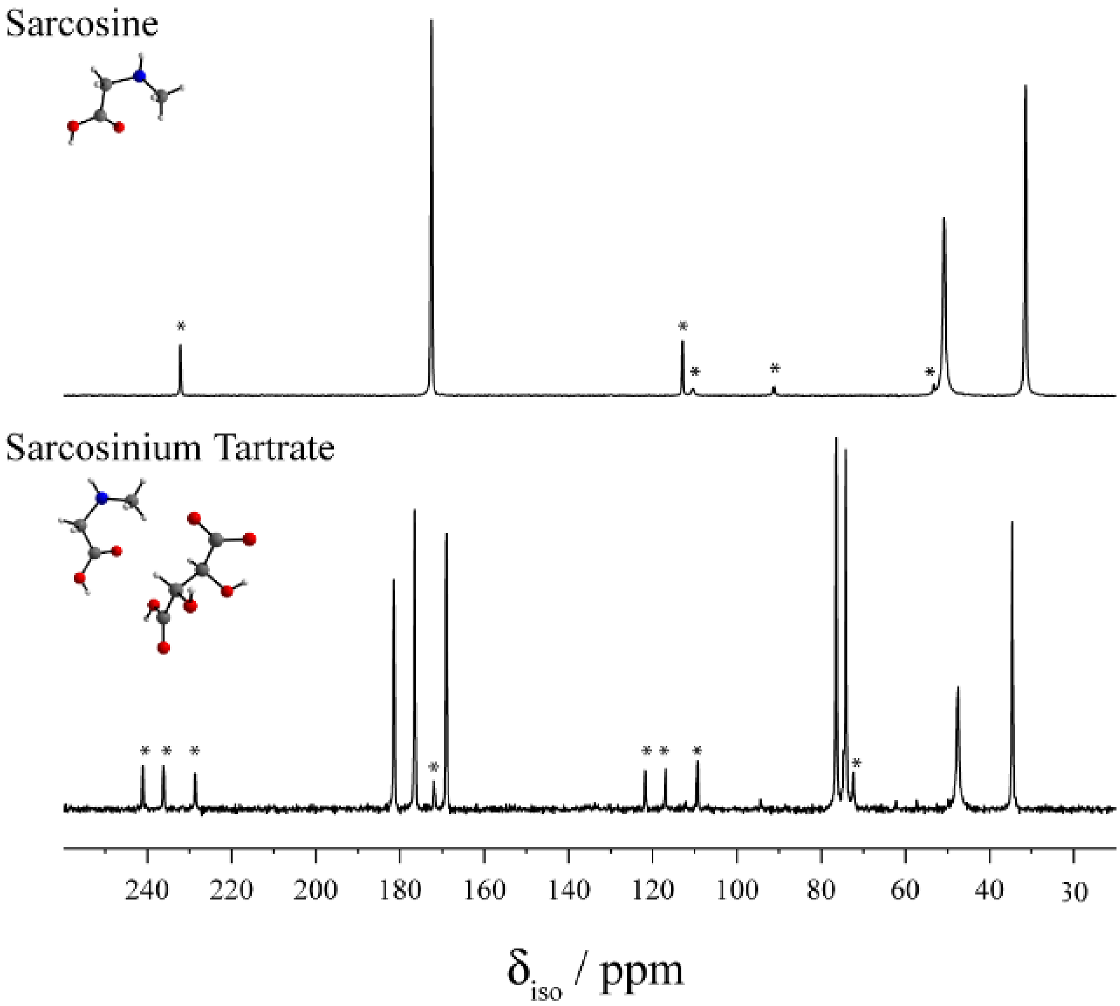

Figure 24. ^{13}C CP/MAS spectra of sarcosine (top) and sarcosinium tartrate (bottom). Spinning sidebands are denoted with asterisks. B_0 = 9.4 T.

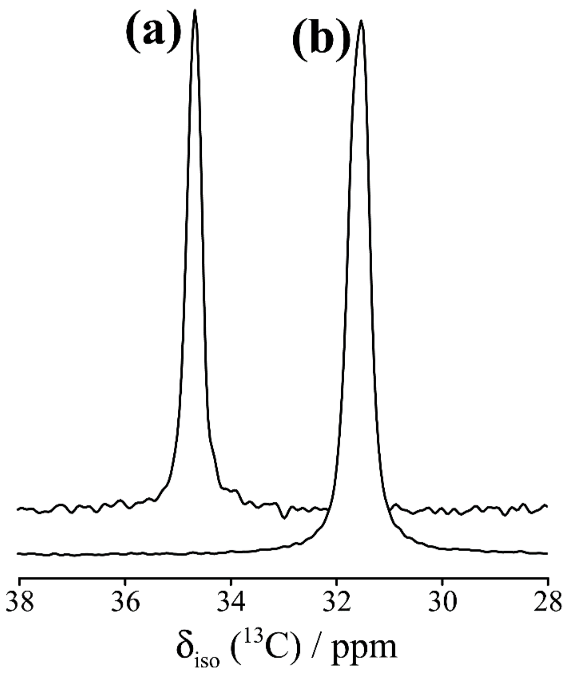

Figure 25. Selected regions of experimental ^{13}C cross-polarization magic-angle spinning (CP/MAS) NMR spectra of the methyl carbon associated with a tetrel bond. B_0 = 9.4 T. (a) Sarcosinium Tartrate. (b) Sarcosine.

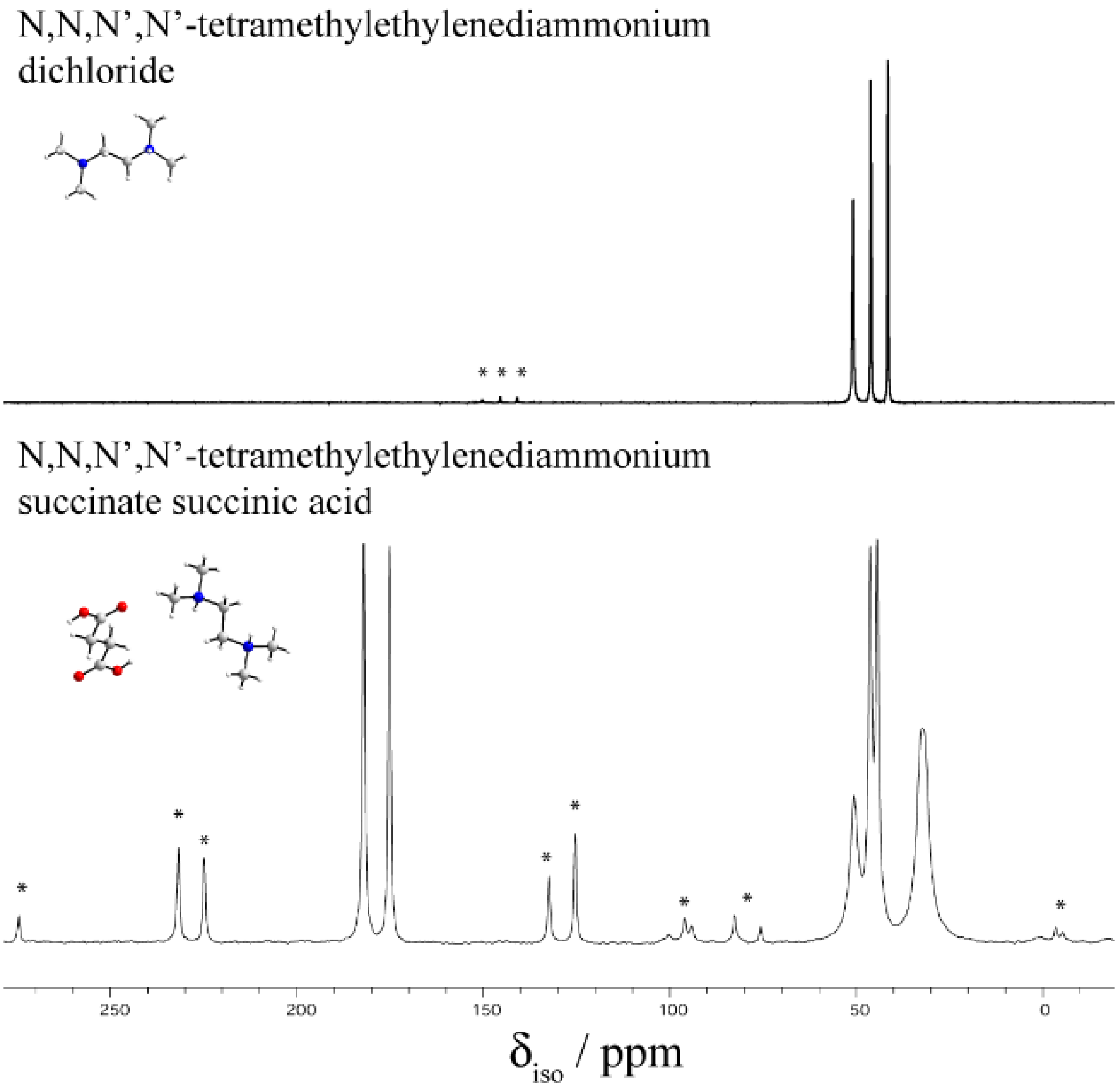

Figure 26. ^{13}C CP/MAS spectra of N,N,N',N'-tetramethylethylenediammonium dichloride (top) and N,N,N',N'-tetramethylethylenediammonium succinate succinic acid (bottom). Spinning sidebands are denoted with asterisks. B_0 = 9.4 T.

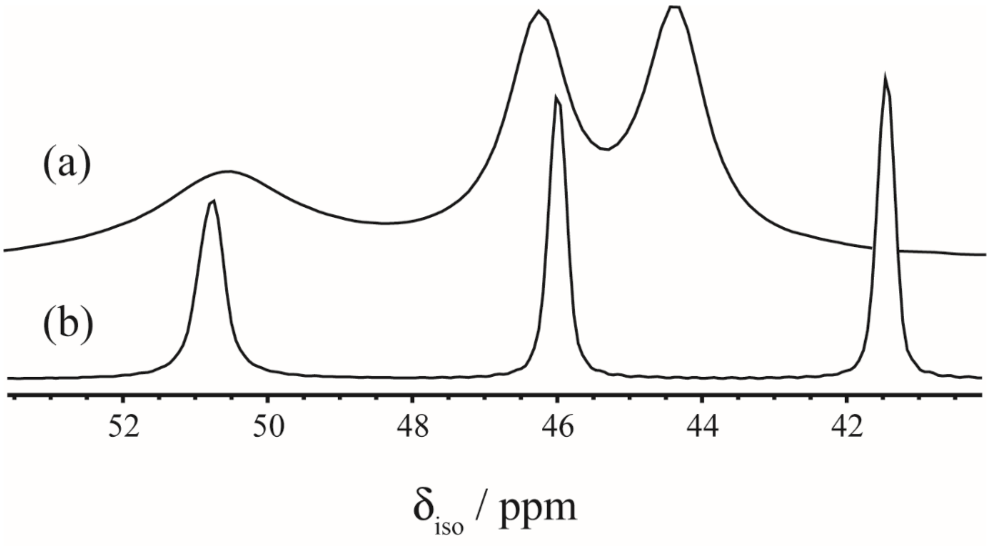

Figure 27. Selected regions of experimental ^{13}C cross-polarization magic-angle spinning (CP/MAS) NMR spectra of the methyl carbon associated with a tetrel bond. B_0 = 9.4 T. (a) N,N,N',N'-tetramethylethylenediammonium dichloride. (b) N,N,N',N'-tetramethylethylenediammonium succinate succinic acid.

Table 5. Calculated GIPAW and experimental ^{13}C isotropic chemical shifts for the methyl carbon on sarcosine compounds.

compound	N-C Bond Length / Å	Interaction Distance (C···O) / Å	$R_{C\cdots O}$	$\delta_{iso}(^{13}C)$ calc. / ppm	Ω calc. /ppm	κ calc.	$\delta_{iso}(^{13}C)$ exp. / ppm
Sarcosine	1.4813(3)	n/a	n/a	37.9	56.8	0.773	31.5
Sarcosinium Tartrate	1.485(3)	3.08	0.96	43.6	61.8	0.604	34.7
Sarcosinium Maleate [149]	1.497(2)	2.96	0.92	47.9	55.0	0.753	36
TMEDA[a] HCl	**1.487(4)**	**n/a**	**n/a**	**27.8**	**72.1**	**0.879**	**41.4**
	1.486(4)	n/a	n/a	32.0	86.8	0.635	46.0
TMEDA[a] succinate	**1.493(2)**	**3.07**	**0.95**	**33.4**	**89.6**	**0.646**	**44.3**
	1.487(2)	3.26	1.01	31.4	73.3	0.898	46.2

(a) *TMEDA refers to N,N,N',N'-tetramethylethylenediammonium.*

(b) *Entries in bold correspond to the methyl carbons of interest. In TMEDA succinate, the bolded entry participates in the σ-hole interaction, whereas the other methyl carbon does not.*

It is interesting to note that in each of the cases where the carbon tetrel bond is present, the introduction of this interaction causes the chemical shift of the methyl group to increase. In addition, the N-C bond lengthens in the presence of the tetrel bond. These trends are reflected in both the GIPAW calculations and the experimental results where the chemical shift increases are on the order of 5 to 10 ppm and 3 to 5 ppm, respectively. The magnitudes of the increases noted from solid-state NMR spectroscopy experiments mirror much more closely the increases calculated for isolated model systems.

The trends predicted by the GIPAW calculations are nevertheless also consistent with the experimental data. Note that a comparison of the experimental and calculated absolute values of the chemical shifts, while perhaps providing some insight into the overall accuracy of the computational method and absolute shielding scale used, does not detract from the findings as far as the *trend* in the values as a function of the tetrel bond distance.

We note that in the cases of the sarcosine salts, the amine becomes protonated, whereas sarcosine itself is neutral. We assessed the potential competing effect of this protonation on the methylamine ^{13}C chemical shift and found there to be a slight difference between the neutral and charged molecules. In a literature review, it was noted that the effect of protonation of sarcosine causes a *decrease* in the methylamine ^{13}C chemical shift by 1.83 ppm, from 35.75 ppm to 33.92 ppm (in solution where the carboxylate is negatively charged).[150] This trend was confirmed by Batchelor and co-workers, who noted that the ^{13}C protonation shift of a methylamine is -2.04 ppm[151], while Thursfield and coworkers distinguish a chemical shift difference of about -2.7 ppm between monomethylamine ($\delta =$ 26.9 to 27.5 ppm) and the corresponding cation ($\delta =$ 24.3 to 24.8 ppm) during a conversion of methanol and ammonia over the zeolite H-SAPO-34.[152] Thursfield's results are also confirmed by Jiang *et al.*[153] Given these experimental results reported in the literature, protonation of the amine in sarcosine would therefore be expected to produce a small negative change in the chemical shift, on the order of 2 to 3 ppm. However, our experimental and computational data present a change in chemical shift in the *opposite* direction upon the combined introduction of a tetrel bond and amine protonation. Therefore, this strongly suggests that the dominant cause for this change is the introduction of the carbon tetrel bond.

Chapter 4 - Conclusions

This combined computational and experimental work has provided several outcomes and insights into the nature of tetrel bonding. First, the quantum chemical calculations on isolated model systems show that the chemical shifts of carbon atoms acting as tetrel bond donors increase with the strength of the interaction. Both diamagnetic and paramagnetic contributions to the magnetic shielding constant are responsible for this trend. Furthermore, ^{13}C chemical shift anisotropies increase with the strength of the interaction.

In agreement with the computations on isolated models, calculations using periodic boundary conditions to model the effects of an infinite crystal lattice (GIPAW DFT) show that the chemical shifts of carbon atoms acting as tetrel bond donors increase relative to parent compounds where tetrel bonds are absent. Experimental data for sarcosine, where no tetrel bond is present, and for two sarcosine salts exhibiting tetrel bonds in the solid state confirm the computational trends described by both the cluster model analysis as well as the GIPAW DFT calculations on published crystal structures.

Cluster model calculations of trans-tetrel bond J couplings show that the magnitude of $^{1c}J(^{13}\mathrm{C},^{17}\mathrm{O})$ increases from zero to several hertz as the C···O interaction distance is decreased to less than the sum of their van der Waals radii. The couplings are typically, but not always, entirely due to the Fermi-contact coupling mechanism.

In summary, the present work provides compelling computational and experimental evidence that the carbon tetrel bond has an influence on NMR parameters in the solid state, thus creating opportunities to use NMR crystallography to characterize tetrel-bonded supramolecular architectures and functional materials.

There is still work to be done in completing the characterization of the carbon tetrel bond. Concurrently, there is an opportunity for further study of other tetrel elements in order to understand the nature of the electronic structures of these bonds. Further research involving silicon, germanium, tin, and lead would be useful using both SSNMR methods and *ab initio* computational studies using our state-of-the-art equipment at the National Ultrahigh-Field NMR Facility for Solids. The crystal structures will first be solved by X-ray diffraction, and the study of these nuclides by multinuclear SSNMR will provide key data relevant to this project. The chemical shift response as a result of the formation of the tetrel bond, as well as other NMR parameters, will assist in developing a clear picture of the tetrel bond. Quantum calculations using density functional theory at the Canadian High Performance Computing Virtual Laboratory will be used to complement the experimental data and confirm any observations.

References

[1] Dalton, J. III. On the absorption of gases by water and other liquids. *Phil. Mag. Ser. 1.* **1806**(24), 15-24.

[2] Dalton, J. *A New System of Chemical Philosophy*, R. Bickerstaff, Strand, London, 1808.

[3] Aad, G.; Abajyan, T. Abbott, B. Abdallah, *et al.* Observation of a new particle in the search for the Standard Model Higgs boson with the ATLAS detector at the LHC. *Phys. Lett. B* **2012**, *716*, 1-29.

[4] Chatrchyan, S.; Khachatryan, V.; *et al.* Observation of a new boson at a mass of 125 GeV with the CMS experiment at the LHC. *Phys. Lett. B*, **2012**, *716*, 30-61.

[5] Petrucci, R. H.; Harwood, W. S.; Herring, F. G.; Madura, J. D. General Chemistry: Principles and Modern Applicationa, 9th ed.; Pearson Prentice Hall: Upper Saddle River, 2007.

[6] Pauli, W. Exclusion principle and quantum mechanics. Nobel Lecture, 1946.

[7] Atkins, P.; De Paula, J. Physical Chemistry, 3rd ed.; W. H. Freeman and Company: New York, 2006.

[8] Hund, F. Atomtheoretische Deutung des Magnetismus der seltenen. Erden. *Z. Phys. A-Hadron Nucl.* **1925**, *33*, 855-859.

[9] Kutzelnigg, W.; Morgan III, J. D. Hund's rules. *Z. Phys. D Atom Mol Cl.* **1996**, *36*, 197-214.

[10] Levitt, M. H. *Spin Dynamics: Basics of Nuclear Magnetic Resonance*, 2nd ed.; John Wiley & Sons Ltd.: West Sussex, 2008.

[11] Steiner, T. The Hydrogen Bond in the Solid State. *Angew. Chem. Int. Ed.* **2002**, *41*, 48-76.

[12] Arunan, E.; Desiraju, G. R.; Klein, R. A.; Sadlej, J.; Scheiner, S.; Alkorta, I.; Clary, D. C.; Crabtree, R. H.; Dannenberg, J. J.; Hobza, P.; Kjaergaard, H. G.; Legon, A. C.; Mennucci, B.; Nesbitt, D. J. Definition of the hydrogen bond (IUPAC Recommendations 2011). *Pure Appl. Chem.* **2011**, *83*, 1637-1641.

[13] Voet, D.; Voet, J. G. *Biochemistry,* 3rd ed.; John Wiley & Sons Ltd.: New York, 2004.

[14] Dougherty, D. A. Cation-π Interactions in Chemistry and Biology: A New View of Benzene, Phe, Tyr and Trp. *Science*, **1996**, *271*, 163-168.

[15] Sheiner, S. *Noncovalent Forces*; Springer International Publishing Switzerland, 2015.

[16] Murrey, J. S.; Lane, P.; Politzer, P. A Predicted New Type of Directional Noncovalent Interaction. *Int. J. Quantum Chem.* **2007,** *107,* 2286-2292.

[17] Del Bene, J. E.; Alkorta, I.; Elguero, J. Properties of Cationic Pnicogen-Bonded Complexes $F_{4-n}H_nP^+$:N-Base with F-P···N Linear and $n = 0$-3. *J. Phys. Chem. A* **2015**, *119*, 5853-5864.

[18] Kapecki, J. A.; Baldwin, J. E. Cycloaddition chemistry. XXI. Extended Hueckel calculations on two heterocyclic systems containing 2.41-Å and 2.64-Å. sulfur-oxygen distances. *J. Am. Chem. Soc.* **1969,** *91* (5), 1120-1123.

[19] Murray, J. S.; Lane, P.; Clark, T.; Politzer, P. σ-hole bonding: molecules containing group VI atoms. *J. Molec Model.* **2007,** *13* (10), 1033-1038.

[20] Ramasubbu, N.; Parthasarathy, R. Stereochemistry of Incipient Electrophilic and Nucleophilic Reactions at Divalent Selenium Center: Electrophilic-Nucleophilic Pairing and Anisotropic Shape of Se in Se···Se Interactions. *Phosphorus Sulfur* **1987,** *31,* 221-229.

[21] Nziko, V. d. P. N.; Scheiner, S. Chalcogen Bonding between Tetravalent SF_4 and Amines. *J. Phys. Chem. A* **2014**, *13*, 10849-10856.

[22] Bauzá, A.; Frontera, A. Aerogen Bonding Interaction: A New Supramolecular Force? *Angew. Chem. Int. Ed.* **2015,** *54*.

[23] Metrangolo, P.; Resnati, G. *Halogen Bonding: Fundamentals and Applications;* Springer Berlin Heidelberg: Berlin, 2008.

[24] Metrangolo, P.; Resnati, G. *Halogen Bonding I: Impact on Materials Chemistry and Life Sciences;* Springer International Publishing, 2015.

[25] Brinck, T.; Murray, J. S.; Politzer, P. Surface Electrostatic Potentials of Halogenated Methanes as Indicators of Directional Intermolecular Interactions. *Int. J. Quantum Chem.* **1992**, *19*, 57-64.

[26] Clark, T.; Hennemann, M.; Murray, J. S.; Politzer, P. Halogen bonding: the sigma-hole. Proceedings of "Modeling interactions in biomolecules II", Prague, September 5th-9th, 2005. *J. Mol. Model.* **2006**, *13*, 291-296

[27] Politzer, P.; Murray, J. S.; Clark, T. Halogen bonding and other σ-hole interactions: a perspective. *Phys. Chem. Chem. Phys.* **2013,** *15,* 11178-11189.

[28] Politzer, P.; Murray, J. S. ; Janjić, G. V.; Zarić, S D. *σ*-Hole Interactions of Covalently-Bonded Nitrogen, Phosphorus and Arsenic: A Survey of Crystal Structures. *Crystals*, **2014**, *4*, 12-31.

[29] Berg, J.M.; Tymocsko, J. L.; Stryer, L. *Biochemistry, 5th ed.*; W. H. Freeman and Company: New York, 2002.

[30] Scheiner, S. The Pnicogen Bond: Its Relation to Hydrogen, Halogen, and Other Noncovalent Bonds. *Accounts Chem. Res.* **2013**, *46*, 280-288.

[31] Politzer, P.; Lane, P.; Concha, M. C.; Ma, Y.; Murray, J. S. An overview of halogen bonding. *J. Molec. Model.* **2007**, *13*, 305-311.

[32] Lommerse, J. P. M.; Stone, A. J.; Taylor, R.; Allen, F. H. The Nature and Geometry of Intermolecular Interactions between Halogens and Oxygen or Nitrogen. *J. Am. Chem. Soc.* **1996**, *118*, 3108-3116.

[33] Wang, W.; Ji, B.; Zhang, Y. Chalcogen Bond: A Sister Noncovalent Bond to Halogen Bond. *J. Phys. Chem. A* **2009**, *113*, 8132-8135.

[34] Politzer, P.; Murray, J. S. The fundamental nature and role of the electrostatic potential in atoms and molecule. *Theor. Chem. Acc.* **2002**, *108*, 134-142.

[35] Clark, T.; Hennemann, M.; Murray, J. S.; Politzer, P. Halogen bonding: the σ-hole. *J. Mol. Model.* **2007**, *13*, 291-296.

[36] Murray, J. S.; Lane, P.; Politzer, P. Expansion of the σ-hole concept. *J. Molec. Model.* **2009,** *15* (6), 723-729.

[37] Murray, J. S. Factors affecting the strengths of σ-hole electrostatic potentials. *J. Comput. Sci.* **2014**, *5*, 590-596.

[38] Cavallo, G.; Metrangolo, P.; Pilati, T.; Resnati, G.; Terraneo, G. Naming Interactions from the Electrophilic Site. *Cryst. Growth Des.* **2014,** *14*, 2697-2702.

[39] Bauzà, A.; Mooibroek, T. J.; Frontera, A. Tetrel-Bonding Interaction: A Rediscovered Supramolecular Force? *Angew. Chem. Int. Edit.* **2013,** *52,* 12317-12321.

[40] Mani, D.; Arunan, E. The X-C$\cdots\pi$ (X = F, Cl, Br, CN) Carbon Bond. *J. Phys Chem. A* **2014,** *118,* 10081-10089.

[41] Li, Q.; Guo, X.; Yang, X.; Li, W.; Cheng, J.; Li, H.-B. A σ-hole interaction with radical species as electron donors: does single-electron tetrel bonding exist? *Phys. Chem. Chem. Phys.* **2014,** *16,* 11617-11625.

[42] Mani, D.; Arunan, E. The X-C···Y (X = O/F, Y = O/S/F/Cl/Br/N/P) 'carbon bond' and hydrophobic interactions. *Phys. Chem. Chem. Phys.* **2013,** *15,* 14377-14383.

[43] Del Bene, J. E. Influence of Substituent Effects on the Formation of P···Cl Pnicogen Bonds or Halogen Bonds. *J. Phys. Chem. A* **2014,** *118,* 2360-2366.

[44] Krishnakumar, R. V.; Subha Nandhini, M.; Natarajan, S. Sarcosinium tartrate. *Acta Crystallogr. C* **2001,** *C57,* 165-166.

[45] Brellère, C.; Carré, F.; Corriu, R. J. P.; Poirier, M.; Royo, G.; Zwecker, J. Hexacoordinated Silicon Species: A Possible Model for Reaction Intermediates. 1. X-ray Determination of the Geometry in the Solid State. *Organometallics* **1989**, *8*, 1831-1833.

[46] Belzner, J.; Schär, D.; Herbst-Irmer, R.; Kneisel, B. O.; Noltemeyer, M. Synthesis and Structure of Silicon Compounds Intramolecularly Coordinated by Hydrazino Groups. *Tetrahedron* **1998**, *54*, 8481-8500.

[47] Kost, D.; Gostevskii, B.; Kalikhman, I. Silicon rehybridization and molecular rearrangements in hypercoordinate silicon dichelates. *Pure Appl. Chem.* **2007**, *79* (6), 1125-1134.

[48] Carre, F.; Chuit, C.; Corriu, R. J. P.; Mehdi, A.; Reye, C. Synthesis, Structure and Fluxional Behaviour of a Dihydrosilane Bearing and Aryldiamine Pincer Ligand. *Organometallics* **1995**, *14*, 2754-2759.

[49] Berceanc, V.; Crainic, C.; Haiduc, I.; Mahon, M. F.; Molloy, K. C.; Venter, M. M.; Wilson, P. J. The structural chemistry of organotin derivatives of 5-mercapto-3-phenyl-1,3,4-

thiadiazoline-2-thione: supramolecular structures involving intermolecular Sn···S, N-H···S or S···S interactions. *J. Chem. Soc., Dalton Trans.* **2002**, 1036-1045.

[50] Akkari-El Ahdab, A.; Rima, G.; Gornitzka, H.; Barrau, J. Synthesis and characterization of 2,4,6-tris((dimethylamino)methyl)phenoxysilicon compounds. *J. Organomet. Chem.* **2001**, *636*, 96-107.

[51] Alkorta, I.; Rozas, I.; Elguero, J. Molecular Complexes between Silicon Derivatives and Electron-Rich Groups. *J. Phys. Chem. A* **2001,** *105* (4), 743-749.

[52] Mitzel, N. W.; Vojinović, K.; Frõhlich, R.; Foerster, T.; Robertson, H. E.; Borisenko, K. B.; Rankin, D. W. H. Three-Membered Ring or Open Chain Molecule − $(F_3C)F_2SiONMe_2$ a Model for the α-Effect in Silicon Chemistry. *J. Am. Chem. Soc.* **2005,** *127* (39), 13705-13713.

[53] Azofra, M. M.; Scheiner, S. Tetrel, chalcogen, and CH··O hydrogen bonds in complexes pairing carbonyl-containing molecules with 1, 2, and 3 molecules of CO_2. *J. Chem. Phys.* **2015,** *142,* 034307.

[54] Varadwaj, P. R.; Varadwaj, A.; Jun, B.-Y. Significant evidence of C···O and C···C long-range contacts in several heterodimeric complexes of CO with CH_3-X, should one refer to them as carbon and dicarbon bonds! *Phys. Chem. Chem. Phys.* **2014,** *16,* 17238-17252.

[55] Lu, Y.; Wang, Y.; Zhu, W. Nonbonding interactions of organic halogens in biological systems: implications for drug discovery and biomolecular design. *Phys. Chem. Chem. Phys.* **2010,** *12,* 4543-4551.

[56] Grabowski, S. J. Tetrel bond-σ-hole bond as a preliminary stage of the S_N2 reaction. *Phys. Chem. Chem. Phys.* **2014,** *16,* 1824-1834.

[57] Koch, U., Popelier, P.L.A. Characterization of C-H-O hydrogen bonds on the basis of the charge density. *J. Phys. Chem*. **1995**, *99*, 9747–9754.

[58] Thomas, S. P.; Pavan, M. S.; Guru Row, T. N. Experimental evidence for 'carbon bonding' in the solid state from charge density analysis. *Chem. Commun.* **2014,** *50,* 49-51.

[59] Duer, M. J. *Introduction to Solid State NMR Spectroscopy*, Blackwell Publishing Ltd: Oxford, 2004.

[60] Jameson, C. J. Reply to ‘conventions for tensor quantities used in nuclear magnetic resonance, nuclear quadrupole resonance and electron spin resonance spectroscopy. *Solid State Nucl. Magn. Reson.* **1998**, *11*, 265-268.

[61] Earl, W. L. Measurement of ^{13}C chemical shifts in solids. *J. Magn. Res.* **1969**, *48*, 35-54.

[62] Marion, D.; Wuthrich, K. Application of phase sensitive two-dimensional correlated spectroscopy (COSY) for measurements of ^{1}H- ^{1}H spin-spin coupling constants in proteins. *Biochem. Biophys. Res. Co.* **1983**, *113*, 967-974.

[63] Ramsey, N. F. Electron Coupled Interactions between Nuclear Spins in Molecules. *Phys. Rev.* **1953**, *91*, 303-307.

[64] Power, W. P.; Lumsden, M. D.; Wasylishen, R. E. Anisotropic Indirect Spin-Spin Coupling in the Solid State. Experimental Evidence of Noncontact Contributions to $^{1}J(^{31}$P,^{199}Hg). *J. Am. Chem. Soc.* **1991**, *113*, 8257-8262.

[65] Bax, A.; Tjandra, N. Direct Measurement of Distances and Angles in Biomolecules by NMR in a Dilute Liquid Crystalline Medium. *Science*, **1997**, *278*, 1111-1114.

[66] Tolman, J. R.; Flanagan, J. M.; Kennedy, M. A.; Prestegard, J. H. Nuclear magnetic dipole interactions in field-oriented proteins: information for structure determination in solution. *Proc. Nat. Acad. Sci.* **1995**, *92*, 9279-9283.

[67] Viger-Gravel, J.; Leclerc, S.; Korobkov, I.; Bryce, D. L. Direct Investigation of Halogen Bonds by Solid-State Multinuclear Magnetic Resonance Spectroscopy and Molecular Orbital Analysis. *J. Am. Chem. Soc.* **2014,** *136,* 6929-6942.

[68] Viger-Gravel, J.; Leclerc, S.; Korobkov, I.; Bryce, D. L. Correlation between ^{13}C chemical shifts and the halogen bonding environment in a series of solid para-diiodotetrafluorobenzene complexes. *CrystEngComm* **2013,** *15,* 3168-3177.

[69] Bouchmella, K.; Dutremez, S. G.; Alonso, B.; Mauri, F.; Gervais, C. ^{1}H, ^{13}C, and ^{15}N Solid-State NMR Studies of Imidazole- and Morpholine-Based Model Compounds Possessing Halogen and Hydrogen Bonding Capabilities. *Cryst. Growth Des.* **2008,** *8* (11), 3941-3950.

[70] Del Bene, J. E.; Alkorta, I.; Elguero, J. Spin-Spin Coupling across Intermolecular F-Cl···N Halogen Bonds. *J. Phys. Chem. A* **2008,** *112,* 7925-7929.

[71] Del Bene, J. E.; Alkorta, I.; Elguero, J. Ab Initio Study of Ternary Complexes A···NCH···C with A,C = HCN, HF, HCl, ClF, and LiH: Energetics and Spin-Spin Coupling Constants across Intermolecular Bonds. *J. Phys. Chem. A* **2010,** *114* (32), 8463-8473.

[72] Scheiner, S. Comparison of CH···O, SH···O, Chalcogen and Tetrel Bonds Formed by Neutral and Cationic Sulfur-Containing Compounds. *J. Phys. Chem. A.* **2015**, *119*, 9189-9199.

[73] Le Bail, A.; Duroy, H.; Fourquet, J. L. Ab-initio structure determination of $LiSbWO_6$ by X-ray powder diffraction. *Mat. Research Bulletin.* **1988**. *23*, 447-452.

[74] Tremayne, M.; Kariuki, B. M.; Harris, K. D. M. Structure Determination of a Complex Organic Solid from X-Ray Powder Diffraction Data by a Generalized Monte Carlo Method: The Crystal Structure of Red Fluorescein. *Angew. Chem.* **1997**, *36*, 770-772.

[75] Brüning, J.; Schmidt, M. U. The determination of crystal structures of active pharmaceutical ingredients from X-ray powder diffraction data: a brief, practical introduction, with fexofenadine hydrochloride as example. *J. Pharm. Pharmacol.* **2015**. *67*, 773-781.

[76] Jensen, F. *Introduction to Computational Chemistry, 2nd ed.*; John Wiley & Sons Ltd.: New York, 2006.

[77] Born, M.; Oppenheimer, R. Zur Quantentheorie der Molekein. *Ann. Phys-Berlin* **1927**, *389*, 457-484.

[78] Slater, J. C. The Theory of Complex Spectra. *Phys. Rev.* **1929**, *34*, 1293-1322.

[79] Roothaan, C. C. J. New Developments in Molecular Orbital Theory. *Rev. Mod. Phys.* **1951**, *23*, 69-89.

[80] Dunning, T. H. Gaussian basis sets for use in correlated molecular calculations. I. The atoms boron through neon and hydrogen. *J. Chem. Phys.* **1989**, *90*, 1007-1023.

[81] Head-Gordon, M.; Pople, J. A.; Frisch, M. J., MP2 energy evaluation by direct methods. *Chem. Phys. Lett.***1988,** *153*, 503-506.

[82] Saebø, S.; Almlöf, J. Avoiding the integral storage bottleneck in LCAO calculations of electron correlation. *Chem. Phys. Lett.* **1989,** *154,* 83-89

[83] Frisch, M. J.; Head-Gordon, M.; Pople, J. A. Direct MP2 gradient method. *Chem. Phys. Lett.*, **1990**, *166*, 275-280.

[84] Frisch, M. J.; Head-Gordon, M.; Pople, J. A. Semi-direct algorithms for the MP2 energy and gradient. *Chem. Phys. Lett.*, **1990**, *166*, 281-288.

[85] Head-Gordon, M.; Head-Gordon, T. Analytic MP2 Frequencies Without Fifth Order Storage: Theory and Application to Bifurcated Hydrogen Bonds in the Water Hexamer. *Chem. Phys. Lett.* **1994**, *220*, 122-128.

[86] Hohenburg, P.; Kohn, W. Inhomogeneous Electron Gas. *Phys. Rev.* **1964**, *136*, 864-871.

[87] Kohn, W.; Sham, L. J. Density-functional theory in strong magnetic fields. *Phys. Rev. Lett.* **1987**, *59*, 2360-2363.

[88] Perdew, J. P.; Burke, K.; Ernzerhof, M. Generalized Gradient Approximation Made Simple. *Phys. Rev. Lett.* **1996**, *77*, 3865-3868.

[89] Becke, A. D. Density-functional exchange-energy approximation with correct asymptotic behaviour. *Phys. Rev. A*. **1988**, *38*, 3098-3100.

[90] Lee, C.; Yang, W.; Parr, R. G. Development of the Colle-Salvetti correlation-energy formula into a functiuonal of the electron density. *Phys. Rev. B* **1988**, 37, 785-789.

[91] Torres, E.; DiLabio, G. A. A (Nearly) Universally Applicable Method for Modeling Noncovalent Interactions using B3LYP. *J. Phys. Chem. Lett.* **2012**, *3*, 1738-1744.

[92] Johnson, E. R.; Michela, S.; Bietti, M.; DiLabio, G. A. Modelling Noncovalent Radical-Molecule Interactions Using Conventional Density-Functional Theory: Beware Erroneous Charge Transfer. *J. Phys. Chem. A* **2013**, *117*, 947-952.

[93] Becke, A. D. A new mixing of Hartree-Fock and local density-functional theories. *J. Chem. Phys*. **1993**, *98*, 1372-1377.

[94] Yanai, T.; Tew, D.; Handy, N. A new hybrid exchange-correlation functional using the Coulomb-attenuating method (CAM-B3LYP). *Chem. Phys. Lett.* **2004**, *393*, 51-57.

[95] Vydrov, O. A.; Scuseria, G. E. Assessment of a long range corrected hybrid functional. *J. Chem. Phys.* **2006**, *125*, 234109.

[96] Vydrov, O. A.; Heyd, J.; Krukau, A.; Scuseria, G. E. Importance of short-range versus long-range Hartree-Fock exchange for the performance of hybrid density functionals. *J. Chem. Phys.* **2006**, *125*, 074106.

[97] Vydrov, O. A.; Scuseria, G. E.; Perdew, J. P. Tests of functionals for systems with fractional electron number. *J. Chem. Phys.* **2007**, *126*, 154109.

[98] Zhao, Y.; Schultz, N. E.; Truhlar, D. G. Exchange-correlation functional with broad accuracy for metallic and nonmetallic compounds, kinetics, and noncovalent interactions. *J. Chem. Phys.* **2005**, *123*, 161103.

[99] Zhao, Y.; Truhlar, D. G. The M06 suite of density functionals for main group thermochemistry, thermochemical kinetics, noncovalent interactions, excited states, and transition elements: two new functionals and systematic testing of four M06-class functionals and 12 other functionals. *Theor. Chem. Acc.* **2008**, *120*, 215-241.

[100] Kaupp, M.; Buhl, M.; Malkin, V. G. Calculation of NMR and EPR Parameters: Theory and Application. Wiley: New York, 2004.

[101] Helgaker, T.; Jaszuński, M.; Ruud, K. Ab Initio Methods for the Calculation of NMR Shielding and Indirect Spin−Spin Coupling Constants. *Chem. Rev.* **1999**, *99*, 293-352.

[102] Gregor, T.; Mauri, F.; Car, R. A comparison of methods for the calculation of NMR chemical shifts. *J. Chem. Phys.* **1999**, *111*, 1815-1822.

[103] Ditchfield, R. Molecular Orbital Theory of Magnetic Shielding and Magnetic Susceptibility. *J. Chem. Phys.* **1972**, *56*, 5688-5691.

[104] Bonhomme, C.; Gervais, C.; Babonneau, F.; Coelho, C.; Pourpoint, F.; Azaïs, T.; Ashbrook, S. E.; Griffin, J. M.; Yates, J. R.; Mauri, F.; Pickard, C. J. First-principles

calculation of NMR parameters using the gauge including projector augmented wave method: a chemist's point of view. *Chem. Rev.* **2012,** *112,* 5733-5779.

[105] Segall, M. D.; Lindan, P. J. D.; Probert, M. J.; Pickard, C. J.; Hasnip, P. J.; Clark, S. J.; Payne, M. C. First-principles simulation: ideas, illustrations and the CASTEP code. *J. Phys.: Condens. Matter* **2002,** *14*, 2717-2744.

[106] Pickard, C. J.; Mauri, F. All-electron magnetic response with pseudopotentials: NMR chemical shifts. *Phys. Rev. B* **2001**, *63*, 245101.

[107] Boys, S. F.; Bernardi, F. The calculation of small molecular interactions by the differences of separate total energies. Some procedures with reduced errors. *Mol. Phys.* **1970**, *19*, 553-556.

[108] Cramer, C. J. *Essentials of Computational Chemistry: Theories and Models, 2nd ed.*; John Wiley & Sons, Ltd.: West Sussex, 2004.

[109] Burns, L. A.; Marshall, M. S.; Sherill, C. D. Comparing Counterpoise-Corrected, Uncorrected, and Averaged Binding Energies for Benchmarking Noncovalent Interactions. *J. Chem. Theory Comput.* **2014**, *10*, 49-57.

[110] Brown, J. P.; Sorenson, J. B.; Kirschner, K. N. Calculating Interaction Energies Using First Principle Theories: Consideration of Basis Set Superposition Error and Fragment Relaxation. *J. Chem. Ed.* **2007**, *84*, 1225-1229.

[111] Andrew, E. R.; Bradbury, A.; Eades, R. G. Removal of Dipolar Broadening of Nuclear Magnetic Resonance Spectra of Solids by Specimen Rotation. *Nature* **1959**, *183*, 1802-1803.

[112] Lowe, I. J. Free Induction Decays of Rotating Solids. *Phys. Rev. Lett.* **1959**, *2*, 285-287.

[113] Maricq, M. M; Waugh, J. S. NMR in rotating solids. *J. Chem. Phys.* **1979**, *70*, 3300-3316.

[114] Andrew, E. R. The narrowing of NMR spectra of solids by high-speed specimen rotation and the resolution of chemical shift and spin multiplet structures for solids. *Prog. Nuc. Magn. Res. Spect.* **1971**, *8*, 1-39.

[115] Andrew, E. R. Magic angle spinning in solid state n.m.r spectroscopy. *Phil. Trans. R. Soc. Lond. A* **1981**, *299*, 505-520.

[116] Bruker. 111kHz probe for ultra-fast magic angle spinning. https://www.bruker.com/products/mr/nmr/probes/probes/solids/very-fast-mas/07-mm/overview.html (accessed Nov 26, 2015).

[117] JEOL USA. JEOL Resonance Introduces Worlds' Fastest and Smallest Solid State NMR Probe. http://www.jeolusa.com/NEWSEVENTS/PressReleases/tabid/314/ID/270/JEOL-Resonance-Introduces-Worlds-Fastest-and-Smallest-Solid-State-NMR-Probe.aspx (accessed Nov 26, 2015).

[118] Hartmann, S. R.; Hahn, E. L. Nuclear Double Resonance in the Rotating Frame. *Phys. Rev.* **1962**, *128*, 2042-2053.

[119] Bruno, G.; Rotondo, A.; De Luca, L; Sammartano, S.; Nicolo, F. N,N,N',N'-Tetra-methyl-ethyl-ene-diammonium-succinate-succinic acid. *Acta Crystallogr. C* **2004**, *C60*, o287-o289.

[120] Kabak, M.; Elerman, Y.; Ünaleroglu, C.; Mert, Y.; Durlu, T. N. N,N,N',N'-Tetra-methyl-ethyl-enedi-ammonium dichloride. *Acta Crystallogr. C* **2000**, *C56*, e66-e67.

[121] Grimme, S.; Antony, J.; Ehrlich, S.; Krieg, H. A consistent and accurate ab initio parameterization of density functional dispersion correction (DFT-D) for the 94 elements H-Pu. *J. Chem. Phys*. **2010**, *132*, 154104.

[122] Frisch, M. J.; Trucks, G. W.; Schlegel, H. B.; Scuseria, G. E.; Robb, M. A.; Cheeseman, J. R.; Scalmani, G.; Barone, V.; Mennucci, B.; Petersson, G. A.; Nakatsuji, H.; Caricato, M.; Li, X.; Hratchian, H. P.; Izmaylov, A. F.; Bloino, J.; Zheng, G.; Sonnenberg, J. L.; Hada, M.; Ehara, M.; Toyota, K.; Fukuda, R.; Hasegawa, J.; Ishida, M.; Nakajima, T.; Honda, Y.; Kitao, O.; Montgomery, J. A. . J.; Peralta, J. E.; Olgiaro, F.; Bearpark, M.; Heyd, J. J.; Brothers, E.; Kudin, K. N.; Staroverov, V. N.; Keith, T.; Kobayaski, R.; Normand, J.; Raghavachari, K.; Rendell, A.; Burant, J. C.; Iyengar, S. S.; Tomasi, J.; Cossi, M.; Rega, N.; Millam, J. M.; Klene, M.; Knox, J. E.; Cross, J. B.; Bakken, V.; Adamo, C.; Jaramillo, J.; Gomperts, R.; Stratmann, R. E.; Yazyev, O.; Austin, A. J.; Cammi, R.; Pomelli, C.; Ochterski, J. W.; Martin, R. L.; Morokuma, K.; Zakrzewski, V. G.; Voth, G. A.; Salvador, P.; Dannenberg, J. J.; Dapprich, S.; Daniels, A. D.; Farkas, O.; Foresman, J. B.; Ortiz, J. V.; Cioslowski, J.; Fox, D. J. *Gaussian 09* Revision D.01, Gaussian Inc., Wallingford, CT, 2013.

[123] Dennington II, R.; Keith, T.; Milliam, J. GaussView, Version 4.1. *Semichem Inc., Shawnee Mission, KS* **2007**.

[124] Adiga, S.; Aebi, D.; Bryce, D. L. A Program for Parsing and Summarizing the Results of Electric Field Gradient and Nuclear Magnetic Shielding Tensor Calculations. *Can. J. Chem.* **2007,** *85,* 496-505.

[125] Jameson, A. K.; Jameson, C. J. Gas-phase ^{13}C chemical shifts in the zero-pressure limit: refinements to the absolute shielding scale for ^{13}C. *Phys. Chem. Lett.* **1987,** *134* (5), 461-466.

[126] Pedone, A.; Pavone, M.; Menziani, M. C.; Barone, V. Accurate First-Principle Prediction of ^{29}Si and ^{17}O NMR Parameters in SiO_2 Polymorphs: The Cases of Zeolites Sigma-2 and Ferrierite. *J. Chem. Theory Comput.* **2008**, *4*, 2130-2140.

---

[127] Perdew, J. P.; Burke, K.; Ernzerhof, M. Generalized gradient approximation made simple. *Phys. Rev. Lett.* **1996,** *77,* 3865-3868.

[128] Yates, J. R.; Pickard, C. J.; Mauri, F. Calculation of NMR chemical shifts for extended systems using ultrasoft pseudopotentials. *Phys. Rev. B* **2007**, *76*, 024401.

[129] Green, T. F. G.; Yates, J. R. Relativistic nuclear magnetic resonance J-coupling with ultrasoft pseudopotentials and zeroth-order regular approximation. *J. Chem. Phys.* **2014**, *140*, 234106.

[130] Zhao, Y.; Truhlar, D. G. Comparative DFT Study of van der Waals Complexes: Rare-Gas Dimers, Alkaline-Earth Dimers, Zinc Dimer, and Zinc-Rare-Gas Dimers. *J. Phys. Chem. A* **2006**, *110*, 5121-5129.

[131] Zhao, Y.; Truhlar, D. G. Density Functional for Spectroscopy: No Long-Range Self-Interaction Error, Good Performance for Rydberg and Charge-Transfer States, and Better Performance on Average than B3LYP for Ground States. *J. Phys. Chem. A* **2006**, *110*, 13126-13130.

[132] Purvis III, G. D.; Bartlett, R. J. A full coupled-cluster singles and doubles model - the inclusion of disconnected triples. *J. Chem. Phys.* **1982**, *76*, 1910-1918.

[133] Scuseria, G. E.; Janssen, C. L.; Schaefer III, H. F. An efficient reformulation of the closed-shell coupled cluster single and double excitation (CCSD) equations. *J. Chem. Phys.* **1988**, *89*, 7382-7387.

[134] Pople, J. A.; Head-Gordon, M.; Raghavachari, K. Quadratic configuration interaction. A general technique for determining electron correlation energies. *J. Chem. Phys.*, **1987**, *87*, 5968-5875.

[135] Akitsu, T.; Einaga, Y. Structures, magnetic properties, and XPS of cyanide-bridged $Nd^{III}/Sm^{III}/Gd^{III}–Cr^{III}$ complexes. *Inorg. Chim. Acta.* **2006,** *359*, 1421-1426.

[136] Minemawari, H.; Naito, T.; Inabe, T. Self-Organized Anionic Networks in Quaternary Ammonium and Phosphonium Salts of Mellitate. *Bull. Chem. Soc. Jpn.* **2010,** *83*, 505-513.

[137] Attell, R. J.; Widdifield, C. M.; Korobkov, I. Bryce, D. L. Weak halogen bonding in solid haloanilinium halides probed directly via chlorine-35, bromine-81, and iodine-127 NMR spectroscopy. *Cryst. Growth Des.* **2012**, *12*, 1641-1653.

[138] Grzesiek, S.; Cordier, S.; Jaravine, V.; Barfield, M. Insights into biomolecular hydrogen bonds from hydrogen bond scalar couplings. *Prog. Nucl. Mag. Res. Sp.* **2004,** *45,* 275-300.

[139] Dingley, A. J.; Grzesiek, S. Direct Observation of Hydrogen Bonds in Nucleic Acid Pairs by Internucleotide $^{2}J_{NN}$ Couplings. *J. Am. Chem. Soc.* **1998,** *120* (33), 8293-8297.

[140] Brown, S. P.; Pérez-Torralba, M.; Sanz, D.; Claramunt, R. M.; Emsley, L. Determining hydrogen-bond strengths in the solid state by NMR: the quantitative measurement of homonuclear *J* couplings. *Chem. Commun.* **2002,** 1852-1853.

[141] Benedict, H.; Shenderovich, I. G.; Malkina, O. L.; Malkin, V. G.; Denisov, G. S.; Golubev, N. S.; Limach, H.-H. Nuclear Scalar Spin-Spin Couplings and Geometries of Hydrogen Bonds. *J. Am. Chem. Soc.* **2000,** *122,* 1979-1988.

[142] Ledbetter, M. P.; Saielli, G.; Bagno, A.; Tran, N.; Romalis, M. V. Observation of scalar nuclear spin–spin coupling in van der Waals complexes. *Proc. Nat. Acad. Sci. USA* **2012,** *109* (31), 12393-12397.

[143] Plevin, M. J.; Bryce, D. L.; Boisbouvier, J. Direct detection of CH/π interactions in proteins. *Nat. Chem.* **2010,** *2*, 466-471.

[144] Pervushin, K.; Ono, A.; Fernández, C.; Szperksi, T.; Kainosho, M.; Wüthrich, K. NMR scalar couplings across Watson–Crick base pair hydrogen bonds in DNA observed by transverse relaxation-optimized spectroscopy. *Proc. Natl. Acad. Sci. USA* **1998,** *95* (24), 14147-14151.

[145] Del Bene, J. E.; Alkorta, I.; Elguero, J. P···N Pnicogen Bonds in Cationic Complexes of F_4P^+ and F_3HP^+ with Nitrogen Bases. *J. Phys. Chem. A* **2015,** *119*, 3125-3133.

[146] Del Bene, J. E.; Alkorta, I.; Elguero, J. Properties of Complexes $H_2C{=}(X)P{:}PXH_2$, for X = F, Cl, OH, CN, NC, CCH, H, CH_3, and BH_2: P···P Pnicogen Bonding at σ-Holes and π-Holes. *J. Phys. Chem. A* **2013**, *117*, 11592-11604.

[147] Vaara, J.; Jokisaari, J; Wasylishen, R. E.; Bryce, D. L. Spin-Spin Coupling Tensors as Determined by Experiment and Computational Chemistry. *Prog. Nucl. Magn. Reson. Spectrosc.* **2002**, *41*, 233-304.

[148] Desiraju, G. R.; Ho, P. S.; Kloo, L.; Legon, A. C.; Marquardt, R.; Politzer, P.; Metrangolo, P.; Resnati, G.; Rissanen, K. Definition of the halogen bond (IUPAC Recommendations 2013). *Pure Appl. Chem.* **2013,** *85* (8), 1711-1713.

[149] Ilczyszyn, I.; Godzisz, D.; Ilczyszyn, M. M. Sarcosine-maleic acid (1:1) crystal: structure, ^{13}C NMR and vibrational properties, protonation character. *Spectrochim. Acta A* **2003,** *59,* 1815-1828.

[150] Surprenant, H. L.; Sarneski, J. E.; Key, R. R.; Byrd, J. T.; Reilly, C. N. Carbon-13 NMR Studies of Amino Acids: Chemical Shifts, Protonation Shifts, Microscopic Protonation Behaviour. *J. Mag. Res.* **1980,** *40,* 231-243.

[151] Batchelor, J. G.; Feeney, J.; Roberts, G. C. K. Carbon-13 NMR Protonation Shifts of Amines, Carboxylic Acids and Amino Acids. *J. Mag. Res.* **1975,** *20,* 19-38.

[152] Thursfield, A.; Anderson, M. W.; Dwyer, J.; Hutchings, G. J.; Lee, D. ^{13}C and ^{15}N solid-state MAS NMR study of the conversion of methanol and ammonia over H-SAPO-34 microporous catalysts. *J. Chem. Soc., Farady Trans.* **1998,** *94* (8), 1119-1122.

[153] Jiang, Y.; Hunger, M.; Wang, W. On the Reactivity of Surface Methoxy Species in Acidic Zeolites. *J. Am. Chem. Soc.* **2006,** *128,* 11679-11692.

Appendix I – Supplementary Data

Table 6. Raw data obtained from calculations (BHandHLYP/6-311++G(d,p)) of $^{1c}J(^{13}C,^{17}O/^{15}N)$ in model structures. All values are reported in Hz.

Model Structure	Interaction Distance /Å	FC	SD	PSO	DSO	Total *J*	%FC
1	2.825	-5.7774400	-0.0033046	0.2211940	-0.0384239	-5.5979800	103.21
	2.925	-4.4712100	-0.0046878	0.1923000	-0.0361786	-4.3197800	103.51
	3.025	-3.4094900	-0.0053476	0.1677860	-0.0341417	-3.2811900	103.91
	3.125	-2.6226900	-0.0055014	0.1470290	-0.0322869	-2.5134500	104.35
	3.225	-1.9885400	-0.0053855	0.1294620	-0.0305911	-1.8950500	104.93
	3.325	-1.4673700	-0.0051835	0.1145940	-0.0290354	-1.3870000	105.79
2	2.825	-5.9705500	-0.0078246	0.1891870	-0.0452860	-5.8344800	102.33
	2.925	-4.6327300	-0.0069752	0.1657100	-0.0427530	-4.5167500	102.57
	3.025	-3.5428000	-0.0061207	0.1452890	-0.0404468	-3.4440800	102.87
	3.125	-2.7252700	-0.0052762	0.1276690	-0.0383392	-2.6412200	103.18
	3.225	-2.0759500	-0.0045096	0.1125460	-0.0364059	-2.0043200	103.57
	3.325	-1.5376900	-0.0039040	0.0996200	-0.0346266	-1.4766000	104.14
3	2.825	-8.4040300	-0.0281782	0.1026520	-0.0426263	-8.3721800	100.38
	2.925	-6.5924800	-0.0231170	0.0990098	-0.0401181	-6.5567000	100.55
	3.025	-5.1447500	-0.0190264	0.0943790	-0.0378430	-5.1072400	100.73
	3.125	-3.9759900	-0.0157842	0.0892440	-0.0357710	-3.9383000	100.96
	3.225	-3.0596900	-0.0131830	0.0839403	-0.0338769	-3.0228100	101.22
	3.325	-2.3299300	-0.0111324	0.0786916	-0.0321394	-2.2945100	101.54
4	2.825	-6.8198200	-0.0044630	0.1741670	-0.0416687	-6.6917800	101.91
	2.925	-5.3073500	-0.0047536	0.1525780	-0.0392216	-5.1987400	102.09
	3.025	-4.0825800	-0.0046334	0.1342270	-0.0370014	-3.9899800	102.32
	3.125	-3.1550400	-0.0042736	0.1186300	-0.0349796	-3.0756700	102.58
	3.225	-2.4098300	-0.0037883	0.1053690	-0.0331312	-2.3413800	102.92
	3.325	-1.7981900	-0.0033615	0.0940816	-0.0314359	-1.7389100	103.41
5	2.825	-9.8252900	-0.0168635	0.0579256	-0.0483889	-9.8326100	99.93
	2.925	-7.7046100	-0.0132438	0.0628782	-0.0457005	-7.7006800	100.05
	3.025	-6.0094900	-0.0105396	0.0647445	-0.0432492	-5.9985400	100.18
	3.125	-4.6638700	-0.0085171	0.0645585	-0.0410055	-4.6488400	100.32
	3.225	-3.5875200	-0.0070535	0.0630627	-0.0389446	-3.5704500	100.48
	3.325	-2.7701800	-0.0058979	0.0607799	-0.0370452	-2.7523400	100.65
6	2.825	-9.9455000	-0.0232848	0.0420864	-0.0432029	-9.9699000	99.76
	2.925	-7.8446900	-0.0165779	0.0470122	-0.0407596	-7.8550200	99.87
	3.025	-6.1444700	-0.0115388	0.0484756	-0.0385370	-6.1460700	99.97

	3.125	-4.7858100	-0.0077824	0.0477239	-0.0365071	-4.7823800	100.07
	3.225	-3.7199100	-0.0050022	0.0456410	-0.0346461	-3.7139200	100.16
	3.325	-2.8793500	-0.0029973	0.0428363	-0.0329341	-2.8724500	100.24
7	2.825	-6.6463000	-0.0044124	0.1966320	-0.0454815	-6.4995600	102.26
	2.925	-5.1631800	-0.0053627	0.1717160	-0.0428884	-5.0397200	102.45
	3.025	-3.9694600	-0.0056746	0.1507090	-0.0405297	-3.8649600	102.70
	3.125	-3.0572400	-0.0055989	0.1329750	-0.0383764	-2.9682400	103.00
	3.225	-2.3201700	-0.0053059	0.1179810	-0.0364033	-2.2439000	103.40
	3.325	-1.7354800	-0.0049659	0.1052800	-0.0345894	-1.6697600	103.94
8	2.825	-0.1271800	0.0361270	0.0242229	-0.0618174	-0.1286480	98.86
	2.925	-0.0054982	0.0319578	0.0221303	-0.0566491	-0.0080593	68.22
	3.025	0.0631498	0.0283092	0.0202108	-0.0520746	0.0595952	105.96
	3.125	0.1003810	0.0251565	0.0185288	-0.0480110	0.0960552	104.50
	3.225	0.1167330	0.0224498	0.0170902	-0.0443888	0.1118850	104.33
	3.325	0.1160610	0.0201338	0.0158772	-0.0411491	0.1109230	104.63
9	2.825	-4.2597800	0.0225266	-0.0167204	-0.0587748	-4.3127500	98.77
	2.925	-3.3080100	0.0235869	-0.0086157	-0.0546399	-3.3476700	98.82
	3.025	-2.5653100	0.0236232	-0.0031007	-0.0509301	-2.5957100	98.83
	3.125	-1.9577100	0.0229638	0.0006016	0.0006016	-1.9817400	98.79
	3.225	-1.4938800	0.0219128	0.0030470	-0.0445719	-1.5135000	98.70
	3.325	-1.1350300	0.0206610	0.0046335	-0.0418364	-1.1515700	98.56
10	2.825	-6.0983126	0.0017227	0.0050878	-0.0329137	-6.1244174	99.57
	2.925	-4.9026536	0.0013808	0.0072425	-0.0310196	-4.9250411	99.55
	3.025	-3.9133502	0.0011910	0.0082917	-0.0292960	-3.9331708	99.50
	3.125	-3.1038207	0.0010870	0.0086249	-0.0277219	-3.1218317	99.42
	3.225	-2.4422932	0.0010361	0.0085185	-0.0262793	-2.4590137	99.32
	3.325	-1.9123558	0.0010064	0.0081643	-0.0249530	-1.9281365	99.18
11	2.825	-7.2071145	-0.0094666	0.0007135	-0.0331168	-7.2489860	99.42
	2.925	-5.7420051	-0.0097103	0.0041096	-0.0313214	-5.7789250	99.36
	3.025	-4.5406510	-0.0095844	0.0060870	-0.0296808	-4.5738396	99.27
	3.125	-3.5653329	-0.0346615	0.0071027	-0.0281762	-3.5956599	99.16
	3.225	-2.7938314	-0.0087708	0.0074845	-0.0267919	-2.8219140	99.00
	3.325	-2.1646509	-0.0082427	0.0074672	-0.0255144	-2.1909380	98.80
12	2.825	-10.0660045	-0.0078429	-0.0085749	-0.0343485	-10.1167693	99.50
	2.925	-8.1384291	-0.0081146	-0.0036897	-0.0324641	-8.1826852	99.46
	3.025	-6.5352910	-0.0081154	-0.0003020	-0.0307434	-6.5744412	99.40
	3.125	-5.2075650	-0.0079637	0.0019808	-0.0291667	-5.2427174	99.33
	3.225	-4.1433839	-0.0076689	0.0034615	-0.0277172	-4.1753100	99.24
	3.325	-3.2698338	-0.0073289	0.0043746	-0.0263804	-3.2991789	99.11
13	2.825	-8.1897100	-0.0169981	0.1368380	-0.0484516	-8.1183300	100.88
	2.925	-6.3826800	-0.0157425	0.1239260	-0.0456354	-6.3201300	100.99
	3.025	-4.9396400	-4.9396400	0.1126660	-0.0430766	-4.8843300	101.13

	3.125	-3.8350900	-0.0127527	0.1027790	-0.0407428	-3.7858100	101.30
	3.225	-2.9168100	-0.0113448	0.0940566	-0.0386065	-2.8727000	101.54
	3.325	-2.1867600	-0.0101220	0.0863351	-0.0366446	-2.1471900	101.84
14	2.825	-8.5663459	-0.0077326	0.0062075	-0.0357135	-8.6035743	99.57
	2.925	-6.9161603	-0.0089168	0.0062827	-0.0337083	-6.9525050	99.48
	3.025	-5.5426070	-0.0094103	0.0062205	-0.0318789	-5.5776753	99.37
	3.125	-4.3996486	-0.0094761	0.0060534	-0.0302040	-4.4332861	99.24
	3.225	-3.4964308	-0.0092233	0.0058142	-0.0286656	-3.5285112	99.09
	3.325	-2.7531803	-0.0088270	0.0055360	-0.0272486	-2.7837317	98.90
15	2.825	-9.3865782	-0.0086330	0.0116579	-0.0359643	-9.4195283	99.65
	2.925	-7.6781092	-0.0087286	0.0128835	-0.0339973	-7.7079593	99.61
	3.025	-6.2383752	-0.0085638	0.0133839	-0.0322006	-6.2657564	99.56
	3.125	-5.0195290	-0.0082747	0.0133938	-0.0305540	-5.0449605	99.50
	3.225	-4.0311234	-0.0078702	0.0130872	-0.0290397	-4.0549417	99.41
	3.325	-3.2214115	-0.0074234	0.0125935	-0.0276429	-3.2438833	99.31
16	2.825	-8.8206187	-0.0098034	0.0101711	-0.0340361	-8.8542983	99.62
	2.925	-7.1904781	-0.0100231	0.0109761	-0.0321483	-7.2216749	99.57
	3.025	-5.8218064	-0.0098948	0.0112125	-0.0304252	-5.8509131	99.50
	3.125	-4.6605283	-0.0095923	0.0110726	-0.0288471	-4.6878956	99.42
	3.225	-3.7354560	-0.0091251	0.0106975	-0.0273967	-3.7612802	99.31
	3.325	-2.9739700	-0.0086028	0.0101924	-0.0260599	-2.9984336	99.18

Table 7. Raw data obtained from calculations (LC-ωPBE-D3/6-311++G(d,p)) of $^{1c}J(^{13}C,^{17}O/^{15}N)$ in model structures. All values are reported in Hz.

Model Structure	Interaction Distance /Å	FC	SD	PSO	DSO	Total *J*	%FC
1	2.825	-5.7930600	0.0005746	0.2305720	-0.0378695	-5.5997800	103.45
	2.925	-4.4339900	-0.0015727	0.1988320	-0.0356548	-4.2723800	103.78
	3.025	-3.3752800	-0.0027946	0.1723260	-0.0336477	-3.2393900	104.19
	3.125	-2.5495100	-0.0034511	0.1501720	-0.0318206	-2.4346100	104.72
	3.225	-1.9178000	-0.0037408	0.1316800	-0.0301513	-1.8200100	105.37
	3.325	-1.4341400	-0.0038239	0.1162390	-0.0286203	-1.3503400	106.21
2	2.825	-6.0089700	-0.0039513	0.1973090	-0.0446880	-5.8603000	102.54
	2.925	-4.6076600	-0.0041334	0.1710760	-0.0421888	-4.4829000	102.78
	3.025	-3.5145100	-0.0040177	0.1487570	-0.0399152	-3.4096900	103.07
	3.125	-2.6592700	-0.0037775	0.1298370	-0.0378379	-2.5710500	103.43
	3.225	-2.0049800	-0.0034803	0.1138820	-0.0359334	-1.9305100	103.86
	3.325	-1.5022400	-0.0031926	0.1004780	-0.0341809	-1.4391400	104.38
3	2.825	-8.0576200	-0.0185941	0.1264120	-0.0420964	-7.9918900	100.82
	2.925	-6.2217000	-0.0154347	0.1174050	-0.0396212	-6.1593500	101.01
	3.025	-4.7801800	-0.0128509	0.1086360	-0.0373767	-4.7217700	101.24
	3.125	-3.6555100	-0.0107681	0.1003280	-0.0353333	-3.6012800	101.51
	3.225	-2.7776700	-0.0091113	0.0926012	-0.0334664	-2.7276500	101.83
	3.325	-2.0962600	-0.0077884	0.0855118	-0.0317541	-2.0503000	102.24
4	2.825	-5.7844300	0.0047817	0.0188364	-0.0397117	-5.8005200	99.72
	2.925	-4.4449100	0.0082895	0.0222445	-0.0372518	-4.4516300	99.85
	3.025	-3.3955600	0.0105454	0.0235193	-0.0350296	-3.3965200	99.97
	3.125	-2.5780700	0.0118609	0.0234633	-0.0330136	-2.5757600	100.09
	3.225	-1.9454700	0.0124985	0.0226469	-0.0311780	-1.9415000	100.20
	3.325	-1.4600600	0.0126354	0.0214541	-0.0295010	-1.4554700	100.32
5	2.825	-8.6371600	-0.0238427	0.0770242	-0.0486771	-8.6326500	100.05
	2.925	-6.6935800	-0.0185794	0.0771373	-0.0459368	-6.6809600	100.19
	3.025	-5.1581700	-0.0145455	0.0753837	-0.0434429	-5.1407700	100.34
	3.125	-3.9584100	-0.0114704	0.0725040	-0.0411647	-3.9385400	100.50
	3.225	-3.0268100	-0.0091289	0.0690134	-0.0390758	-3.0060000	100.69
	3.325	-2.2919700	-0.0073697	0.0652748	-0.0371536	-2.2712100	100.91
6	2.825	-8.6341500	-0.0259481	0.0489777	-0.0426850	-8.6538100	99.77
	2.925	-6.7649200	-0.0185392	0.0515617	-0.0402109	-6.7721100	99.89
	3.025	-5.2718700	-0.0130305	0.0511891	-0.0379651	-5.2716700	100.00
	3.125	-4.0920500	-0.0089577	0.0490449	-0.0359182	-4.0878800	100.10
	3.225	-3.1649200	-0.0059782	0.0459344	-0.0340456	-3.1590100	100.19
	3.325	-2.4350000	-0.0038355	0.0423882	-0.0323268	-2.4287700	100.26

7	2.825	-6.3439100	-0.0008079	0.1601130	-0.0446853	-6.2292900	101.84
	2.925	-4.8702400	-0.0007546	0.1404440	-0.0421074	-4.7726600	102.04
	3.025	-3.7187100	-0.0005144	0.1236560	-0.0397662	-3.6353400	102.29
	3.125	-2.8191100	-0.0002304	0.1093600	-0.0376309	-2.7476100	102.60
	3.225	-2.1278400	0.0000373	0.0972072	-0.0356767	-2.0662700	102.98
	3.325	-1.5945700	0.0002389	0.0868906	-0.0338823	-1.5413200	103.45
8	2.825	-0.0065126	0.0424602	-0.0140986	-0.0606358	-0.0387867	16.79
	2.925	0.0932412	0.0374877	-0.0125142	-0.0554818	0.0627329	148.63
	3.025	0.1433280	0.0331336	-0.0112246	-0.0509129	0.1143240	125.37
	3.125	0.1589070	0.0293612	-0.0100983	-0.0468571	0.1313130	121.01
	3.225	0.1547720	0.0261089	-0.0090655	-0.0432445	0.1285710	120.38
	3.325	0.1401710	0.0233153	-0.0081110	-0.0400161	0.1153590	121.51
9	2.825	-3.8412100	0.0218847	-0.0399006	-0.0573358	-3.9165600	98.08
	2.925	-2.9196000	0.0231508	-0.0299731	-0.0532334	-2.9796600	97.98
	3.025	-2.2028100	0.0233431	-0.0226304	-0.0495549	-2.2516500	97.83
	3.125	-1.6537800	0.0228383	-0.0171975	-0.0462446	-1.6943800	97.60
	3.225	-1.2342900	0.0218951	-0.0131471	-0.0432560	-1.2688000	97.28
	3.325	-0.9143350	0.0206784	-0.0101024	-0.0405491	-0.9443080	96.83
10	2.825	-5.0430248	0.0112429	0.0012606	-0.0312384	-5.0617512	99.63
	2.925	-3.9877650	0.0108981	0.0040728	-0.0293312	-4.0021290	99.64
	3.025	-3.1304585	0.0104404	0.0056437	-0.0276050	-3.1419749	99.63
	3.125	-2.4431769	0.0099019	0.0063992	-0.0260362	-2.4529119	99.60
	3.225	-1.8972484	0.0093185	0.0066469	-0.0246053	-1.9058893	99.55
	3.325	-1.4671574	0.0087180	0.0066010	-0.0232960	-1.4751389	99.46
11	2.825	-5.7626112	0.0081290	-0.0051309	-0.0318689	-5.7914934	99.50
	2.925	-4.5365971	0.0078691	-0.0016199	-0.0300013	-4.5603594	99.48
	3.025	-3.5495101	0.0075152	0.0005860	-0.0283064	-3.5697094	99.43
	3.125	-2.7569817	0.0071012	0.0019020	-0.0267618	-2.7747402	99.36
	3.225	-2.1339030	0.0066569	0.0026323	-0.0253497	-2.1499643	99.25
	3.325	-1.6435928	0.0062063	0.0029931	-0.0240543	-1.6584477	99.10
12	2.825	-9.4753289	-0.0079882	-0.0035862	-0.0332475	-9.5201602	99.53
	2.925	-7.5293777	-0.0088041	-0.0003627	-0.0314226	-7.5699727	99.46
	3.025	-5.9442648	-0.0091312	0.0018270	-0.0297575	-5.9813249	99.38
	3.125	-4.6686922	-0.0091330	0.0032552	-0.0282329	-4.7028066	99.27
	3.225	-3.6511519	-0.0089259	0.0041419	-0.0268324	-3.6827554	99.14
	3.325	-2.8424500	-0.0085870	0.0046485	-0.0255417	-2.8719354	98.97
13	2.825	-7.8771000	-0.0100444	0.1495560	-0.0475216	-7.7851100	101.18
	2.925	-6.0514700	-0.0098800	0.1336920	-0.0447581	-5.9724100	101.32
	3.025	-4.6218300	-0.0093202	0.1201630	-0.0422482	-4.5532400	101.51
	3.125	-3.5144200	-0.0085856	0.1085420	-0.0399601	-3.4544200	101.74
	3.225	-2.6609300	-0.0077988	0.0985066	-0.0378669	-2.6080900	102.03
	3.325	-2.0001200	-0.0070462	0.0898050	-0.0359449	-1.9533100	102.40

14	2.825	-8.0504779	-0.0086993	0.0019223	-0.0351461	-8.0923915	99.48
	2.925	-6.3727006	-0.0097991	0.0023905	-0.0331664	-6.4132675	99.37
	3.025	-5.0120525	-0.0101808	0.0027250	-0.0313618	-5.0508660	99.23
	3.125	-3.9226503	-0.0101107	0.0029358	-0.0297108	-3.9595421	99.07
	3.225	-3.0599713	-0.0097701	0.0030532	-0.0281957	-3.0948853	98.87
	3.325	-2.3747518	-0.0092785	0.0031025	-0.0268011	-2.4077299	98.63
15	2.825	-8.8160037	-0.0147454	-0.0083638	0.0112335	-8.8488136	99.63
	2.925	-7.0870689	-0.0087491	0.0120321	-0.0337284	-7.1175081	99.57
	3.025	-5.6569857	-0.0087716	0.0122744	-0.0319444	-5.6854330	99.50
	3.125	-4.4917659	-0.0085585	0.0121476	-0.0303102	-4.5184879	99.41
	3.225	-3.5477006	-0.0082177	0.0117955	-0.0288083	-3.5729357	99.29
	3.325	-2.7903526	-0.0077974	0.0113178	-0.0274235	-2.8142551	99.15
16	2.825	-8.2436899	-0.0097808	0.0081368	-0.0337594	-8.2790948	99.57
	2.925	-6.5982315	-0.0101530	0.0088711	-0.0318835	-6.6314061	99.50
	3.025	-5.2452002	-0.0101079	0.0091352	-0.0301724	-5.2763408	99.41
	3.125	-4.1488545	-0.0098008	0.0090849	-0.0286063	-4.1781856	99.30
	3.225	-3.2638301	-0.0093544	0.0088430	-0.0271679	-3.2915059	99.16
	3.325	-2.5570505	-0.0088253	0.0084941	-0.0258431	-2.5832255	98.99

Table 8. Raw data obtained from calculations (CAM-B3LYP/6-311++G(d,p)) of $^{1c}J(^{13}\mathrm{C},^{17}\mathrm{O}/^{15}\mathrm{N})$ in model structures. All values are reported in Hz.

Model Structure	Interaction Distance /Å	FC	SD	PSO	DSO	Total *J*	%FC
1	2.825	-6.2104200	0.0006354	0.2383710	-0.0378105	-6.0092200	103.35
	2.925	-4.8158300	-0.0011225	0.2062680	-0.0356041	-4.6462900	103.65
	3.025	-3.6902000	-0.0021042	0.1791590	-0.0336026	-3.5467500	104.04
	3.125	-2.8359600	-0.0025646	0.1562930	-0.0317799	-2.7140200	104.49
	3.225	-2.1588400	-0.0027119	0.1370110	-0.0301135	-2.0546500	105.07
	3.325	-1.6102800	-0.0027199	0.1207470	-0.0285847	-1.5208400	105.88
2	2.825	-6.4276600	-0.0056128	0.2037530	-0.0446052	-6.2741200	102.45
	2.925	-4.9976400	-0.0049976	0.1777020	-0.0421144	-4.8670500	102.68
	3.025	-3.8414700	-0.0043257	0.1551460	-0.0398466	-3.7305000	102.97
	3.125	-2.9557000	-0.0036523	0.1357460	-0.0377741	-2.8613800	103.30
	3.225	-2.2586300	-0.0030270	0.1191450	-0.0358729	-2.1783800	103.68
	3.325	-1.6914400	-0.0025173	0.1049920	-0.0341229	-1.6230900	104.21
3	2.825	-9.0551400	-0.0256854	0.1088650	-0.0419433	-9.0139000	100.46
	2.925	-7.1200400	-0.0207014	0.1042500	-0.0394793	-7.0759700	100.62
	3.025	-5.5681900	-0.0167037	0.0988112	-0.0372440	-5.5233300	100.81
	3.125	-4.3144800	-0.0135585	0.0930015	-0.0352083	-4.2702400	101.04
	3.225	-3.3335000	-0.0110549	0.0871303	-0.0333473	-3.2907700	101.30
	3.325	-2.5535900	-0.0090947	0.0814030	-0.0316400	-2.5129200	101.62
4	2.825	-7.1509900	-0.0019952	0.1554770	-0.0408194	-7.0383300	101.60
	2.925	-5.5707300	-0.0014109	0.1368530	-0.0384047	-5.4736900	101.77
	3.025	-4.3104500	-0.0007735	0.1207300	-0.0362150	-4.2267100	101.98
	3.125	-3.3226400	-0.0001830	0.1068230	-0.0342220	-3.2502300	102.23
	3.225	-2.5426600	0.0003509	0.0948642	-0.0324011	-2.4798500	102.53
	3.325	-1.9248700	0.0007476	0.0846023	-0.0307318	-1.8702500	102.92
5	2.825	-11.3519000	-0.0000491	0.0587627	-0.0469496	-11.3402000	100.10
	2.925	-8.9184400	-0.0000178	0.0642715	-0.0443818	-8.8985700	100.22
	3.025	-6.9600600	-0.0001478	0.0664115	-0.0420362	-6.9358300	100.35
	3.125	-5.4113300	-0.0003671	0.0663145	-0.0398857	-5.3852700	100.48
	3.225	-4.1959700	-0.0005823	0.0647892	-0.0379071	-4.1696700	100.63
	3.325	-3.2160800	-0.0008257	0.0624041	-0.0360810	-3.1905800	100.80
6	2.825	-11.0661000	-0.0140711	0.0547235	-0.1367140	-11.0675000	99.99
	2.925	-8.7333600	-0.0095469	0.0582667	-0.0397536	-8.7243900	100.10
	3.025	-6.8520700	-0.0061800	0.0584133	-0.0376087	-6.8374400	100.21
	3.125	-5.3524900	-0.0037196	0.0564311	-0.0356474	-5.3354200	100.32
	3.225	-4.1732400	-0.0019123	0.0532124	-0.0338471	-4.1557800	100.42
	3.325	-3.2355700	-0.0006361	0.0493699	-0.0321893	-3.2190200	100.51

7	2.825	-7.1771300	-0.0009220	0.2193690	-0.0448664	-7.0035500	102.48
	2.925	-5.5848300	-0.0025383	0.1904710	-0.0423171	-5.4392200	102.68
	3.025	-4.2988900	-0.0033561	0.1662810	-0.0399979	-4.1759700	102.94
	3.125	-3.3196100	-0.0036502	0.1459850	-0.0378803	-3.2151500	103.25
	3.225	-2.5300200	-0.0036433	0.1289110	-0.0359396	-2.4407000	103.66
	3.325	-1.8971400	-0.0035336	0.1145110	-0.0341552	-1.8203200	104.22
8	2.825	-0.1206650	0.0298742	0.0218952	-0.0610709	-0.1299660	92.84
	2.925	0.0040753	0.0264024	0.0202067	0.0525804	0.0049529	82.28
	3.025	0.0732845	0.0233542	0.0186079	-0.0514273	0.0638193	114.83
	3.125	0.1084270	0.0207182	0.0171776	-0.0474058	0.0989171	109.61
	3.225	0.1225330	0.0184569	0.0159364	-0.0438214	0.1131050	108.34
	3.325	0.1202560	0.0165275	0.0148781	-0.0406157	0.1110460	108.29
9	2.825	-4.5047000	0.0174908	-0.0294744	-0.0576875	-4.5743700	98.48
	2.925	-3.4852900	0.0192342	-0.0194277	-0.0536179	-3.5391100	98.48
	3.025	-2.6966300	0.0198243	-0.0122374	-0.0499668	-2.7390100	98.45
	3.125	-2.0582200	0.0196516	-0.0071149	-0.0466796	-2.0923600	98.37
	3.225	-1.5614900	0.0190038	-0.0034815	-0.0437098	-1.5896700	98.23
	3.325	-1.1932200	0.0180825	-0.0009137	-0.0410180	-1.2170700	98.04
10	2.825	-6.40650637	0.003593	0.0012969	-0.0324108	-6.43402794	99.57
	2.925	-5.15837125	0.0031398	0.0041538	-0.0305393	-5.18161448	99.55
	3.025	-4.12193613	0.0028182	0.0057513	-0.0288368	-4.14219155	99.51
	3.125	-3.27551482	0.0025756	0.0065112	-0.0272824	-3.29370823	99.45
	3.225	-2.5834359	0.0023894	0.0067366	-0.0258583	-2.60017046	99.36
	3.325	-2.02571045	0.002235	0.006641	-0.0245496	-2.04137894	99.23
11	2.825	-7.03722989	0.0016791	-0.0087616	-0.0323207	-7.07663258	99.44
	2.925	-5.62066897	0.0012662	-0.0039705	-0.0305045	-5.65387159	99.41
	3.025	-4.46000809	0.0009776	-0.0008647	-0.0288497	-4.48875003	99.36
	3.125	-3.51733145	0.0007717	0.001067	-0.0273364	-3.54283308	99.28
	3.225	-2.76022196	0.0006309	0.0021991	-0.0259478	-2.78333895	99.17
	3.325	-2.1518299	0.0005283	0.0028024	-0.02467	-2.17316543	99.02
12	2.825	-10.8649434	-0.0052768	-0.0150692	-0.0339372	-10.919215	99.50
	2.925	-8.81169737	-0.0057432	-0.0091936	-0.0320781	-8.85871688	99.47
	3.025	-7.10437858	-0.0059399	-0.0050001	-0.0303803	-7.145703	99.42
	3.125	-5.68628868	-0.0059786	-0.0020591	-0.0288248	-5.72315243	99.36
	3.225	-4.53797182	-0.0058756	-3.86E-05	-0.0273948	-4.57128666	99.27
	3.325	-3.60076583	-0.0056974	0.0013184	-0.0260759	-3.6312191	99.16
13	2.825	-8.7675500	-0.0129312	0.1443740	-0.0475191	-8.6836200	100.97
	2.925	-6.8426300	-0.0119873	0.1298540	-0.0447587	-6.7695300	101.08
	3.025	-5.3049300	-0.0108222	0.1173480	-0.0422508	-5.2406600	101.23
	3.125	-4.1119300	-0.0095903	0.1064880	-0.0399636	-4.0550000	101.40
	3.225	-3.1414500	-0.0084381	0.0970003	-0.0378700	-3.0907600	101.64
	3.325	-2.3753500	-0.0074290	0.0886742	-0.0359474	-2.3300500	101.94

14	2.825	-9.0404265	-0.0068039	-0.0018878	-0.0350812	-9.0842057	99.52
	2.925	-7.3035242	-0.0078135	-0.0004817	-0.0331109	-7.3449327	99.44
	3.025	-5.8600168	-0.0082183	0.0005164	-0.0313136	-5.8990407	99.34
	3.125	-4.6634180	-0.0082495	0.0011968	-0.0296683	-4.7001414	99.22
	3.225	-3.7051991	-0.0080141	0.0016384	-0.0281574	-3.7397343	99.08
	3.325	-2.9226160	-0.0076477	0.0019098	-0.0267659	-2.9551173	98.90
15	2.825	-10.0110455	-0.0074487	0.0056522	-0.0354680	-10.0483161	99.63
	2.925	-8.2127036	-0.0075159	0.0079111	-0.0335297	-8.2458361	99.60
	3.025	-6.6946271	-0.0073663	0.0092236	-0.0317595	-6.7245193	99.56
	3.125	-5.4119427	-0.0071100	0.0098740	-0.0301371	-5.4393100	99.50
	3.225	-4.3603441	-0.0067643	0.0100748	-0.0286451	-4.3856774	99.42
	3.325	-3.4965009	-0.0063814	0.0099850	-0.0272689	-3.5201650	99.33
16	2.825	-9.3518606	-0.0082658	0.0034613	-0.0335584	-9.3902253	99.59
	2.925	-7.6401092	-0.0084667	0.0053658	-0.0316985	-7.6749109	99.55
	3.025	-6.2019463	-0.0083684	0.0064717	-0.0300009	-6.2338443	99.49
	3.125	-4.9872101	-0.0081144	0.0070226	-0.0284462	-5.0167376	99.41
	3.225	-4.0040086	-0.0077290	0.0072001	-0.0270176	-4.0315442	99.32
	3.325	-3.1970882	-0.0072891	0.0071397	-0.0257008	-3.2229405	99.20

Table 9. Polynomial fit information for ${}^{1c}J({}^{13}\mathrm{C},{}^{17}\mathrm{O}/{}^{15}\mathrm{N})$ vs the carbon tetrel bond length (BHandHLYP/6-311++G(d,p)).

$$y = \mathbf{A}x^2 + \mathbf{B}x + \mathbf{C}$$

	δ_{iso} / ppm			
Model	**A**	**B**	**C**	R^2
1	-9.88	69.06	-121.84	0.9995
2	-10.17	71.13	-125.62	0.9996
3	-13.52	95.20	-169.38	0.9998
4	-11.34	79.53	-140.83	0.9996
5	-16.19	113.58	-201.50	0.9998
6	-15.94	112.14	-199.48	0.9998
7	-11.13	77.97	-137.96	0.9997
8	-1.46	9.41	-15.08	0.9941
9	-7.41	51.85	-91.61	0.9998
10	-8.32	59.50	-107.81	0.9999
11	-10.57	75.06	-134.91	0.9999
12	-13.31	95.41	-173.40	0.9999
13	-13.31	93.66	-166.45	0.9996
14	-11.45	81.99	-148.84	0.9999
15	-11.27	81.61	-150.02	1.0000

16	-10.94	78.93	-144.54	1.0000

Table 10. Polynomial fit information for ${}^{1c}J({}^{13}C,{}^{17}O/{}^{15}N)$ vs the carbon tetrel bond length (LC-ωPBE-D3/6-311++G(d,p)).

$$y = \mathbf{A}x^2 + \mathbf{B}x + \mathbf{C}$$

	δ_{iso} / ppm			
Model	**A**	**B**	**C**	R^2
1	-10.65	73.88	-129.32	0.9997
2	-11.00	76.40	-133.87	0.9997
3	-14.34	99.96	-175.87	0.9997
4	-10.71	74.46	-130.65	0.9997
5	-15.21	106.10	-186.97	0.9997
6	-14.36	100.66	-178.37	0.9998
7	-11.58	80.46	-141.12	0.9997
8	-1.41	8.97	-14.09	0.9849
9	-7.63	52.78	-92.14	0.9996
10	-7.85	55.40	-98.91	0.9998
11	-9.22	64.88	-115.51	0.9998
12	-14.23	100.74	-180.47	0.9999
13	-14.43	100.28	-175.87	0.9997
14	-12.41	87.61	-156.52	0.9998
15	-12.16	86.77	-156.92	0.9999
16	-11.73	83.47	-150.43	0.9999

Table 11. Polynomial fit information for ${}^{1c}J({}^{13}C,{}^{17}O/{}^{15}N)$ vs the carbon tetrel bond length (CAM-B3LYP/6-311++G(d,p)).

$$y = \mathbf{A}x^2 + \mathbf{B}x + \mathbf{C}$$

Model	δ_{iso} / ppm **A**	**B**	**C**	R^2
1	-10.55	73.73	-130.11	0.9996
2	-10.84	75.89	-134.10	0.9997
3	-14.45	101.77	-181.15	0.9998
4	-11.93	83.61	-147.98	0.9997
5	-18.40	129.27	-229.68	0.9998
6	-17.61	123.85	-220.38	0.9998
7	-11.92	83.55	-147.89	0.9996
8	-1.54	9.93	-15.87	0.9861
9	-8.04	56.10	-98.88	0.9998
10	-8.66	62.01	-112.46	0.9999
11	-10.15	72.17	-129.93	0.9999
12	-14.01	100.67	-183.46	0.9999
13	-14.33	100.70	-178.77	0.9997
14	-11.99	85.94	-156.14	0.9999
15	-11.71	85.00	-156.72	1.0000
16	-11.35	82.10	-150.70	1.0000

Table 12. Polynomial fit information for the CP-corrected energy and the ^{13}C isotropic chemical shift vs the carbon tetrel bond length (MP2/6-311++G(d,p)).

$$y = \mathbf{A}x^2 + \mathbf{B}x + \mathbf{C}$$

	Energy / kcal/mol				δ_{iso} / ppm			
Model	**A**	**B**	**C**	R^2	**A**	**B**	**C**	R^2
1	6.45	-42.81	71.12	0.9977	8.03	-57.07	98.07	0.9999
2	6.45	-42.71	70.68	0.9976	7.94	-56.63	97.63	0.9999
3	3.18	-17.27	14.43	0.9981	2.79	-20.61	59.49	1.0000
4	5.61	-36.78	59.84	0.9970	6.06	-43.39	96.62	0.9999
5	2.77	-13.61	4.74	0.9988	2.53	-19.03	57.35	1.0000
6	5.86	-37.00	54.96	0.9841	4.36	-32.79	81.43	1.0000
7	5.61	-36.84	60.07	0.9968	6.67	-47.72	114.32	0.9999
8	16.96	-112.74	185.57	0.9985	0.18	-1.65	117.48	1.0000
9	5.11	-31.55	45.58	0.9602	0.46	-4.03	106.67	0.9999
10	8.21	-54.40	89.68	0.9977	7.29	-53.12	124.51	1.0000
11	7.86	-51.93	85.01	0.9977	6.97	-50.59	89.30	0.9999
12	8.52	-52.83	72.35	0.9802	2.31	-17.77	37.11	1.0000
13	4.02	-25.56	39.04	0.9896	2.93	-21.54	99.57	1.0000
14	6.34	-41.03	64.63	0.9950	1.63	-13.33	86.88	1.0000
15	5.93	-34.94	40.13	0.9905	2.55	-19.99	67.94	1.0000
16	6.11	-36.99	47.08	0.9722	2.85	-21.77	70.35	1.0000

Table 13. Polynomial fit information for the CP-corrected energy and the ^{13}C isotropic chemical shift vs the carbon tetrel bond length (B3LYP/6-311++G(d,p)).

$$y = \mathbf{A}x^2 + \mathbf{B}x + \mathbf{C}$$

	Energy / kcal/mol				δ_{iso} / ppm			
Model	**A**	**B**	**C**	R^2	**A**	**B**	**C**	R^2
1	6.11	-40.88	68.95	0.9981	8.99	-63.78	124.20	0.9998
2	6.18	-41.38	69.78	0.9978	8.66	-61.83	121.34	0.9999
3	2.77	-14.73	10.60	0.9984	2.63	-19.68	73.61	1.0000
4	5.20	-34.42	57.00	0.9972	7.22	-51.48	125.71	0.9998
5	3.79	-20.13	14.64	0.9984	2.02	-15.67	67.25	1.0000
6	7.29	-46.46	70.62	0.9900	4.26	-32.20	95.89	1.0000
7	5.20	-34.42	57.04	0.9972	7.44	-53.15	137.63	0.9999
8	16.29	-108.65	180.38	0.9986	0.23	-2.08	140.37	0.9999
9	5.52	-35.22	54.19	0.9901	0.34	-2.88	122.95	1.0000
10	7.95	-53.04	88.76	0.9982	7.88	-57.50	147.77	0.9999
11	7.59	-50.54	83.87	0.9979	7.03	-51.35	109.29	0.9999
12	4.84	-28.47	32.59	0.9909	0.72	-6.79	40.43	0.9999
13	3.61	-23.10	35.70	0.9895	3.18	-23.33	119.54	1.0000
14	5.86	-38.12	60.76	0.9954	1.25	-10.87	99.52	0.9999
15	5.45	-31.99	35.80	0.9896	2.06	-16.62	77.16	1.0000
16	5.77	-35.04	44.74	0.9738	2.40	-18.73	80.11	1.0000

Table 14. Polynomial fit information for the CP-corrected energy and the ^{13}C isotropic chemical shift vs the carbon tetrel bond length (LC-ωPBE/6-311++G(d,p)).

$$y = \mathbf{A}x^2 + \mathbf{B}x + \mathbf{C}$$

	Energy / kcal/mol				δ_{iso} / ppm			
Model	**A**	**B**	**C**	R^2	**A**	**B**	**C**	R^2
1	6.11	-40.86	68.72	0.9985	8.35	-59.03	103.83	0.9998
2	6.11	-40.86	68.71	0.9985	8.18	-58.14	102.65	0.9998
3	2.93	-15.78	12.06	0.9986	2.99	-21.97	64.67	1.0000
4	5.11	-34.02	56.50	0.9981	5.34	-38.06	88.83	0.9999
5	2.61	-12.63	2.85	0.9991	2.61	-19.65	61.18	1.0000
6	5.36	-33.87	50.46	0.9832	4.61	-34.36	85.92	1.0000
7	5.25	-34.78	57.54	0.9975	6.40	-45.61	111.28	0.9998
8	17.46	-116.06	191.31	0.9984	-0.04	-0.20	122.68	0.9997
9	6.32	-40.05	60.84	0.9881	0.17	-1.78	110.17	0.9998
10	7.70	-51.40	85.88	0.9982	7.42	-53.56	126.94	0.9999
11	7.43	-49.41	81.74	0.9979	7.06	-50.88	92.70	0.9999
12	5.18	-30.74	36.23	0.9893	1.92	-14.94	38.19	1.0000
13	3.75	-24.00	36.97	0.9922	2.96	-21.75	106.24	1.0000
14	5.84	-38.02	60.45	0.9962	1.54	-12.63	91.72	1.0000
15	5.52	-32.49	36.55	0.9903	2.86	-21.94	73.64	1.0000
16	5.77	-35.01	44.38	0.9709	3.09	-23.29	75.34	1.0000

Table 15. Polynomial fit information for the CP-corrected energy and the ^{13}C isotropic chemical shift vs the carbon tetrel bond length (LC-ωPBE-D3/6-311++G(d,p)).

$$y = \mathbf{A}x^2 + \mathbf{B}x + \mathbf{C}$$

	Energy / kcal/mol				δ_{iso} / ppm			
Model	**A**	**B**	**C**	R^2	**A**	**B**	**C**	R^2
1	5.61	-36.78	60.15	0.9957	8.35	-59.03	103.83	0.9998
2	5.70	-37.19	60.41	0.9950	8.18	-58.14	102.65	0.9998
3	2.45	-11.88	3.89	0.9988	2.99	-21.97	64.67	1.0000
4	4.86	-31.39	49.96	0.9912	5.34	-38.06	88.83	0.9999
5	2.27	-9.48	-4.51	0.9994	2.61	-19.65	61.18	1.0000
6	5.20	-31.90	45.11	0.9422	4.61	-34.36	85.92	1.0000
7	4.79	-30.90	49.19	0.9921	6.40	-45.61	111.28	0.9998
8	18.61	-121.47	195.17	0.9970	-0.04	-0.20	122.68	0.9997
9	5.61	-33.99	47.51	0.9622	0.17	-1.78	110.17	0.9998
10	8.20	-53.65	87.14	0.9961	7.42	-53.56	126.94	0.9999
11	8.04	-52.37	84.22	0.9959	7.06	-50.88	92.70	0.9999
12	5.61	-32.69	37.37	0.9908	1.92	-14.94	38.19	1.0000
13	3.52	-21.69	31.35	0.9596	2.96	-21.75	106.24	1.0000
14	6.34	-40.46	62.49	0.9863	1.54	-12.63	91.72	1.0000
15	6.11	-35.36	38.95	0.9936	2.86	-21.94	73.64	1.0000
16	6.29	-37.49	46.29	0.9855	3.09	-23.29	75.34	1.0000

Table 16. Polynomial fit information for the CP-corrected energy and the ^{13}C isotropic chemical shift vs the carbon tetrel bond length (CAM-B3LYP/6-311++G(d,p)).

$$y = \mathbf{A}x^2 + \mathbf{B}x + \mathbf{C}$$

	Energy / kcal/mol				δ_{iso} / ppm			
Model	**A**	**B**	**C**	R^2	**A**	**B**	**C**	R^2
1	5.61	-36.98	61.14	0.9963	-10.69	55.96	-63.08	0.9561
2	5.70	-37.54	62.01	0.9971	-11.62	61.38	-70.98	0.9553
3	2.27	-10.82	2.68	0.9989	-12.06	68.58	-63.97	0.9237
4	4.77	-31.00	50.02	0.9948	-11.68	63.51	-54.65	0.9465
5	3.95	-20.46	13.45	0.9986	-13.47	77.25	-77.11	0.9170
6	6.45	-40.19	58.71	0.9685	-24.41	139.96	-167.83	0.9151
7	4.93	-32.05	51.83	0.9956	-13.10	71.44	-56.33	0.9454
8	16.36	-107.80	175.74	0.9979	-5.32	31.28	83.70	0.8709
9	5.20	-31.95	46.05	0.9459	-6.02	35.24	61.38	0.8863
10	7.61	-50.21	82.69	0.9975	-15.52	84.24	-71.99	0.9510
11	7.36	-48.43	79.00	0.9967	-13.17	70.81	-81.88	0.9544
12	4.93	-28.51	31.26	0.9932	-11.08	63.10	-70.63	0.9291
13	3.27	-20.17	29.37	0.9569	-12.73	72.49	-28.91	0.9203
14	5.54	-35.39	54.82	0.9911	-13.21	75.66	-33.95	0.9243
15	5.27	-30.21	31.43	0.9950	-16.97	97.22	-97.67	0.9213
16	5.45	-32.33	38.81	0.9861	-14.34	81.48	-74.55	0.9285

Table 17. Polynomial fit information for the CP-corrected energy and the ^{13}C isotropic chemical shift vs the carbon tetrel bond length (BHandHLYP/6-311++G(d,p)).

$$y = \mathbf{A}x^2 + \mathbf{B}x + \mathbf{C}$$

	Energy / kcal/mol				δ_{iso} / ppm			
Model	**A**	**B**	**C**	R^2	**A**	**B**	**C**	R^2
1	5.77	-38.18	63.44	0.9973	8.46	-59.99	110.80	0.9998
2	5.95	-39.28	65.11	0.9972	8.24	-58.78	109.17	0.9999
3	2.43	-11.88	4.28	0.9990	2.93	-21.59	68.61	1.0000
4	4.91	-32.04	51.97	0.9952	6.70	-47.77	111.05	0.9999
5	3.12	-15.25	5.37	0.9988	2.48	-18.72	64.19	1.0000
6	6.04	-37.67	55.17	0.9719	4.70	-34.98	91.78	1.0000
7	4.84	-31.59	51.33	0.9946	6.96	-49.71	123.23	0.9999
8	16.61	-109.81	179.85	0.9981	0.20	-1.78	122.32	1.0000
9	5.20	-32.14	46.79	0.9630	0.36	-3.05	108.91	1.0000
10	7.70	-50.95	84.26	0.9972	7.77	-56.44	137.17	0.9999
11	7.86	-51.80	84.74	0.9980	7.73	-56.24	109.68	0.9999
12	5.02	-29.15	32.41	0.9934	2.01	-15.77	46.55	1.0000
13	3.34	-20.74	30.48	0.9662	3.19	-23.33	109.11	1.0000
14	5.68	-36.45	56.82	0.9919	1.92	-15.42	96.84	1.0000
15	5.34	-30.75	32.47	0.9943	2.86	-22.10	78.15	1.0000
16	5.61	-33.41	40.63	0.9877	3.11	-23.56	80.00	1.0000

Table 18. CP-corrected energy and the ^{13}C isotropic chemical shift vs the carbon tetrel bond angle (CAM-B3LYP/6-311++G(d,p)). In all cases the angle was set so that the oxygen or nitrogen was placed between two methyl hydrogen atoms.

	Interaction energy / kcal/mol Model Structure			δ_{iso} / ppm Model Structure		
Angle / degrees	12	13	16	12	13	16
140	-9.19	-0.73	-8.17	21.34	75.33	43.44
145	-9.34	-0.91	-8.33	20.88	75.14	43.07
150	-9.49	-1.08	-8.51	20.46	74.95	42.68
155	-9.64	-1.25	-8.69	20.09	74.78	42.31
160	-9.77	-1.40	-8.86	19.79	74.64	41.98
165	-9.88	-1.53	-9.01	19.56	74.54	41.72
170	-9.95	-1.63	-9.12	19.42	74.48	41.53
175	-10.00	-1.69	-9.19	19.36	74.48	41.42
180	-10.00	-1.71	-9.21	19.38	74.51	41.40

Appendix II – Sample of Computation Input Files

Gaussian Input for the Geometry Optimization of Acetylene

```
%nprocshared=4
%mem=200MW
%chk=acetylene.chk
# opt freq B3LYP/6-311++g(d,p)

Acetylene

0 1
 O                 -2.38476950    0.11022044    0.00000000
 C                 -3.64316950    0.11022044    0.00000000
 C                 -4.15650238    0.79185828    1.28197473
 H                 -3.79983653    1.80004974    1.31718059
 H                 -5.22650238    0.79185682    1.28197551
 H                 -3.79983440    0.25727357    2.13749044
 C                 -4.15650310   -1.34082091   -0.05067148
 H                 -5.22650116   -1.34089227   -0.04863256
 H                 -3.80150292   -1.81380188   -0.94239110
 H                 -3.79817192   -1.87595925    0.80380246

 1 2 2.0
 2 3 1.0 7 1.0
 3 4 1.0 5 1.0 6 1.0
 4
 5
```

Gaussian Input for NMR calculation of Magnetic Shielding Contributions

```
%nprocshared=4
%mem=200MB
%chk=1.chk
# nmr lc-wpbe/6-311++g(d,p) empiricaldispersion=GD3
counterpoise=2 iop33(10=1)

Mag Sheild

0 1 0 1 0 1
 C(Fragment=1)   -0.02693000   -0.00289400    0.88347900
 H(Fragment=1)   -0.02717500    1.01401200    1.28351400
 H(Fragment=1)    0.85369700   -0.51146400    1.28346400
 H(Fragment=1)   -0.90768000   -0.51156100    1.28308900
 C(Fragment=1)   -0.02685700   -0.00297000   -0.63762200
 H(Fragment=1)    0.85055600    0.50421000   -1.04042300
 H(Fragment=1)   -0.02566900   -1.01586600   -1.04086500
 H(Fragment=1)   -0.90319800    0.50525200   -1.04080600
 C(Fragment=2)   -0.02729300   -0.00348000   -4.66034000
 H(Fragment=2)   -0.35968700    0.87559200   -5.24404400
 H(Fragment=2)    0.30474000   -0.88301700   -5.24355300
 O(Fragment=2)   -0.02685700   -0.00297000   -3.46262200
```

Gaussian Input for NMR calculation of *J*-coupling

```
%nprocshared=4
%mem=200MB
%chk=2.chk
# nmr=spinspin cam-b3lyp/6-311++g(d,p) Counterpoise=2

J-coupling

1 1 1 1 0 1
 C(Fragment=1)        3.54568454    0.01569282    0.23519796
 H(Fragment=1)        3.91235854    0.89998582   -0.27818404
 H(Fragment=1)        3.81597554    0.02344182    1.28480996
 H(Fragment=1)        3.91092554   -0.87688118   -0.26470304
 S(Fragment=1)        1.71996354    0.01562582    0.03088496
 H(Fragment=1)        1.37618554   -0.97148218    0.88942096
 H(Fragment=1)        1.37770954    1.01555082    0.87508296
 N(Fragment=2)        6.46194146    0.01570318    0.46118604
 C(Fragment=2)        7.60343946    0.01541618    0.51346204
 H(Fragment=2)        8.67209546    0.01514518    0.56245804

 1 2 1.0 3 1.0 4 1.0 5 1.0
 2
 3
 4
 5 6 1.0 7 1.0
 6
 7
 8 9 3.0
 9 10 1.0
 10
```